

University of Alabama in Huntsville

**LOUIS**

---

Theses

UAH Electronic Theses and Dissertations

---

2018

## **Experimental investigation of shock wave boundary layer interaction structure and unsteadiness**

Shannon R. Marko

Follow this and additional works at: <https://louis.uah.edu/uah-theses>

---

### **Recommended Citation**

Marko, Shannon R., "Experimental investigation of shock wave boundary layer interaction structure and unsteadiness" (2018). *Theses*. 693.  
<https://louis.uah.edu/uah-theses/693>

This Thesis is brought to you for free and open access by the UAH Electronic Theses and Dissertations at LOUIS. It has been accepted for inclusion in Theses by an authorized administrator of LOUIS.

1681

**Experimental Investigation of Shock Wave Boundary Layer Interaction Structure  
and Unsteadiness**

by

**Shannon R. Marko**

**A Thesis**

**Submitted in partial fulfillment of the requirements  
For the degree of Master of Science Mechanical Engineering  
in  
The Department of Mechanical and Aerospace Engineering  
of  
The School of Graduate Studies  
of  
The University of Alabama in Huntsville**

**HUNTSVILLE, ALABAMA**

**2018**

In presenting this thesis in partial fulfillment of the requirements for a master's degree from The University of Alabama in Huntsville, I agree that the Library of this University shall make it freely available for inspection. I further agree that permission for extensive copying for scholarly purposes may be granted by my advisor or, in his/her absence, by the Chair of the Department or the Dean of the School of Graduate Studies. It is also understood that due recognition shall be given to me and to The University of Alabama in Huntsville in any scholarly use which may be made of any material in this thesis.


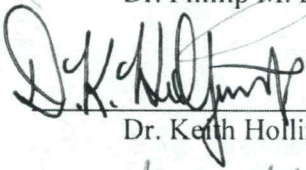
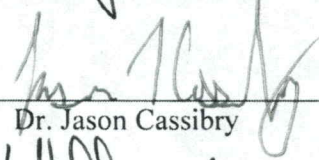
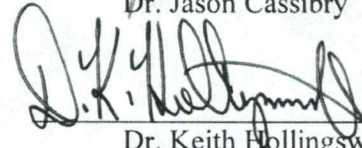
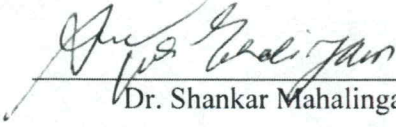

  
(student signature)

25 October 2018  
(date)

### THESIS APPROVAL FORM

Submitted by Shannon Marko in partial fulfillment of the requirements for the degree of Master of Science in Mechanical Engineering and accepted on behalf of the Faculty of the School of Graduate Studies by the thesis committee.

We, the undersigned members of the Graduate Faculty of the University of Alabama in Huntsville, certify that we have advised and/or supervised the candidate on the work described in this thesis. We further certify that we have reviewed the thesis manuscript and approve it in partial fulfillment of the requirements of the degree of Master of Science in Mechanical Engineering.

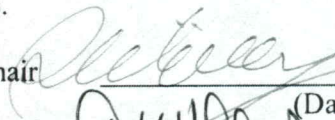
	10-19-2018	Committee Chair
Dr. Phillip M. Ligrani	(Date)	
	10/25/18	Committee Member
Dr. Keith Hollingsworth	(Date)	
	10/25/18	Committee Member
Dr. Jason Cassibry	(Date)	
	10/25/18	Department Chair
Dr. Keith Hollingsworth	(Date)	
	10/26/18	College Dean
Dr. Shankar Mahalingam	(Date)	
	11/2/18	Graduate Dean
Dr. David Berkowitz	(Date)	

**ABSTRACT**  
The School of Graduate Studies  
The University of Alabama in Huntsville

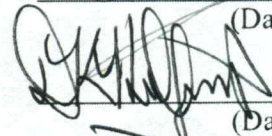
Degree Master of Science College/Dept. Engineering/Mechanical and  
Aerospace Engineering  
Name of Candidate Shannon Marko  
Title Experimental Investigation of Shock Wave Boundary Layer Interaction  
Structure and Unsteadiness

Of interest are the structure and unsteadiness of shock wave boundary layer interactions in a supersonic blow-down wind tunnel. The investigation is motivated because shock wave boundary layer interactions occur in many aerospace, aeronautical, and turbomachinery applications, but are not well understood. As such, the present investigation provides new data to elucidate associated structure and unsteadiness characteristics, in order to improve physical understanding and for development of improved shock wave control strategies. A two-flow-passage test section design is employed with a shock wave holding plate and a downstream choking flap, along with a shadowgraph flow visualization system to visualize unsteady, spatially-resolved flow characteristics. Shock wave structure and unsteadiness are associated with the present wind tunnel configuration, such that higher static pressures downstream of the shock wave result in a shock wave position which is farther upstream and with less overall unsteadiness. The highest amplitudes of this unsteadiness are generally present at Strouhal numbers less than 0.0042. Data associated with the shock wave are also correlated with time-varying data from lambda foot, upstream boundary layer, and downstream boundary layer locations to determine the frequencies and correlation magnitudes of associated flow perturbations.

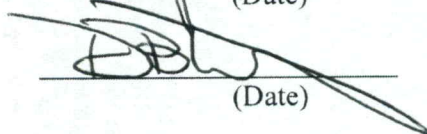
Abstract Approval: Committee Chair

 10-19-2018  
(Date)

Department Chair

 10-25-18  
(Date)

Graduate Dean

  
(Date)

## ACKNOWLEDGEMENTS

I would like to acknowledge my advisor, Dr. Ligrani, for his guidance and support throughout the development of this Master's Thesis. I also warmly acknowledge my other committee members, Dr. Hollingsworth and Dr. Cassibry. The following individuals are acknowledged for their assistance with laboratory development, laboratory testing, laboratory instrumentation and apparatus, safety considerations, and/or data analysis: Tony Hall, David Lineberry, Bob Frederick, Andrew Miller, Melissa Anderson, Robert Pertrimoulx, Daniel Corey, Soo Rhee, Conner Gisburne, Kaylee Hall, Sarah Stearman, Benjamin Shea, Benjamin Lund, Connor Pierce, Patrick McInturff, and Warren Buzzard. I also acknowledge the tree that has given its life for the printing of this thesis. Financial support for this research is provided, through Dr. Ligrani, by The Alabama Innovation Fund (Contract ID No. 61070000002), the University of Alabama Endowment Fund, and the Office of the Vice President for Research and Economic Development of the University of Alabama in Huntsville.

## TABLE OF CONTENT

<b>ABSTRACT.....</b>	<b>iv</b>
<b>ACKNOWLEDGEMENTS.....</b>	<b>v</b>
<b>LIST OF FIGURES.....</b>	<b>x</b>
<b>LIST OF TABLES.....</b>	<b>xix</b>
<b>LIST OF ACRONYMS.....</b>	<b>xx</b>
<b>LIST OF SYMBOLS.....</b>	<b>xxi</b>
<b>CHAPTER</b>	
<b>1 INTRODUCTION.....</b>	<b>1</b>
1.1 Statement of the Problem.....	1
1.2 Survey of Previous Engineering and Scientific Work.....	2
1.3 Objectives.....	4
1.4 Summary of the Approach.....	5
1.5 Synopsis of the Thesis.....	6
<b>2 LITERATURE REVIEW.....</b>	<b>8</b>
2.1 Shock Wave Control in Wind Tunnels.....	8
2.1.1 Upstream and Downstream Wind Tunnel Effects.....	9
2.1.2 Fluctuating Downstream Pressure.....	10
2.1.3 Dual Passage Test Section.....	12
2.2 Low Frequency Shock Wave Unsteadiness.....	13
2.2.1 Upstream Forcing.....	14
2.2.2 Downstream Forcing.....	15
2.2.3 Multiple Forcing Mechanisms.....	17
<b>3 SUPERSONIC WIND TUNNEL FACILITY.....</b>	<b>20</b>
3.1 High-Pressure Piping System.....	23
3.1.1 High-Pressure Compressor.....	24

3.1.2	2500 psi Fill Line.....	25
3.1.3	Air Supply Tanks.....	25
3.1.4	2500 psi High-Pressure Piping Components.....	26
3.1.5	300 psi High-Pressure Piping Components.....	28
3.2	Low-Pressure Piping System.....	31
3.2.1	Low-Pressure Compressor.....	32
3.2.2	Vertical Supply Tank.....	33
3.2.3	Low-Pressure Piping System Components.....	33
3.2.4	Connection of the Low and High-Pressure Piping Systems.....	35
3.2.5	Air Flow Control Components.....	36
3.3	Test Sections.....	39
3.3.1	Inlet.....	41
3.3.2	Nozzle.....	44
3.3.3	The Test Section.....	46
3.3.4	Exhausting the Flow.....	50
<b>4</b>	<b>DATA ACQUISITION.....</b>	<b>56</b>
4.1	Pressure Data Acquisition.....	56
4.1.1	Pressure Measurement Locations.....	56
4.1.2	Pressure Data Acquisition Hardware.....	58
4.1.3	Pressure Data Acquisition Software.....	59
4.2	Visualization System.....	61
4.2.1	Visualization System Instrumentation.....	61
4.2.2	Phantom v711 Camera.....	64
4.2.3	Visualization Data Acquisition Software.....	66
<b>5</b>	<b>ANALYTICAL PROCEDURE.....</b>	<b>67</b>
5.1	Flow Characterization.....	67
5.2	Frequency Analysis of Flow Visualization Data.....	68
5.2.1	Extract Pixel Data.....	68
5.2.2	Filter.....	70
5.2.3	Transform to the Frequency Domain.....	73



5.2.4 Smooth the Frequency Transform.....	76
5.2.5 Remove White Noise.....	79
5.2.6 Ensemble Average the Frequency Data.....	80
5.3 Shock Wave Position Tracking.....	82
5.4 Correlations.....	88
5.4.1 Single Point Auto-Correlation.....	88
5.4.2 Magnitude Squared Coherence.....	89
5.4.3 Cross Power Spectral Density, Phase Lag and Time Lag.....	91
5.4.4 Spatial Variations.....	93
<b>6 TEST SECTION MODIFICATIONS.....</b>	<b>94</b>
6.1 Pressure Data.....	99
6.2 Characteristic Flow Visualization Data.....	101
6.3 Effect of SWHP Refinishing.....	105
6.4 Effects of Plenum Venting.....	106
6.5 Effect of Choking Flap Angle.....	110
6.6 Effects of SWHP Height.....	113
6.7 Effects of SWHP Height, SWHP Distance, and Choking Flap Angle.....	118
6.8 Overall Data Trends.....	121
<b>7 RESULTS FROM 13 NOVEMBER 2017.....</b>	<b>123</b>
7.1 Configuration.....	123
7.2 Overall Results.....	125
7.2.1 Shock Wave.....	125
7.2.2 Lambda Foot.....	127
7.2.3 Upstream Boundary Layer.....	129
7.2.4 Downstream Boundary Layer.....	131
7.2.5 Grayscale Spectral Energy Distribution Comparison.....	133
<b>8 RESULTS FROM 05 APRIL 2018.....</b>	<b>140</b>
8.1 Shock Wave Streamwise Position Spectral Energy Result.....	140
8.2 Grayscale Spectral Energy Results.....	142
8.3 Auto-Correlation.....	144

8.4 Correlations Function Variations Between Regions.....	145
8.4.1 Shock Wave and Downstream Boundary Layer.....	145
8.4.2 Shock Wave and Upstream Boundary Layer.....	147
8.4.3 Shock Wave and Lambda Foot.....	150
8.5 Correlation Function and Time Lag Results to Illustrate Spatial Variations .....	152
<b>9 SUMMARY AND CONCLUSIONS.....</b>	<b>157</b>
<b>REFERENCES.....</b>	<b>160</b>
<b>APPENDIX A: Pressure Regulator Controller Settings.....</b>	<b>164</b>
<b>APPENDIX B: Data File Directory.....</b>	<b>166</b>
<b>APPENDIX C: List of Programs.....</b>	<b>185</b>

## LIST OF FIGURES

Figure 1.1: A shadowgraph image of typical impinging normal and oblique shock waves in a two passage test section.....	2
Figure 1.2: Schematic diagram of the test section.....	6
Figure 3.1: Map of the Johnson Research Center. The wind tunnel is located in and around the room labeled Supersonic Wind Tunnel.....	20
Figure 3.2: The High-Pressure (HP) Layout. This schematic shows the 2500 psig portion of the High-Pressure Piping System. The legend is shown in Figure 3.5.....	21
Figure 3.3: The HP Layout. This schematic shows the 300 psig portion of the High-Pressure Piping System. The legend is shown in Figure 3.5.....	22
Figure 3.4: Low-Pressure (LP) Vertical Tank to Wind Tunnel. A schematic of the low-pressure piping system. The legend is shown in Figure 3.5.....	22
Figure 3.5: Legend for the schematic diagrams in Figs. 3.2, 3.3, and 3.4.....	23
Figure 3.6: The high-pressure piping system and part of the low-pressure piping system. ....	24
Figure 3.7: The high-pressure compressor.....	24
Figure 3.8: The piping and components connecting the 2500 psi tanks (right), the 300 psi tanks (left), and the fill line (vertical center).....	26
Figure 3.9. The control panel showing the digital displays for the pressure transducers.	27
Figure 3.10: The piping components downstream of the bottom 300 psi tank. The piping from the top tank is the same as from the bottom tank.....	29
Figure 3.11: Piping system connection.....	30
Figure 3.12: Photograph of the low-pressure piping system.....	31
Figure 3.13: The air compressor and dryer used in the low-pressure piping system.....	32

Figure 3.14: The 300 psig vertical supply tank.....	33
Figure 3.15: The analog and digital pressure gauges that measures pressure in the vertical supply tank, the six pressure relief valves, and the manual gate valve on the low-pressure piping system.....	34
Figure 3.16: The six pressure relief valves and the manual gate valve on the low-pressure piping system.....	35
Figure 3.17: The connection where the high-pressure piping system joins the low-pressure piping system.....	36
Figure 3.18: The pneumatic valve and the pressure regulating valve. A padlocked box typically encloses these components.....	37
Figure 3.19: The interface with the digital valve controller.....	38
Figure 3.20: The air diverter plenum.....	39
Figure 3.21: The branch of the wind tunnel used for this research.....	40
Figure 3.22. Schematic Diagram of the branch of the test section used for this research.	40
Figure 3.23. A photograph of the connection between the 10.635 inch duct and 9.635 inch square insert.....	41
Figure 3.24. Top view of the inlet to the branch of the wind tunnel from the diverter plenum used in the current research.....	42
Figure 3.25: Inlet spectacle blind valve.....	42
Figure 3.26: Technical drawing of the inlet duct.....	43
Figure 3.27: The inlet to the nozzle that connects with the inlet duct as viewed from upstream.....	44
Figure 3.28: Side view from a technical drawing of the converging diverging nozzle. Flow enters from the left.....	44
Figure 3.29: Plot of the vertical interior wall distance of the nozzle measured from the centerline of the nozzle with respect to distance from the nozzle entrance. The nozzle is symmetric across the centerline. The width is 9.635 inches.....	45

Figure 3.30: The exit to the converging diverging nozzle that connects with the test section as viewed from downstream.....	45
Figure 3.31: The nozzle and test section.....	46
Figure 3.32: An example image showing the choking flap angle calculation.....	47
Figure 3.33: A photograph of the test section. Flow enters from the right.....	48
Figure 3.34: Schematic diagram of the test section. The dimensions shown correspond to the configuration for the tests on 04 and 05 April 2018.....	48
Figure 3.35: Drawing of the top wall of the test section.....	49
Figure 3.36: Vertical profile of the top wall with respect to the distance from the entrance to the test section.....	49
Figure 3.37: The final design of the shock wave holding plate and supports. In this diagram, flow would enter from the left.....	50
Figure 3.38: Top view of the exhaust plenum.....	51
Figure 3.39: Isometric view of the exhaust plenum.....	51
Figure 3.40: The spectacle blind valve for the 4 inch diameter vent. The spectacle blind valve can be fully closed, fully open, or half open.....	52
Figure 3.41: The exhaust piping attached to the downstream exhaust plenum.....	53
Figure 3.42: Exhaust Piping inside the building.....	54
Figure 3.43: Exhaust piping for the wind tunnel facility.....	55
Figure 4.1: The pressure taps and transducers located along the bottom wall of the test section.....	57
Figure 4.2: The bottom wall of the test section. The used pressure taps locations are circled.....	57
Figure 4.3: The location of the pressure transducer that measures the pressure in the exhaust plenum.....	58

Figure 4.4: A schematic diagram of the flow visualization system.....	62
Figure 4.5: Photograph of the flow visualization system.....	63
Figure 5.1: A pixel location at [736, 329] on the shock wave is circled in a shadowgraph image from the test on 13 November 2017.....	69
Figure 5.2: Grayscale value of a pixel location [736, 329] with respect to time for a half second of data from the test on 13 November 2017.....	70
Figure 5.3. The transform function of a Low Pass Butterworth Filter. Lines A through E represent orders 1 through 5. This image is from [27].....	72
Figure 5.4: The grayscale spectral energy distribution before smoothing. This is for the data associated with pixel location identified in Figure 5.1. It is representative of all unsmoothed grayscale spectral energy distribution data.....	76
Figure 5.5: The grayscale spectral energy distribution after smoothing. This is from the data in Figure 5.4.....	78
Figure 5.6: The grayscale spectral energy distribution with and without removing the white noise. The data is from the pixel [736, 329] from the test on 13 November 2017. It is representative of all data before and after removing the white noise.....	80
Figure 5.7: The five grayscale spectral energy distribution with respect to frequency plots for the five pixels analyzed near the shock wave. Data is from the test on 13 November 2017.....	81
Figure 5.8: Ensemble averaged grayscale spectral energy distribution with respect to frequency for pixels near the shock wave from the test on 13 November 2017. This is the average of the grayscale spectral energy distribution data shown in Fig. 5.7.....	82
Figure 5.9: The white line indicates the locations of all the pixels where the grayscale data is . This is from the test on 05 April 2018. The vertical coordinate is 277.....	83
Figure 5.10: Grayscale of the last frame in the time sequence with respect to x pixel location. This is for the horizontal line of pixels all with $z = 277$ for the test on 05 April 2018.....	84
Figure 5.11: 2018-04-05 Shock location as a function of time. This is for vertical pixel location 277.....	86

Figure 5.12: 2018-04-05 Shock location (with respect to the time averaged shock position) as a function of time. This is for vertical pixel location 277.....	86
Figure 5.13: A subset of the data from Figure 5.12. This shows shock wave position from 1.40 to 1.45 seconds.....	87
Figure 5.14: Spectral energy distribution associated with the shock wave position relative to the average shock wave position as a function of frequency.....	87
Figure 6.1: The configuration of the test section. Three of the dimensions vary among tests and are labeled with variables.....	95
Figure 6.2: The shock wave holding plate prior to its modifications between September and November 2017.....	96
Figure 6.3: The modified shock wave holding plate. This plate is used for all tests after and including 08 November 2017.....	97
Figure 6.4: The measured pressures in the test section, the exhaust plenum, and the pressure regulator with respect to time for the test on 08 November 2017. Flow conditions remain established for approximately 3 seconds between 7 and 10 seconds.	100
Figure 6.5: Pressure data from the test on 13 November 2017. Pressures are relatively constant between 7 and 12 seconds. This plot represents the pressure data collected during all tests where the 4 inch vent is half open.....	101
Figure 6.6: Flow Visualization image with flow features labeled. This image is from the test on 29 September 2017.....	102
Figure 6.7: Flow visualization image showing an oblique shock wave impinging on the top wall. This image is from the test on 05 April 2018.....	102
Figure 6.8: A typical flow visualization image from the test on 29 September 2017....	104
Figure 6.9: Another typical flow visualization image from the test on 29 September 2017.....	104
Figure 6.10: Flow visualization images from (a) 29 September 2017 with the original shock wave holding plate, and (b) 08 November 2017 with the shock wave holding plate refinished.....	105

Figure 6.11: Grayscale spectral energy distributions from locations near the (a) shock wave and (b) lambda foot for the tests on 29 September 2017 and 08 November 2017 with the original and refinished shock wave holding plate.....106

Figure 6.12: Shadowgraph images comparing the tests with exhaust pressure to regulator pressure ratios of (a) 0.355 (b) 0.342 and (c) 0.332. These correspond to test on 08 November 2017, 13 November 2017, and 15 November 2017, respectively.....108

Figure 6.13: Representative grayscale spectral energy distributions for locations near the (a) shock wave and (b) lambda foot, comparing the effects of the 4 inch vent position. Pressure ratios are 0.355, 0.342, and 0.334 for closed, half, and fully open venting.....109

Figure 6.14: Total grayscale spectral energy near the shock wave with respect to exhaust plenum to regulator pressure ratio. Dots show average energy of five pixels; error bars indicate maximum and minimum energy.....109

Figure 6.15: Flow visualization images from tests with bottom passage entrance to smallest area ratio of (a) 1.20, (b) 1.16, and (c) 1.04.....110

Figure 6.16: Comparison of characteristic grayscale spectral energy distribution due to a change in choking flap angle from data near the (a) shock wave and (b) lambda foot for tests with entrance to smallest area ratios of 1.20 and 1.16.....113

Figure 6.17: The overall spectral energy decreases as area ratio in the bottom passage increases (caused by raising the choking flap). The central line indicates the average energy and the error bars show the minimum and maximum energies from the five pixel locations considered near the shock wave.....113

Figure 6.18: Shadowgraph images from the tests on (a) 13 November 2017, (b) 05 December 2017, and (c) 08 December 2017, with the shock wave holding plate positioned 1.4 inches, 1.65 inches, and 1.21 inches, respectively, above the bottom wall. ....116

Figure 6.19: Grayscale spectral energy distribution from pixel locations near the (a) shock wave and (b) lambda foot comparing effects of the entrance to smallest area ratio in the bottom passage caused by changing the shock wave holding plate height.....117

Figure 6.20: Total grayscale spectral energy decreases as the entrance to smallest area ratio in the bottom passage increases. Dots indicate the average of data from five pixels near the lambda foot. The error bars show the maximum and minimum energy.....118

Figure 6.21: Shadowgraph images from the tests on (a) 13 December 2017, (b) 22 March 2018, and (c) 05 April 2018.....120



Figure 6.22: Comparison of characteristic grayscale spectral energy for locations near the (a) shock wave and (b) lambda foot. The data is from tests on 13 December 2017, 22 March 2018, and 04 April 2018, and 05 April 2018.....121

Figure 7.1: The configuration of the test section for the test on 13 November 2017.....124

Figure 7.2: The locations of the analyzed pixels on the shock wave for the test on 13 November 2017.....125

Figure 7.3: Grayscale spectral energy distribution associated the shock wave. The associated pixels' locations are shown in Figure 7.2.....126

Figure 7.4: Grayscale spectral energy distribution associated with the shock wave with respect to the Strouhal number. The associated pixels' locations are shown in Figure 7.2 .....127

Figure 7.5: The locations of he analyzed pixels on the lambda foot from the test on 13 November 2017.....127

Figure 7.6: Grayscale spectral energy distribution associated with three pixel locations on the lambda foot. The associated pixels' locations are shown in Figure 7.5.....128

Figure 7.7: Grayscale spectral energy distribution associated with three pixel locations on the lambda foot with respect to the Strouhal number. The associated pixels' locations are shown in Figure 7.5.....129

Figure 7.8: The locations of the analyzed pixels in the upstream boundary layer.....129

Figure 7.9: Grayscale spectral energy distribution associated with three pixel locations in the upstream boundary layer. The associated pixels' locations are shown in Figure 7.8. ....130

Figure 7.10: Grayscale spectral energy distribution associated with three pixel locations in the upstream boundary layer with respect to the Strouhal number. The associated pixels' locations are shown in Figure 7.8.....131

Figure 7.11: The locations of the analyzed pixels in the downstream boundary layer...131

Figure 7.12: Grayscale spectral energy distributions associated with three pixel locations in the downstream boundary layer. The associated pixels' locations are shown in Figure 7.11.....132

Figure 7.13: Grayscale spectral energy distributions associated with three pixel locations in the downstream boundary layer with respect to Strouhal number. The associated pixels' locations are shown in Figure 7.11.....133

Figure 7.14: The locations of the pixels representative of the shock wave, lambda foot, upstream boundary layer, and downstream boundary layer regions.....134

Figure 7.15: Grayscale spectral energy distribution for a location on the shock wave. The pixel is [736, 329] from the test on 13 November 2017.....136

Figure 7.16: Grayscale spectral energy distribution for a location on the lambda foot. The pixel is [739, 226] from the test on 13 November 2017.....136

Figure 7.17: Grayscale spectral energy distribution for a location in the upstream boundary layer. The pixel is [893, 200] from the test on 13 November 2017.....137

Figure 7.18: Grayscale spectral energy distribution for a location in the downstream boundary layer. The pixel is [589, 168] from the test on 13 November 2017.....137

Figure 7.19: Representative grayscale spectral energy distribution from the shock wave, lambda foot, upstream boundary layer, and downstream boundary layer with respect to the Strouhal Number.....138

Figure 7.20: The higher frequency results of the representative grayscale spectral energy distribution in the four considered regions with respect to the Strouhal Number.....139

Figure 8.1: Instantaneous shadowgraph image from the test on 05 April 2018.....140

Figure 8.2: Spectral energy distribution of the shock wave position relative to the average shock wave position as a function of frequency.....141

Figure 8.3: Grayscale spectral energy distribution for locations near the shock wave...142

Figure 8.4: Grayscale spectral energy distribution with respect to frequency and Strouhal number shown in (a) semi-log coordinates, and (b) log-log coordinates.....143

Figure 8.5: A single point auto-correlation as time varies. This utilizes data from a single pixel near the shock wave. The blue lines indicate a 95 percent confidence interval, relative to the zero value.....144

Figure 8.6: Rectangles mark the locations of the pixels in the downstream boundary layer and on the shock wave associated with the data shown in Figures 8.7 and 8.8.....145

Figure 8.7: Magnitude squared coherence of data associated with pixel locations near the shock wave and in the downstream boundary layer.....146

Figure 8.8: Time lag between unsteadiness in the downstream boundary layer and the shock wave. Positive lags indicate the signal in the boundary layer comes first.....147

Figure 8.9: Rectangles mark the locations of the pixels in the upstream boundary layer and on the shock wave associated with data shown in Figures 8.10 and 8.11.....148

Figure 8.10: Magnitude squared coherence between grayscale signals in the upstream boundary layer and on the shock wave.....149

Figure 8.11: Time lag between perturbations in the upstream boundary layer and near the shock wave. Positive lags indicate that the signal in the boundary layer comes first.....149

Figure 8.12: Rectangles mark the locations of the pixels on the lambda foot and on the shock wave associated with data shown in Figures 8.10 and 8.11.....150

Figure 8.13: Magnitude squared coherence as a function of frequency of grayscale time sequence data associated with the shock wave and the lambda foot.....151

Figure 8.14: Time lag between perturbations near the lambda foot and near the shock wave. Positive lags indicate that the signal associated with the lambda foot comes first. ....152

Figure 8.15: The spatial locations where the magnitude squared coherence and time lag are determined and analyzed at specific frequencies. Coordinate axes are in inches.....153

Figure 8.16: The magnitude squared coherence and time lag at frequencies of (a) 20 Hz, (b) 40 Hz, and (c) 100 Hz for  $y_1$  along a line in the boundary layer and  $y_2$  a pixel on the shock wave. Positive values of time lag indicate the boundary layer perturbation comes first.....154

Figure 8.17: The magnitude squared coherence and time lag at frequencies of (a) 20 Hz, (b) 40 Hz, and (c) 100 Hz where  $y_1$  is located on a line along the shock wave and  $y_2$  is a pixel on the shock wave. Positive values of time lag indicate perturbations at the location along the line comes first.....156

## LIST OF TABLES

Table 4.1: The fastest sampling rate for each standard image resolution size for the Phantom v711 camera [27].....	66
Table 5.1: Summary of the smoothing process. This scheme is used for all sampling frequencies.....	77
Table 5.2. The smoothing process for the magnitude squared coherence results.....	91
Table 6.1: The wind tunnel configuration for each of the tests. The dimensions correspond to the variable dimensions in Figure 6.1.....	95
Table 6.2: Effects of opening the 4 inch diameter exhaust vent on the plenum pressure and pressure ratio.....	106
Table 6.3: The entrance to smallest area ratio in the bottom passage due to adjusting the choking flap angle.....	111
Table 6.4: Area and mass flow rate changes dues to shock wave holding plate height. .	114
Table 6.5: Changes to the percentage of the mass flow rate and the entrance to smallest area ratios in the top and bottom passages due to a combination of changes associated with tests on 13 December 2017, 22 March 2018, and 05 April 2018.....	119
Table 7.1: Smoothing process summary associated with the test on 13 November 2017. Sampling rate is 5000 frames per second and frequency resolution is 0.3421 Hz.....	124
Table 7.2: Energy of selected pixels in each of the four flow regions considered. The energy is calculated from the time sequence data and the frequency transformed data..	135
Table 7.3: The value of the white noise subtracted from each of the selected pixels in the four flow regions considered.....	135
Table 7.4: The peak frequencies and Strouhal numbers for the shock wave, lambda foot, upstream boundary layer, and downstream boundary layer for the test on 13 November 2017. An “x” indicates the frequency is prominent in the corresponding region.....	139

## LIST OF ACRONYMS

BD	Burst Disk
DAQ	Data Acquisition
FPS	Frames per second
HP	High Pressure
L	Lockable
LP	Low Pressure
MV	Manual Valve
PID	Position Integral Derivative
PG	Pressure Gauge
PGA	Pressure Gauge
PRC	Propulsion Research Center
PS	Piping System
PT	Pressure Transducer
REG	Pressure Regulator
RV	Relief Valve
SBV	Spectacle Blind Valve
SWHP	Shock Wave Holding Plate
VI	Virtual Instrument

## LIST OF SYMBOLS

$A$	Area, in <sup>2</sup>
$A^*$	Area where the flow is sonic, in <sup>2</sup>
$ACF$	Auto-correlation of grayscale value varying with time, normalized
$A_{min}$	Smallest flow area, in <sup>2</sup>
$c_o$	Variance of the grayscale value at a certain pixel location, GS
$c_m$	Correlation of a time sequence with itself at an instant in time $m$
$C_{xy}$	Magnitude squared coherence estimate
$d$	Distance from test section entrance to the shock wave holding plate tip, inches
$\delta_o$	Boundary layer thickness, inches
$E$	Expected value function
$f$	Frequency, Hertz
$f_o$	Cut-off Frequency, Hertz
$\Delta f$	Frequency resolution, Hertz
$F_s$	Sampling Frequency, frames per second
$\mathcal{F}$	MATLAB's Fast Fourier Transform function operator
$GS$	Grayscale value
$\gamma$	Ratio of constant pressure specific heat to constant volume specific heat
$h$	Distance from the bottom wall to the shock wave holding plate, inches
$i$	Horizontal pixel location counted from the left side of the frame, pixel number
$j$	Imaginary number $\sqrt{-1}$
$m$	dummy variable index

$\dot{m}$	Mass flow rate, lbm/s
$\dot{m}_b$	Mass flow rate in the bottom passage, lbm/s
$\dot{m}_t$	Mass flow rate in the top passage, lbm/s
$M$	Mach number
$n$	dummy variable index
$N$	Number of frames, frames
$P_e$	Static Pressure in the exhaust plenum, psia
$P_t$	Stagnation pressure upstream of the shock wave, psia
$P_{y_1 y_2}$	Cross power spectral density of two functions
$p_{yy}$	Power spectral density of a function
$\phi$	Phase lag, radians
$R$	Gas Constant, ft lbf/(lbm °R)
$St_r$	Strouhal Number
$\Delta St_r$	Resolution of the Strouhal Number
$t$	Time, seconds
$\tau$	Time lag, seconds
$T$	Temperature, °R
$T_t$	Stagnation Temperature, °R
$\theta$	Angle of the choking flap
$u_\infty$	Velocity of the free stream flow, inches per second
$x$	Streamwise location relative to the average position of the shock wave, inches
$y(t)$	Filtered time sequence data
$Y(f)$	Normalized Fourier Transform of $y$

- $z$  Vertical location relative to a reference point on the shock wave, inches
- $\zeta$  Butterworth filter transfer function



## **CHAPTER 1. INTRODUCTION**

Shock waves are present in a variety of engineering applications, such as in transonic gas turbine blade tip gaps, in scramjet isolator ducts, in supersonic aircraft engine intakes, on transonic and supersonic flight vehicle surfaces, and on and around rockets, missiles, and reentry vehicles, among others. These different application environments require consideration of the orientation, position, strength, and unsteadiness of the associated shock waves. The interaction between such shock waves and the boundary layers of these devices are of particular interest. The shock waves and their interactions with the boundary layers affect static and stagnation pressures, boundary layer development and separation, vortex formation, shear stress distributions, convective heat transfer, and flow stability. These, in turn, increase drag on external surfaces, cause buffet, lower engine efficiency, and increase the chances of engine unstart—all undesirable consequences. Active research areas regarding shock wave boundary layer interactions include: designing shock wave and boundary layer control devices, determining the heat transfer effects of the interactions, and—one of the goals of the present research—determining the origin and characteristics of unsteadiness of shock wave boundary layer interactions.

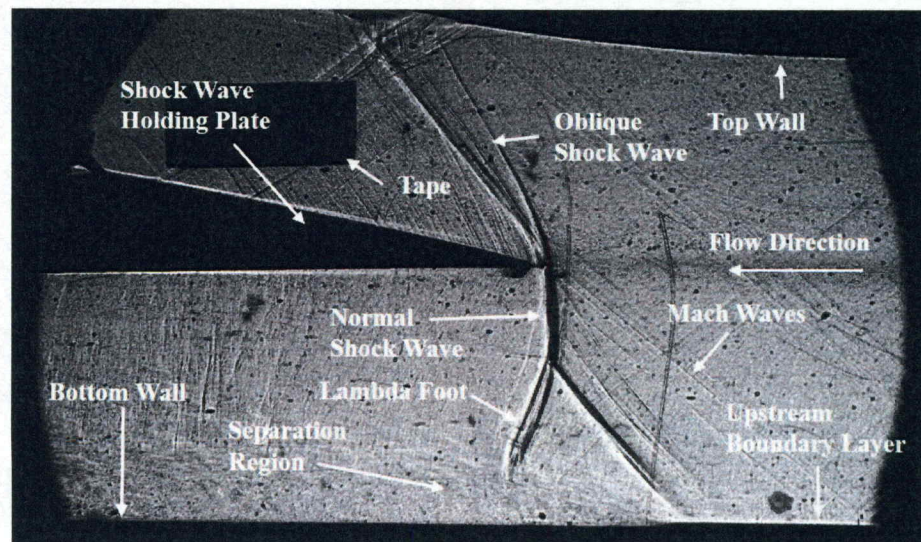
### **1.1 Statement of the Problem**

Fundamental research is required in order to determine the cause of shock wave boundary layer interaction unsteadiness and subsequent flow field unsteadiness. This knowledge can, ultimately, be used to increase shock wave control in engineering

applications and decrease undesired conditions, such as buffet or unstart. This research can be conducted using computational and experimental methods. However, computational studies require validating and flight tests are often impractical. Hence, much of this fundamental work is done in wind tunnels. Configuring a wind tunnel to generate a particular shock wave associated with a particular engineering application can be challenging and take several years of development. This is especially true for impinging normal shock waves.

## 1.2 Survey of Previous Engineering and Scientific Work

The three typical configurations of shock waves frequently studied include oblique shock waves caused by compression ramps, reflected shock waves, and impinging normal shock waves. These can be generated in a constant-area duct, a diverging nozzle, or a multiple passage test section. Figure 1.1 shows a shadowgraph image of an impinging normal shock wave and an impinging oblique shock wave in a two passage test section. Pertinent flow features are labeled. For impinging normal shock



*Figure 1.1: A shadowgraph image of typical impinging normal and oblique shock waves in a two passage test section.*

waves, a two passage test section with the flow in one passage choked and the other unchoked is most effective, as is shown by Ogawa and Babinsky [1]. Ogawa and Babinsky note that changing the dimensional parameters in this type of test section affects the shock wave position, strength, and orientation; however, documentation detailing how the shock wave is affected by these changes is somewhat lacking. Several studies [2-7] have been done in single-passage parallel and diverging ducts where a dynamic back pressure downstream of the shock wave forces shock motion. These provide greater evidence about how wind tunnel configurations affect shock waves. Since unsteadiness is controlled and forced on the shock wave in these studies, the authors neglect mention of how each static wind tunnel configuration affects overall flow unsteadiness.

Shock waves also exhibit an unsteadiness that is not caused by the wind tunnel. The origin and frequency of this unsteadiness are debated. Frequency is often represented by Strouhal number, a non-dimensional parameter scaling the frequency by a length scale and the incoming flow velocity. Strouhal number is advantageous over dimensional frequency because it is independent of flow conditions. In external flows that are studied using compression ramps, it is generally agreed that the Strouhal number of this unsteadiness is approximately 0.03, using the interaction length as the length scale as defined by Clemens and Narayanaswamy [8]. Despite this agreement, understanding the source of the unsteadiness is still illusive. For the internal flows studied by reflected shock waves and impinging normal shock waves, there is not yet a collapse of frequency data; the prominent frequencies detected from several experiments and computations are

not scaled such that they all converge to a single value [8]. Knowing the source of the unsteadiness may assist in finding the appropriate scaling factor.

Some researchers detect great coherence between the upstream boundary layer and the unsteadiness in the interaction region [9-12]. Others do not detect any correlation at all [13, 14]. This discrepancy may be caused by differences in interaction strength [8]. Stronger shock waves ( $M \geq 1.4$ ) cause boundary layer separation just downstream of the shock wave. For flows with shock wave induced separation, many researchers proclaim that unsteadiness in the interaction region is related to pulsations of the separation region [13-16]. This source may overpower the influence of the upstream boundary layer [8]. This provokes the question of what causes the separation region pulsations. The two accepted hypotheses are that it is linked to the upstream boundary layer [8, 16] or that it is caused by a cyclical mass entrainment and shear layer vortex shedding process [13, 14]. The desire to reconcile the different—and sometimes conflicting—conclusions necessitates further investigation in this area.

### **1.3 Objectives**

There are two main objectives to this thesis. The first is to modify a wind tunnel in order to alter and control the position, orientation, strength, and unsteadiness of a shock wave. A two-flow-passage test section, similar to that used by Ogawa and Babinsky [1] is used in this study. The present research extends the information in the literature by describing how changes to the area ratio of the choked passage, mass flow rate of each passage, downstream exhaust pressure, and imperfections in the test section components manipulates the shock wave and its associated unsteadiness. Minimizing the

unsteadiness caused by the wind tunnel is particularly important in order to accurately detect unsteadiness from other sources.

The second objective is to determine the frequencies and sources of the interaction unsteadiness from an impinging normal shock wave turbulent boundary layer interaction. This interaction is formed in the wind tunnel developed in the first objective. This second objective is new data to the literature that may assist others in finding a common frequency and source of unsteadiness for internal flows. Without this fundamental physical understanding, effectively controlling shock waves in more complicated engineering applications is limited.

#### **1.4 Summary of the Approach**

The supersonic wind tunnel on the University of Alabama in Huntsville's campus is used for this research. It is a two passage test section with a diverging top passage and constant-area bottom passage. A labeled schematic of this test section is shown in Figure 1.2. A shock wave holding plate separates the two passages. The bottom passage is choked using a variable angle choking flap. A normal shock wave boundary layer interaction is generated in this test section. The shock wave structure and unsteadiness are modified by changing the condition of the shock wave holding plate, the position of the shock wave holding plate, the angle of the choking flap, and the amount of exhaust vents downstream of the test section.

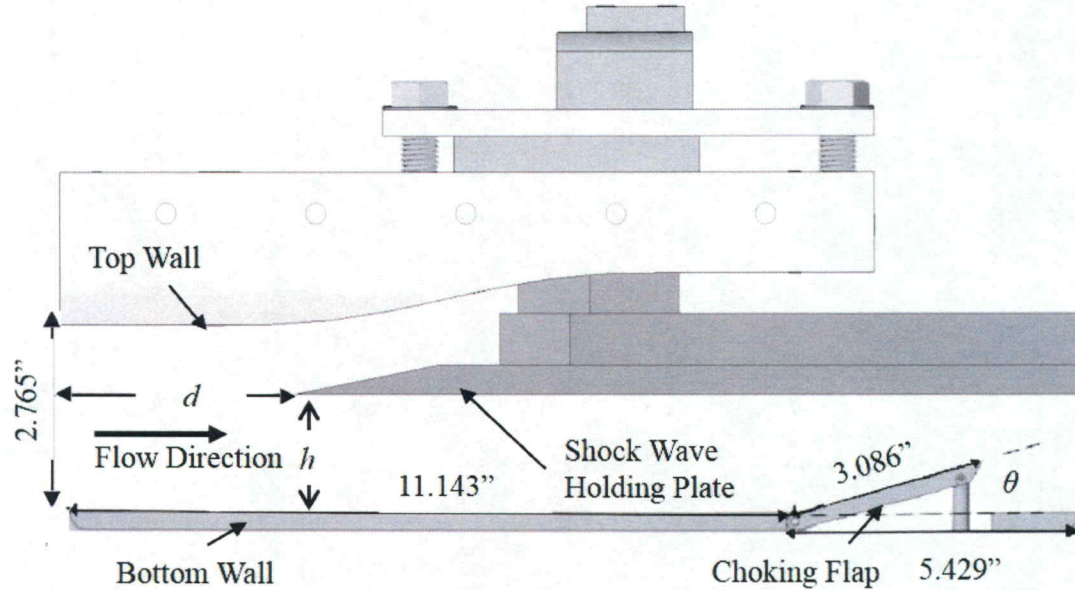


Figure 1.2: Schematic diagram of the test section.

Wind tunnel tests are conducted for approximately eight seconds. Static pressure data and shadowgraph visualization data are collected during this time. Frequency transforms of individual pixel locations in the shadowgraph visualization image data are analyzed to determine the unsteadiness near the shock wave, near the lambda foot, in the upstream boundary layer, and in the downstream boundary layer. These data are also used in finding correlations among interaction and upstream and downstream regions. The shadowgraph data are used to determine the approximate location, and track the path, of the shock wave motion from a Lagrangian perspective, as well.

## 1.5 Synopsis of the Thesis

Chapter 2 provides a detailed literature review. It discusses previous work relating wind tunnel set-up to shock wave configuration and stability, and reviews the previous findings regarding innate shock wave unsteadiness in external and internal flows. Chapter 3 describes the wind tunnel facility used to generate the shock wave boundary

layer interaction under study. The shadowgraph and pressure data acquisition systems are described in Chapter 4. Chapter 5 details the analytical procedures used to determine the prominent unsteady frequencies from the shadowgraph grayscale pixel values, the shock wave motion, and the correlations of frequencies between the interaction, the upstream, and the downstream regions. Chapter 6 shows how changes to the wind tunnel circuit modify the shock wave structure and unsteadiness. Chapter 7 provides preliminary frequency results from an early test. The results from this test informed the procedures presented in Chapter 5. Chapter 8 gives frequency results from the final test and examines correlations between flow regions in an attempt to determine the source of the interaction region unsteadiness. Chapter 9 provides a summary and conclusions of the present work.

## **CHAPTER 2. LITERATURE REVIEW**

This chapter summarizes other investigations that are related to the present research. It begins by describing how wind tunnels have been altered to affect shock wave boundary layer interactions. Then, it provides background concerning the origins of the unsteadiness within the interaction region. Babinsky and Harvey [17] provide excellent detail regarding the flow physics of shock wave boundary layer interactions, such as the generation of the separation region from strong pressure gradients and the overall structure of the various types of shock wave boundary layer interactions.

### **2.1 Shock Wave Control in Wind Tunnels**

Shock-wave boundary-layer interactions occur in many applications, such as supersonic air intakes, transonic wings, and turbomachinery blade tips. Shock wave control is necessary for lowering the stagnation pressure drop in supersonic engine inlets and reducing wave drag on high speed aircraft wings. Fundamental experimental research of the shock-wave boundary-layer interactions is critical for understanding and being able to control the shock wave boundary-layer interactions in these more complicated flows. Much of this fundamental research is done in wind tunnels. Hence, it is important to be able to control shock wave structure and unsteadiness in wind tunnel test sections. Several studies have been conducted regarding control of shock wave turbulent boundary layer interactions in wind tunnels.



### 2.1.1 Upstream and Downstream Wind Tunnel Effects

Sajben and Kroutil [18] determine the effects of the boundary layer thickness on the unsteadiness of the shock wave. This is done experimentally by tracking the position of a normal shock wave in a wind tunnel diffuser. Even without upstream or downstream forcing, the shock wave still oscillates. These authors conclude that for shock wave boundary layer interactions without boundary layer separation, the thickness of the incoming boundary layer and the peak frequency of the shock wave motion are directly related; as the boundary layer thickness increases, so does the peak frequency. For flows with shock wave induced separation, there is no observed relationship between the boundary layer thickness and the shock wave unsteadiness.

Bogar et al. [19] do a similar study of shock wave unsteadiness in a diffuser. In their study, Bogar et al. vary the length of the duct downstream of the diffuser to determine the downstream effects on the shock wave. For cases where the boundary layer remains attached, they observe that the frequency of the shock wave motion depends inversely on the length of diffuser duct. This correlation is suspected to arise from acoustic resonance. Robinet and Casalis [20] numerically determine that for the same configuration as is used by Bogar et al. [19], the relationship between the diffuser length and shock wave oscillation frequency is caused by weak shock wave reflections at the diffuser exit. When shock wave induced boundary layer separation is present, there is no correlation between the shock wave frequencies and the diffuser length.

Handa et al. [21] note that the frequency of unsteadiness differs between the studies of Sajben and Kroutil [18] and of Bogar et al. [19]. Handa et al. [21] use results from experimental and numerical techniques. Replicating the diffuser used in the studies

of Bogar et al. and Robinet and Casalis, Handa et al. confirm the correlation between the pressure disturbance at the diffuser exit and the shock wave unsteadiness. Contrarily, using a different diffuser configuration, Handa et al. show that a shock wave reflection or pressure disturbance at the diffuser exit provides negligible effects on the shock wave oscillation. Instead, observed are large pressure fluctuations in a location downstream of the shock wave where the flow is highly turbulent. Handa et al. attribute much of the shock wave motion to these fluctuations. They also observe pressure fluctuations originating near the shock wave foot.

### **2.1.2 Fluctuating Downstream Pressure**

The findings of Handa et al.[21] imply that any pressure perturbation downstream of the shock wave may affect the shock wave stability. Other studies [2-6] intentionally induce a pressure disturbance by rotating a cam in the flow downstream of the shock wave. Doeffler et al. [7] describe a similar study by oscillating the angle of a choking flap instead of a cam. From this, they are able to study the shock wave boundary layer interaction response to a controlled, oscillatory, back pressure. These studies have been conducted at Mach numbers ranging from 1.2 to 1.5.

Edwards and Squire [2] use a constant cross section duct. An elliptical cam is located in the center of a diffuser downstream of the test section and rotates at frequencies between 34 Hz and 167 Hz. These authors find that for larger cams, the upstream stagnation pressure needs to be lower to maintain the same shock wave position in the test section. Also as the cam size increases, the unsteady shock wave motion amplitude increases. Ott et al [3] obtain similar results using a diverging channel. The cam is elliptical and rotates at frequencies between 0 and 180 Hz. When the long side of

the ellipse is horizontal, the shock wave is farthest downstream. When it is vertical, the shock wave is farthest upstream. Bur et al. [4] employ a diverging duct with a variable second throat to control the time-averaged location of the shock wave in the test section. The elliptical cam in this study is located in the second throat. Bur et al. conclude that large-scale unsteadiness that affects the whole flow field must be separated from the small scale fluctuations that affect the interaction region only. As such, the location of the shock wave is modeled by a constant location, with the excited frequency from the cam and random frequencies superimposed on it.

Edwards and Squire [2] also observe that the induced frequency is inversely proportional to the amplitude of the shock wave motion. Ott et al. [3] and Bur et al., [4] confirm these observations. The results of Doerffer et al. [7] agree with these authors for excitation frequencies between 50 Hz and 512 Hz. This inversely proportional relationship maintains a constant maximum velocity of the shock wave with respect to the test section walls for all frequencies. Doerffer et al. [7] observe that for excitation frequencies below 50 Hz, the shock wave amplitude is constant because it has enough time to reach equilibrium pressures before the excitation reverses. Above 512 Hz, the forced oscillations subside and only the natural oscillation are observed.

Furthermore, when forced oscillations are observed, the shock wave is momentarily stationary at the farthest upstream and farthest downstream positions. At these locations, Edwards and Squire [2] observe that the pressure signals are not the same as when the shock waves are in those locations in quasi-steady flow conditions, especially when the boundary layer is separated. However, Ott et al. [3] noted that there is no phase lag between the pressure signals and the shock wave oscillations. Bur et al.

[4] observe that pressure variations of the rotating shaft are not present upstream of the shock wave. Such pressure variations are transmitted upstream to the shock wave by means of damped acoustic waves.

Bruce and Babinsky [5] study shock wave structure and motion in a constant cross section duct. An elliptical cam is rotated at frequencies between 8 and 45 Hz. These authors note that resonance in the wind tunnel greatly affects the data at certain excitation frequencies. Also, because of wind tunnel operation errors, the shock wave is observed to move up to 0.75 inches from its mean position in an irregular fashion.

### **2.1.3 Dual Passage Test Section**

According to Bruce and Babinsky [5], controlling the position of a shock wave in a constant-area duct requires great effort. Ogawa and Babinsky [1] state that any shock wave control mechanism that reduces pressure losses increases shock wave instability. The stagnation pressure ratio across the shock wave decreases when the shock wave is located at the control mechanism. When the stagnation pressure ratio rises, the shock wave moves downstream to the control mechanism, then skips over part of it such that the stagnation pressure ratio continues its rising trend. Similarly, the shock wave skips over part of the control mechanism when it is traveling upstream so that the stagnation pressure ratio continues to drop. The shock wave motion direction is reversed when the stagnation pressure ratio (related to static pressure ratio) becomes too large or too small to sustain the shock wave position. This instability makes shock wave control in conventional wind tunnels impossible. Thus, Ogawa and Babinsky [1] propose a unique experimental arrangement to produce a normal shock wave, which impinges upon the boundary layer of a wind tunnel wall. This arrangement uses a shock wave holding plate

to partition the flow behind the shock wave into an upper, un-choked, channel and a lower, choked, channel. It has the benefit of producing a more stable shock wave than in a constant-area channel test sections. The position of the shock wave holding plate, which separates the two channels, and the choking flap, which chokes the flow in the bottom channel, are manipulated to position the shock wave and produce the desired testing conditions. A similar test section to the one described by Ogawa and Babinsky [1] is used in the present study.

Chapter 6 extends the results of these authors by providing further insight on how the wind tunnel configuration affects the shock wave structure. It also details how test section changes affect the unsteadiness of the shock wave and the lambda foot. In particular, the present study provides data that illustrate the effects of manipulating the amount of exhaust venting, the angle of the choking flap, and the position of the shock wave holding plate.

## **2.2 Low Frequency Shock Wave Unsteadiness**

More recent investigations of shock wave boundary layer interactions consider associated low frequency unsteadiness. The origin of this unsteadiness is still unknown as several studies give different and even contradictory results. Both upstream and/or downstream mechanisms are cited as the source of the unsteadiness. The frequencies commonly detected are two to three orders of magnitude smaller than the characteristic frequency of the turbulence within the incoming boundary layer. Considering a number of ramp-induced shock wave boundary layer interaction studies, Dussauge et al [22] conclude that the interaction unsteadiness occurs at Strouhal numbers between 0.02 and 0.05, where frequency is scaled based on the interaction length and the incoming

velocity. Interaction length is typically defined as the average distance from the shock wave foot to the reattachment point. Note that this is a different definition of Strouhal number than employed within the present study. Similarly, Clemens and Narayanaswamy [8] state the Strouhal number is 0.03 for their collection of ramp-induced shock wave studies, using the same definition of Strouhal number as Dussauge et al. [21]. They do not present a single number characterizing impinging shock wave unsteadiness [8].

### **2.2.1 Upstream Forcing**

Humble et al. [9] conduct an experimental study of the upstream boundary layer using tomographic particle image velocimetry. This permits them to visualize the flow field in three dimensions. An incident oblique shock wave is generated from a shock generator with a  $10^\circ$  angle and the flow Mach number of 2.1. Humble et al. [9] verify the existence of complex three dimensional structures in the upstream boundary layer. Particularly in the logarithmic region close to the wall, they detect regions of high and low-speed flow forming the a variety of structures. The structures observed include long streamwise structures, referred to as hairpins, at least  $2\delta_0$  in length. Ganapathisubramani et al. [10, 11] observe similar structures that are approximately  $50\delta_0$  in the streamwise direction and less than  $0.5\delta_0$  in the spanwise direction. Humble et al. also observe that when large areas of high speed flow approach the shock wave, the reflected shock wave moves downstream. Conversely, as low-speed flow approach the interaction, the reflected shock wave is farther upstream relative to the interaction region. Hence, according to these investigators, large fluctuating structures in the upstream boundary layer are responsible for the unsteadiness in the shock wave and interaction region. Ganapathisubramani et al. [10] suggest that the separation region resulting from a ramp

flow responds to these upstream structures. The results of Humble et al. and Ganapathisubramani et al. are quite similar, citing structures in the upstream boundary layer as the cause of the shock wave boundary layer interaction unsteadiness for different experimental configurations.

Touber and Sandham [12] apply a numerical and an analytical model of an oblique impinging shock wave and its reflection in a Mach number 2.3, turbulent, flow. Their model suggests that no significant low frequency structures, upstream nor downstream, are necessary to cause the shock wave boundary layer interaction unsteadiness. Instead, they supply white noise fluctuations in the upstream boundary layer and discover that the shock wave oscillations still occur. They attribute the presence of particular unsteady frequencies to the low pass filtering effect of the reflected shock wave boundary layer system.

### **2.2.2 Downstream Forcing**

Piponniau et al. [13] describe a forcing method that originates downstream of the shock wave boundary layer interaction in flows with reattaching separation regions. In this work, the investigators suggest that mass must enter the separation region upstream and must exit downstream. The amount exiting is not the same as the amount entering (since some of the flow is reversed), causing a build-up of mass in the separation region, and hence, causing the separation region to grow. This occurs until the mass in the separation region is significant enough to force a greater flow rate out, which is associated with an arrangement wherein the amount of mass exiting supersedes the amount entering and the separation region shrinks. The cyclical growing and shrinking of the separation region causes a pulsation with the time scale which is related to the ratio of

the mass in the reverse flow to the mass being entrained. A mathematical model is established to calculate the characteristic frequencies of the separation region pulsations. Piponniau et al. [13] apply this theory to an experimental reflected shock wave. They discover that the pulsations of the separation region are in good agreement with their model, and they indicate that the reflected shock wave moves downstream as the region shrinks and upstream as the region grows. The possibility of turbulent superstructures also influencing the shock wave motion is dismissed because the time scale of the superstructures would create frequencies an order of magnitude higher than the detected shock wave motion frequencies. From this, Piponniau et al. conclude that the shock wave motion must be caused by the pulsating mass entrainment process of the separation region, not upstream forcing.

Grilli et al. [14] use a large eddy simulation of flow over a compression expansion ramp emulating an experiment described in Zheltovodov et al. [23] The shock wave causes boundary layer separation. Near the shock wave foot, the discovered frequency is  $0.0039U_\infty/\delta_0$ . The frequency is scaled based on the length of the separation region, giving a Strouhal number of 0.0234. Unsteadiness at these Strouhal numbers is not found to be prominent in the upstream boundary layer, nor as the flow approaches the reattachment point; it exists only in the region between the shock wave foot downstream to half-way through the separation region. Using dynamic mode decomposition, four modes are selected. The reconstructed flow field agrees well with the original, and a pulsating or breathing motion is present in the separation region. No turbulent structures are associated with this model. Further investigation provides evidence that the separation region pulsations are caused by a mass entrainment process. Grilli et al. [14] detect a



delay between the pulsations of the separation region and the motion of the shock wave, indicating that the shock wave unsteadiness comes solely from the separation region mass entrainment. Grilli et al. [14] do note that any structures similar to those found by Ganapathisubramani [10,11] would be outside of the spatial domain considered by them. Frequencies of that scale would be an order of magnitude larger than the modes from their dynamic mode decomposition.

### 2.2.3 Multiple Forcing Mechanisms

Wu and Martin [15] use direct numerical simulation of a Mach 2.9 flow over a  $24^\circ$  compression ramp. These authors detect low frequency motion at frequencies of  $(0.01 \pm 0.003)U_\infty/\delta_o$  and higher frequency spanwise wrinkling on the order of  $U_\infty/\delta_o$ . The low frequencies scale to Strouhal numbers based on the interaction length of 0.03 to 0.042. These authors attribute the spanwise wrinkling oscillations in the upstream boundary layer, but detect little correlation between the low frequencies and low momentum structures in the incoming boundary layer.

Pirozzoli et al. [16] use large eddy simulations of reflected shock waves with several incident shock wave strengths. They observe that increasing shock wave strength increases the size of the interaction zone and a separation region forms. High and low frequency modes are found. The higher frequency with a Strouhal number of approximately 1 (where  $St_r = f\delta_o/U_\infty$ ) is associated with turbulence. Turbulent structures are observed to propagate from the upstream boundary layer through the interaction region in the separated shear layer. The lower frequency mode is three orders of magnitude smaller than the high frequency mode and relates to the separation region pulses. The dimensional low frequency near the interaction region decreases as the

separation region increases in size. The approach used by Pirozzoli et al. provide no indication of which, the separation region pulses or the shock wave motion, is the cause and which is the effect.

Pirozzoli et al. [16] also complete a global stability analysis that shows a non-oscillatory, higher frequency, growing mode and several weakly damped, lower frequency, modes. They correlate the damped modes with separation region pulsations. The authors surmise that the non-oscillatory mode is likely overcome by non-linear effects, making it undetectable if it even exists. However, the damped modes must have some excitation source to sustain them, otherwise the damping would diminish the mode to nothing after a short time. In essence, Pirozzoli et al. [16] claim that the upstream boundary layer must be supplying the low frequency energy to drive the pulsations of the separation region and shock wave. Such a result is consistent with Toubert and Sandham [12], and the early work by Plotkin [24]. Note that Plotkin [24] states that the shock motion is caused by a linear mechanism restoring equilibrium from an imbalance caused by upstream forcing. Pirozzoli et al. [16] cannot attest to how the energy in the upstream boundary layer manifests into low frequency pulsations in the interaction region.

Gamba [25] describes unsteadiness surrounding normal impinging shock waves. Gamba generates a train of normal shock waves in a shock tube. The upstream most flow is at Mach 2. Events occur upstream and downstream of the shock waves. This author correlates these events and the shock waves. Gamba determines that low frequency events (less than 250 Hz) are created downstream and within the shock wave train, and propagate upstream through acoustic waves in the boundary layer, before affecting the shock waves in order from upstream to downstream. Frequencies less than 3000 Hz

originate within the shock wave train, specifically between the first and second shock waves, and propagate both upstream and downstream. Gamba suspects that these disturbances are caused by boundary layer separation or corner effects.

From this survey, it is evident that some researchers claim that the unsteadiness in the interaction region comes from upstream forcing. Others claim that the unsteadiness is from the downstream forcing but not upstream forcing. Others claim that shock wave unsteadiness originates from both upstream and downstream forcing. Clemens and Narayanaswamy [8] compile many results in an attempt to reconcile these different ideas. These authors hypothesize that the upstream boundary layer may influence the frequency of the pulsation region, which in turn excites the shock wave. They suggest that, for mildly separated flows, the upstream forcing dominates. For strongly separated flows, the forcing from the pulsating separation region dominates and masks the upstream component. Despite over fifty years of research in shock wave boundary layer unsteadiness, the source of the unsteadiness still remains controversial and a debated topic.

### CHAPTER 3. SUPERSONIC WIND TUNNEL FACILITY

The supersonic wind tunnel used in the present study is located in the Johnson Research Center on the University of Alabama in Huntsville's campus. Figure 3.1 shows the Supersonic Wind Tunnel labeled on a map of the Johnson Research Center. The pressurized piping and exhaust ducts are located outside the building, in the areas surrounding the room labeled as the Supersonic Wind Tunnel.

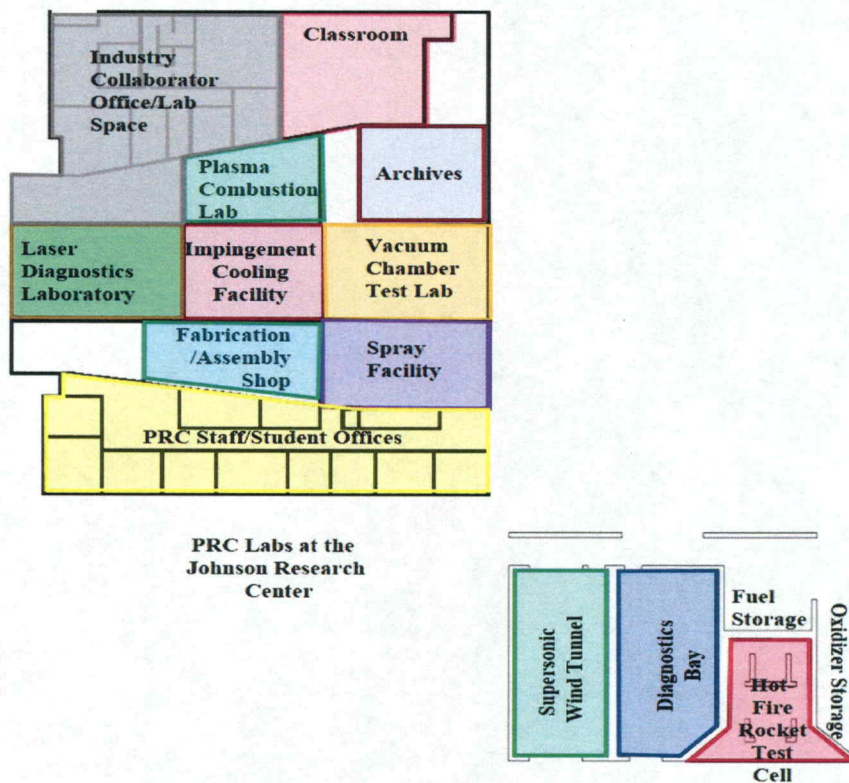


Figure 3.1: Map of the Johnson Research Center. The wind tunnel is located in and around the room labeled Supersonic Wind Tunnel.

The wind tunnel is a blow-down facility. The working fluid is dried air. The wind tunnel is comprised of a high-pressure piping system, a low-pressure piping system, two

test section assemblies, and exhaust piping. Compressors, air storage tanks, ball valves, knife gate valves, spectacle blind valves, pressure relief valves, burst disks, analog pressure gauges, digital pressure transducers, and an air diverter plenum control the air in the high and low-pressure piping systems. The many components in this system allow it to produce a wide variety of conditions for different testing environments.

The high-pressure piping system connects to the low-pressure piping system. A spectacle blind valve can be used to isolate the air in the high-pressure piping system from the air in the low-pressure piping system. Figure 3.2 is a schematic diagram of the 2500 psi portion of the high-pressure piping system. Figure 3.3 is a schematic diagram of the 300 psi portion of the high-pressure piping system. Figure 3.4 is a schematic diagram of the low-pressure piping system. Figure 3.5 shows a legend defining the symbols used in the schematic diagrams.

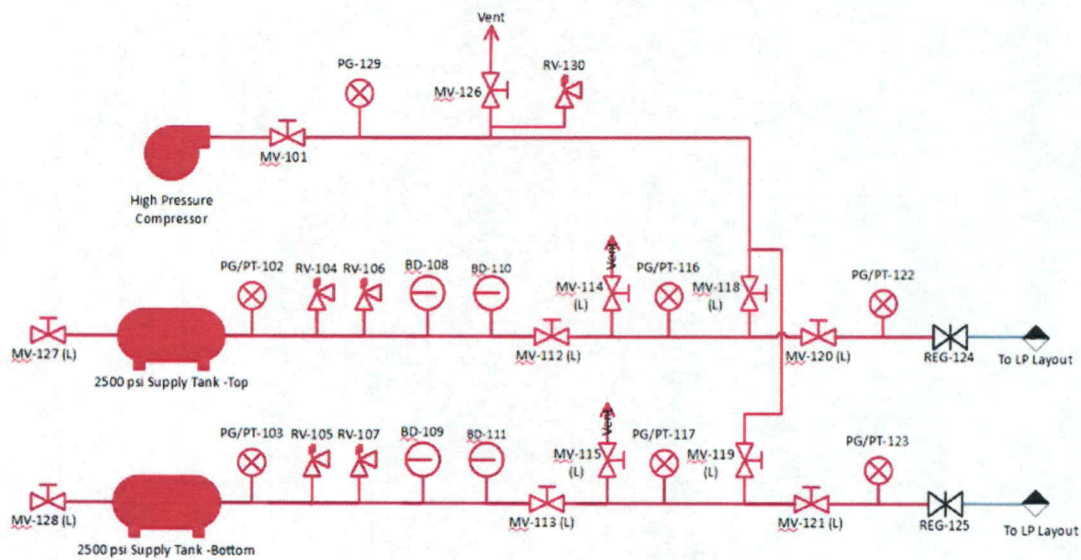


Figure 3.2: The High-Pressure (HP) Layout. This schematic shows the 2500 psig portion of the High-Pressure Piping System. The legend is shown in Figure 3.5.

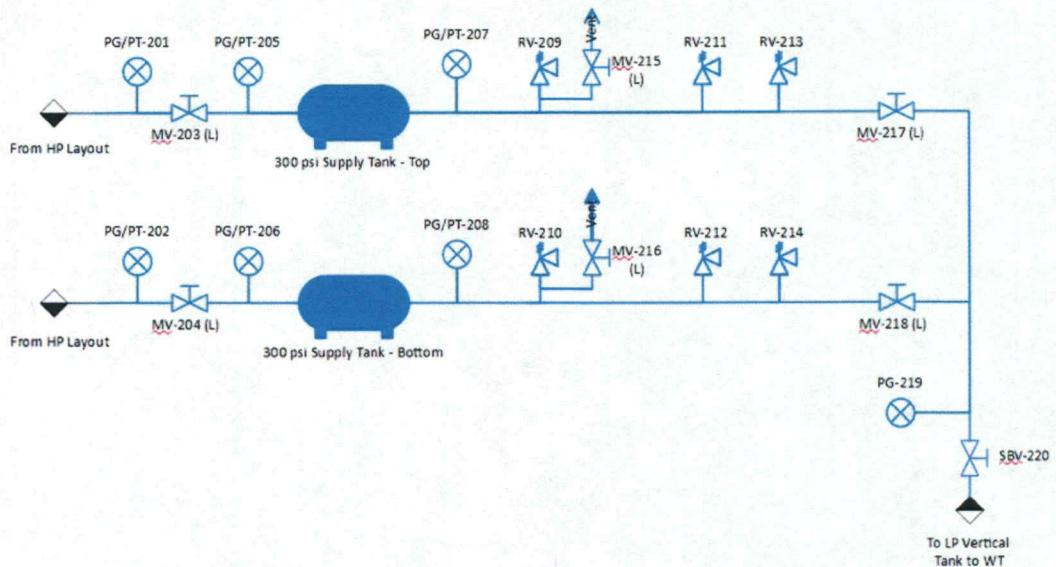


Figure 3.3: The HP Layout. This schematic shows the 300 psig portion of the High-Pressure Piping System. The legend is shown in Figure 3.5.

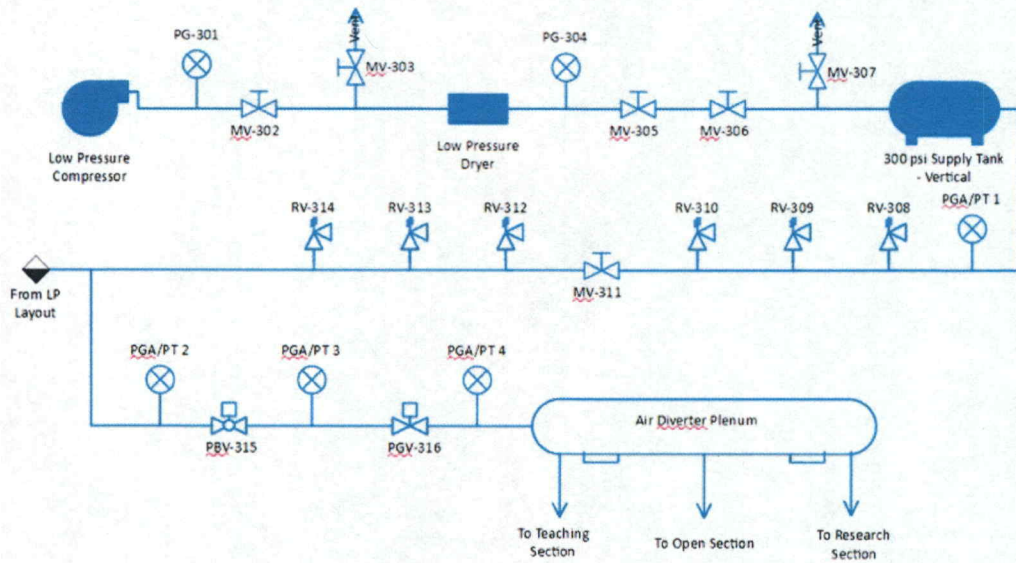
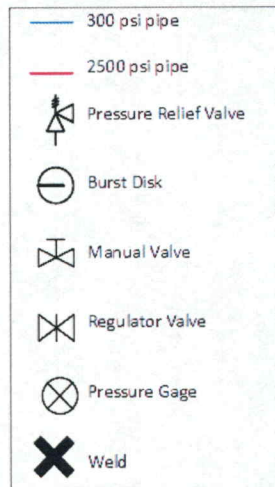


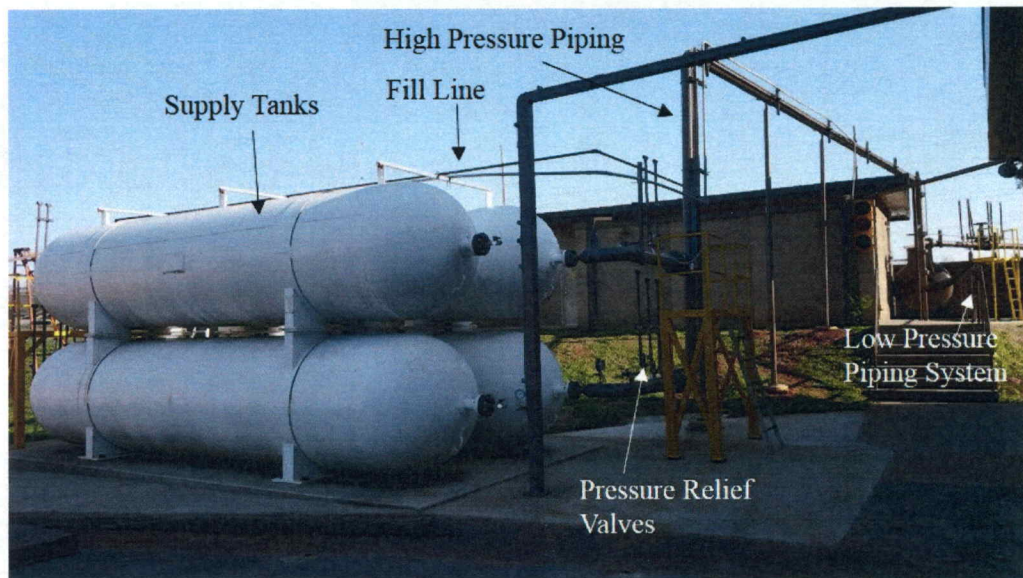
Figure 3.4: Low-Pressure (LP) Vertical Tank to Wind Tunnel. A schematic of the low-pressure piping system. The legend is shown in Figure 3.5.



*Figure 3.5: Legend for the schematic diagrams in Figs. 3.2, 3.3, and 3.4.*

### 3.1 High-Pressure Piping System

The high-pressure piping system includes a compressor, four horizontal supply tanks, manual valves, pressure relief valves, pressure regulators, and burst disks. Figure 3.6 shows a photograph of a portion of the high-pressure piping system, including the four supply tanks, the pressure relief valves, the high-pressure piping used to fill the tanks, the high-pressure piping that connects the high and low-pressure piping systems, and the low-pressure piping system. The other components in this system are not visible in this image, as they are located behind the supply tanks.



*Figure 3.6: The high-pressure piping system and part of the low-pressure piping system.*

### **3.1.1 High-Pressure Compressor**

A high-pressure compressor pressurizes the high-pressure piping system. The high-pressure compressor is manufactured by Bauer Compressors. It has part number BP26-E3. The high-pressure compressor includes an air dryer and filter. Figure 3.7 shows the high-pressure compressor.



*Figure 3.7: The high-pressure compressor*



### **3.1.2 2500 psi Fill Line**

The compressor pumps air into a  $\frac{3}{4}$  inch diameter pipe called the fill line. A manual valve MV-101, an analog pressure gauge PG-129, a manual venting valve MV-126, and a pressure relief valve RV-130 are installed in the fill line as safety features. The analog pressure gauge is an Acco Helicoid gage with a maximum pressure of 4000 psi. The manual venting valve is a Ham-Let H700SSL1/2TLD ball valve. The pressure relief valve is a Parker R series relief valve with a model number of 4A-RH4A-BNT-SS-K1. The pressure relief valve vents at 2550 psi. These components are shown schematically in Figure 3.2.

Near the supply tanks, the fill line splits into two  $\frac{3}{4}$  inch diameter fill lines. One fill line is used to supply the top two air supply tanks. The second fill line is used to supply the bottom two air supply tanks. Each fill line has a manual valve, MV-118 and MV-119. The manual valves are F26 series ball valves from A-T Controls. The manual valves isolate the top and bottom piping systems. The top and bottom piping systems are functionally identical. Only the bottom system is described here.

### **3.1.3 Air Supply Tanks**

The vertical fill line connects with a horizontal  $\frac{3}{4}$  inch diameter pipe. The horizontal pipe connects the two bottom air supply tanks. The air supply tanks are manufactured by A. O. Smith Corporation. The manufacturer serial number is MV-50405-10. Each air supply tank has a volume of 306.9 cubic feet and is rated to 2826 psig, however, all tanks are not used at the maximum pressure. Referring to Figure 3.8, the high-pressure air supply tanks on the right side of the fill line are pressurized to 2500 psig. The air supply tanks on the left of the fill line are pressurized to 300 psig.



*Figure 3.8: The piping and components connecting the 2500 psi tanks (right), the 300 psi tanks (left), and the fill line (vertical center).*

#### **3.1.4 2500 psi High-Pressure Piping Components**

To the right of the fill line in Figure 3.8, an analog gauge and pressure transducer, PG/PT-117 (116 on the top) measure the pressure. The analog gauge measures pressures as high as 3000 psig. It is manufactured by WIKA. The pressure transducer is a Honeywell FPA transducer with a part number of 060-C860-20. The pressure transducer is capable of measuring pressures up to 3000 psia. The digital pressure transducer is connected to a Honeywell GM-A 4.5 digit digital display. The digital display has a part number of 060-6807-01. The digital displays are located on an electrical rack panel in the wind tunnel control room. The digital displays are shown in Figure 3.9.



*Figure 3.9. The control panel showing the digital displays for the pressure transducers.*

To the right of the pressure gauges, an F26 series manual ball valve manufactured by A-T Controls can be used to vent the air from fill line and 2500 psig tank. This venting valve is labeled MV-114 in the schematic in Figure 3.2. Rightward of the venting valve in Figure 3.8, another F26 series manual ball valve manufactured by A-T Controls isolates the 2500 psi tank. This valve is labeled MV-112. Next, two burst disks, BD-111 and BD-109, and two pressure relief valves, RV-107 and RV-105, prevent over pressurization of the 2500 psi tank. The burst disks are Zook 3008592 burst disks, and have a burst capacity of 2750 psig. The pressure relief valves are manufactured by Kunkle Valves and have a model number of 264MP-E01-KG. The pressure relief valves vent at 4270 SCFM when the pressure exceeds 2500 psig. To the right of the pressure

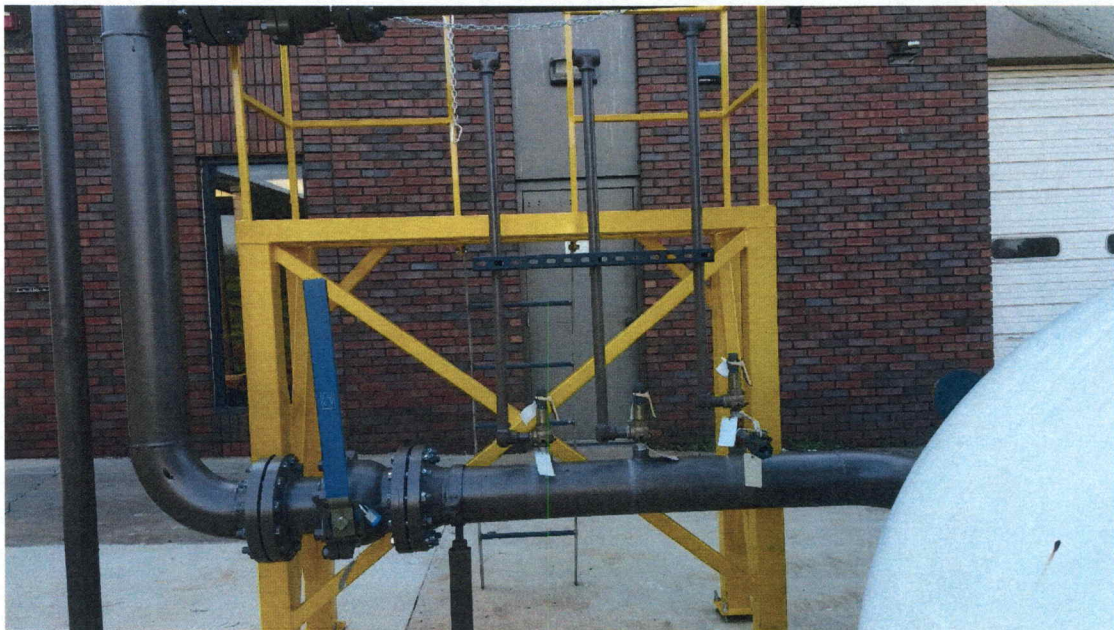
relief valves in Figure 3.8, an analog pressure gauge and digital pressure transducer measure the pressure in the 2500 psig tank. The analog gauge and pressure transducer PG/PT-103 are the same models as the gauge and transducer PG/PT-117. The ¾ inch pipe terminates into the 2500 psig tank after the analog pressure gauge and digital pressure transducer.

To the left of the fill line in Figure 3.8, there is a manual valve MV-121, followed by an analog pressure gauge and digital pressure transducer PG/PT-123. The pressure gauge and transducer are the same types as the ones on the right of the fill line. The next component to the left of the analog gauge and pressure transducer is a pressure regulating valve REG-125. The pressure regulating valve is manufactured by Tescom and has model number 44-1313-2122. It is set to regulate the downstream pressure to 300 psi. Each of the components described appear on the schematic in Figure 3.2 and in the photograph in Figure 3.8.

### **3.1.5 300 psi High-Pressure Piping Components**

Downstream of the pressure regulator, the components are labeled on the schematic in Figure 3.3 and are in the photograph of Figure 3.8. An analog pressure gauge and a digital pressure transducer PG/PT-202 measure the pressure to the left of the pressure regulator. The analog gauge is manufactured by WIKA. It measures pressures up to 600 psig. The transducer is a Honeywell FPA digital transducer. It can measure up to 750 psia. Its part number is 060-C860-15. A Honeywell GM-A 4.5 digit digital display displays the pressure from the transducer in the wind tunnel control room. The display is part number 060-6807-01.

An A-T Controls, F26 series, manual valve is downstream of the pressure gauge and transducer. This manual valve can isolate the 300 psi tank. It is labeled MV-204 in Figure 3.3. An analog gauge and digital pressure transducer PG/PT-206 are located between the manual valve and the tank. The analog gauge is manufactured by WIKA. It measures up to 300 psig. The pressure transducer is the same as the one upstream of the manual valve. The analog pressure gauge and digital pressure transducer measure the pressure in the 300 psi tank.



*Figure 3.10: The piping components downstream of the bottom 300 psi tank. The piping from the top tank is the same as from the bottom tank.*

As shown in Figure 3.10, downstream of the 300 psi tank, 6 inch diameter piping is used. Another analog gauge and pressure transducer PG/PT-208 measure the pressure in the 300 psi tank. The analog gauge is manufactured by Duro United Instruments. It measures pressures less than 300 psig. The transducer is the same as the others downstream of the pressure regulator. A series of three Kunkle 913BDEM03-KE pressure relief valves are downstream of the analog gauge and transducer. These are

called RV-210, 212, and 214 in Figure 3.3. Each relief valve vents 694 SCFM at pressures greater than 310 psig. An A-T Controls, F26 series, manual venting valve, labeled MV-216, is in the same location as the upstream most pressure relief valve, RV-210. This manual valve can be used to vent the 300 psi tank without running the air through the wind tunnel. Downstream of the pressure relief valves, there is a 6 inch manual ball valve, MV-218. This manual valve and the corresponding valve in the top piping system, MV-217, can be used to isolate the top and bottom piping systems downstream of the supply tanks. These components are all shown on the schematic in Figure 3.3 and in the photograph in Figure 3.10.

Downstream of the large manual ball valves, the 6 inch pipes from the top and bottom piping systems connect into one 6 inch pipe. This connection is shown in Figure 3.11. The pipe connects the high-pressure piping system to the low-pressure piping system. Directly upstream of the junction with the low-pressure piping system, a WIKA analog gauge measures pressures up to 300 psig.



*Figure 3.11: Piping system connection*

### 3.2 Low-Pressure Piping System

The low-pressure piping system consists of an air compressor, a small manual valve, a vertical supply tank, a series of pressure relief valves, and a manual gate valve. These components are all upstream of the connection with the high-pressure piping system. After the connection to the high-pressure piping system, the low-pressure piping system has a pneumatic valve, a pressure regulating valve, and an air diverter plenum. Pressure gauges are located at various positions throughout the piping system. A photograph of the low-pressure piping system is presented in Figure 3.12. All components in the low-pressure piping system are shown schematically in Figure 3.4.



Figure 3.12: Photograph of the low-pressure piping system.

### 3.2.1 Low-Pressure Compressor

The vertical supply tank is filled using an air compressor with an air dryer. The compressor is manufactured by Quincy Compressor. Its model number is Quincy QR 350 model BM350HPDT. This compressor can pressurize air to 300 psig. The air drier is manufactured by ZEKS. Its model number is 75NDQCA100. The compressor and dryer are shown in Figure 3.13. Manual valves MV-305 and 306 separate the compressor from the vertical air supply tank. The manual valves are manufactured by Ham-Let and have model number H700SSL3/4TLD. During testing, the compressor is turned off, and the valves are closed. Hence, the type of compressor used to pressurize the supply tank should not affect the test results.



*Figure 3.13: The air compressor and dryer used in the low-pressure piping system.*



### 3.2.2 Vertical Supply Tank

The compressor fills the vertical supply tank. The vertical supply tank is manufactured by Taylor Forge. It holds 500.7 cubic feet of air and is rated to hold pressures as large as 300 psig. The vertical supply tank is shown in Figure 3.14.



*Figure 3.14: The 300 psig vertical supply tank*

### 3.2.3 Low-Pressure Piping System Components

As shown in Figure 3.15, an analog pressure gauge and a Honeywell digital pressure transducer PGA/PT-01 are installed in a 6 inch diameter pipe that connects to the vertical supply tank. The analog gauge and digital transducer measure the pressure in the tank. The analog pressure gauge is manufactured by Duro United Instruments. It can measure up to 300 psig. The digital transducer is a Honeywell FPA transducer with a part

number of 060-C860-15. The transducer can measure pressures less than 750 psia. All of the digital pressure transducers are the same in the low-pressure piping system.



*Figure 3.15: The analog and digital pressure gauges that measures pressure in the vertical supply tank, the six pressure relief valves, and the manual gate valve on the low-pressure piping system.*

Three pressure relief valves RV-308, 309, and 310 are located downstream of the 500.7 cubic foot air supply tank. The pressure relief valves are manufactured by Kunkle Valves and have model number 913BFEM03. These pressure relief valves will open when the pressure in the piping reaches 310 psig. Each pressure relief valve can exhaust 1929 SCFM. The pressure relief valves are included in the piping system as a safety feature. They are not intended to be open during testing.

Downstream of the pressure relief valves, a manual gate valve MV-311 holds the air in the supply tank when testing is not underway. The manual gate valve is manufactured by Newco and has model number N36426. The manual gate valve is fully opened prior to testing.

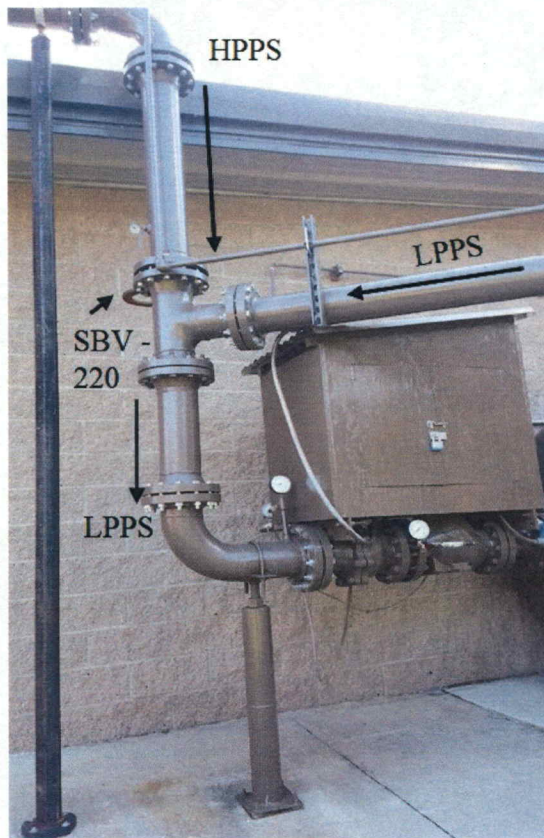
Three pressure relief valves RV-312, 313, and 314 are located downstream of the manual gate valve. These are identical to the pressure relief valves upstream of the manual gate valve. The pressure relief valves and the manual gate valve are shown in Figures 3.15 and 3.16, and schematically in Figure 3.4.



*Figure 3.16: The six pressure relief valves and the manual gate valve on the low-pressure piping system.*

#### **3.2.4 Connection of the Low and High-Pressure Piping Systems**

The high-pressure piping system and low-pressure piping system connect downstream of the relief valves. Figure 3.17 shows this connection. The spectacle blind valve, SBV-220, can be in the closed position to separate the high-pressure piping system and low-pressure piping system. It is in the closed configuration in Figure 3.17. It can also be moved to the open position to allow air flow from the high-pressure piping system into the low-pressure piping system.



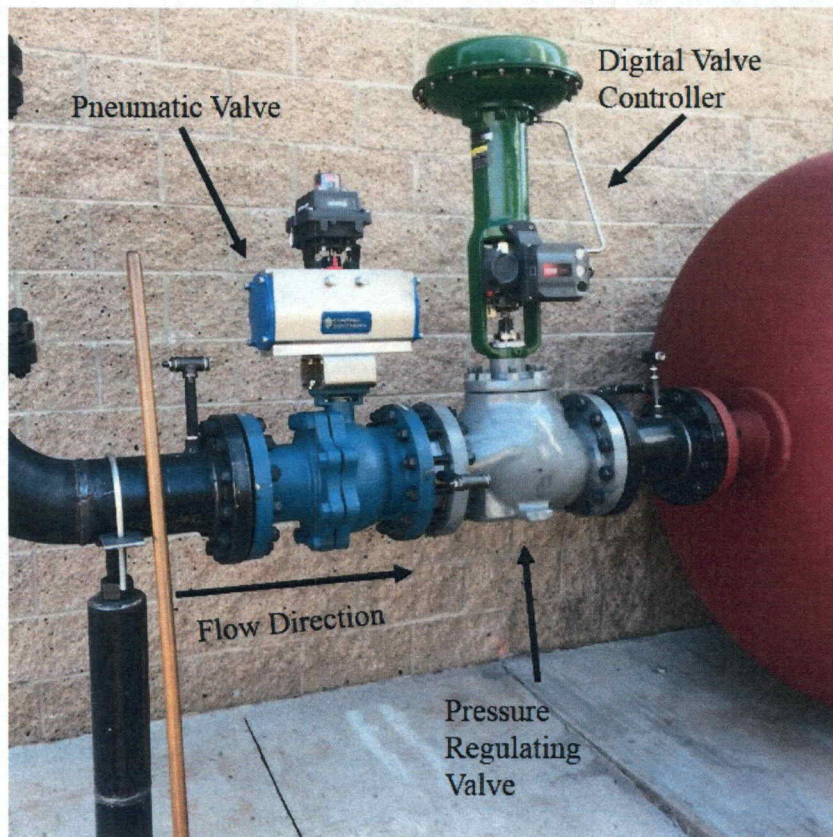
*Figure 3.17: The connection where the high-pressure piping system joins the low-pressure piping system.*

### **3.2.5 Air Flow Control Components**

Downstream of the connection between the high and low-pressure piping systems, an analog pressure gauge and digital pressure transducer PGA/PT-2 measure the pressure. The analog gauge is manufactured by Ashcroft. It can measure pressures as great as 300 psig.

A pneumatic ball valve PBV-315 is downstream of the gauge and transducer. This valve is assembled by Southern Controls and is comprised of a 6 inch ball valve, a pneumatic actuator, a switch, and a solenoid. The 6 inch ball valve is manufactured by Trueline. It has model number 330AITFM-CH-SQ. The actuator, switch, and solenoid

are manufactured by CSS and have model numbers of VAD09, M, and 4, respectively. The switch is located on the electrical rack panel in the wind tunnel control room. The pneumatic valve is fully open during testing and fully closed otherwise. The pneumatic valve is shown in Figure 3.18.

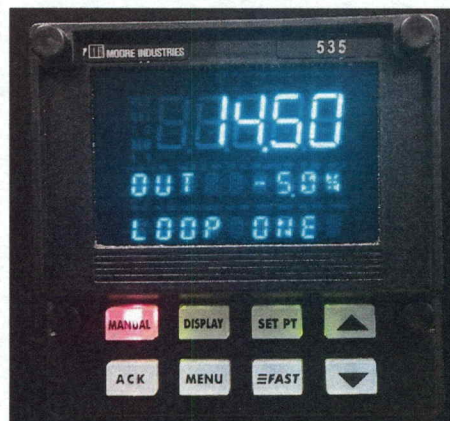


*Figure 3.18: The pneumatic valve and the pressure regulating valve. A padlocked box typically encloses these components.*

Another Ashcroft analog pressure gauge and digital pressure transducer PGA/PT-3 measure the pressure downstream of the pneumatic valve.

Next is a pressure regulating gate valve PGV-316. The pressure regulating valve is a 6 inch 667-EWT-DVC6200 Fisher Valve. The pressure regulating valve is controlled by a Fisher FIELDVUE DVC6200 Digital Valve Controller. The digital valve controller is set to maintain a constant downstream pressure whatever is set using the Moore

Industries Inc. controller display. It is set to 60 psi during these tests. The pressure downstream is measured using a pressure transmitter manufactured by Rosemount with part number 3051S2TA2A2E11A1AM5. The pressure regulating valve and the digital valve controller are shown in Figure 3.18. The digital valve controller settings are programmed into a display that is mounted on the electrical panel in the control room. The display is manufactured by Moore Industries and has part number 535. Figure 3.19 shows the input display to the digital valve controller. Some of the settings to the digital valve controller are listed in Appendix A.

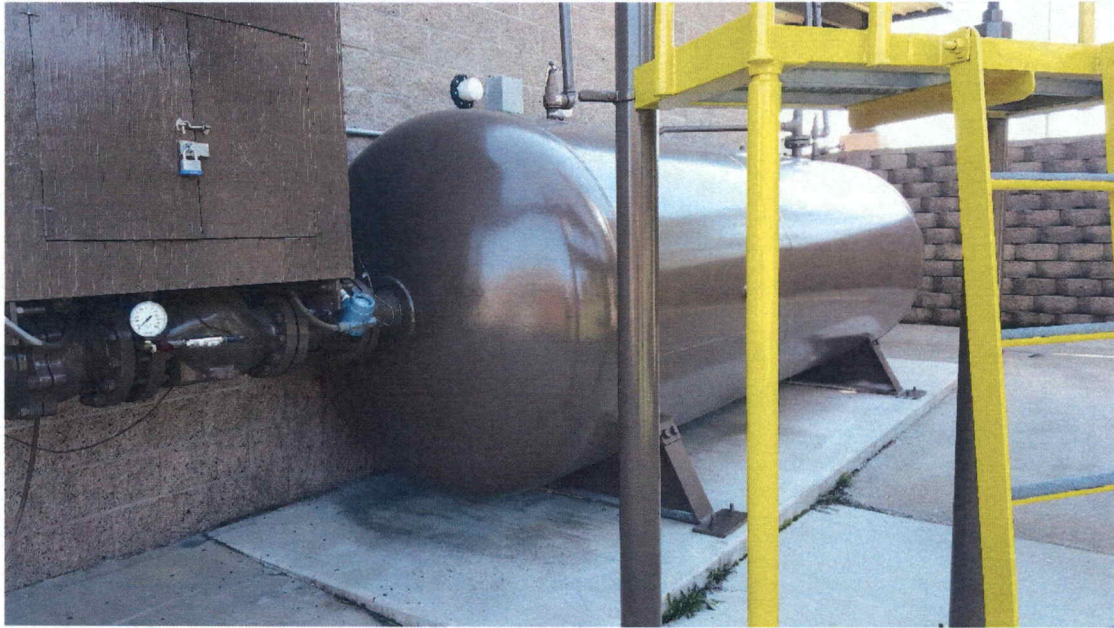


*Figure 3.19: The interface with the digital valve controller.*

An analog pressure gauge and a digital pressure transducer PGA/PT-4 are located downstream of the pressure regulating valve. The output from this digital pressure transducer is recorded using a LabVIEW code as well as is displayed on the electrical rack in the control room. The code will be described in Chapter 4.

The final component in the low-pressure piping system is a diverter plenum, shown in Figure 3.20. The diverter plenum holds approximately 428 cubic feet. The diverter plenum ensures that any disturbances that occur in the piping system do not propagate to the test section. The diverter plenum has three air output pipes. These three

pipes pass through the wall and into the building. They lead to three independent test sections.



*Figure 3.20: The air diverter plenum.*

### **3.3 Test Sections**

Only one of the three test section branches is used in the present research effort. The entrances to the other two sections are blocked by a closed spectacle blind valve and by a circular sliding gate valve. The branch of the wind tunnel that is used in this research is shown and labeled in the photograph in Figure 3.21 and schematic diagram in Figure 3.22. The air passes through an open spectacle blind valve into the inlet duct. From there, the flow is accelerated through a converging diverging nozzle into the test section. After the test section, the air decelerates to the exhaust plenum. Finally, the air exits the facility through exhaust duct-work.

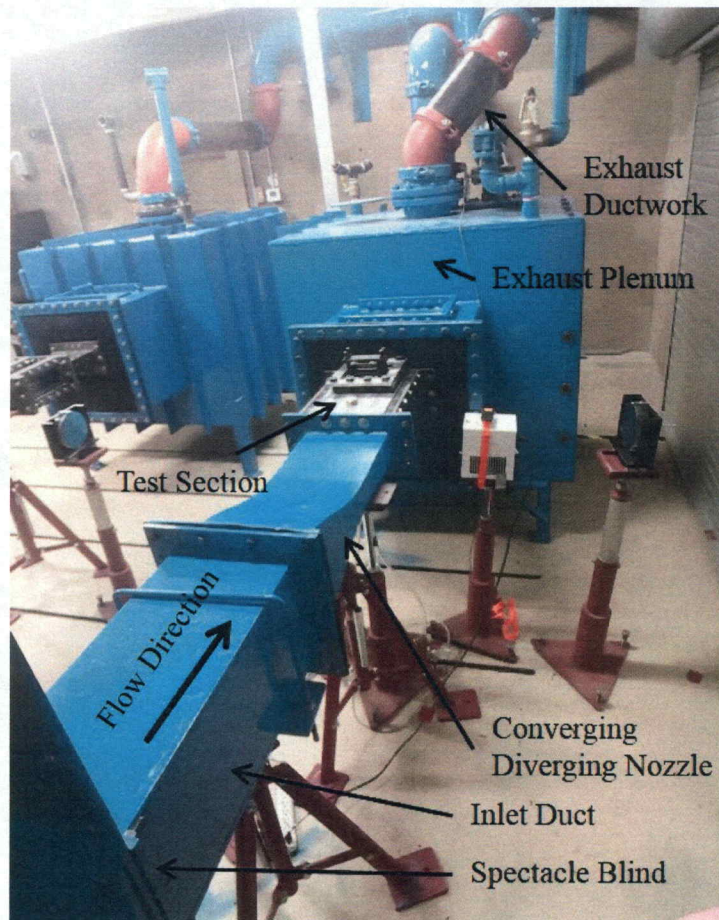


Figure 3.21: The branch of the wind tunnel used for this research.

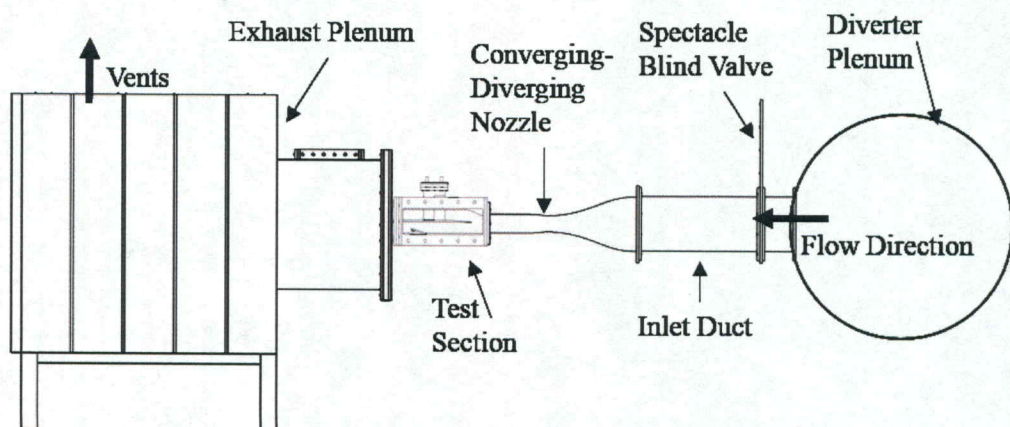


Figure 3.22. Schematic Diagram of the branch of the test section used for this research.



### 3.3.1 Inlet

A square cross sectional duct is welded to the diverter plenum. This allows a 10.635 inch square flow area. This duct goes through the wall of the supersonic wind tunnel laboratory. A smaller square duct, with an inner side dimension of 9.635 inches, is inserted inside the 10.635 inch square duct. The two ducts are connected using a bolted flange that also blocks airflow from the larger square duct. Air is present between the two ducts, but there is no flow in this region. The smaller insert protrudes two inches into the diverter plenum. This is intended to create a more uniform flow through the 9.635 inch square duct. Figures 3.23 and 3.24 show a photograph and a schematic diagram of the two ducts. The 9.635 inch insert also connects to the spectacle blind valve and the inlet duct. During the wind tunnel tests, the spectacle blind valve is open to permit air to flow through this branch of the wind tunnel.



*Figure 3.23. A photograph of the connection between the 10.635 inch duct and 9.635 inch square insert.*

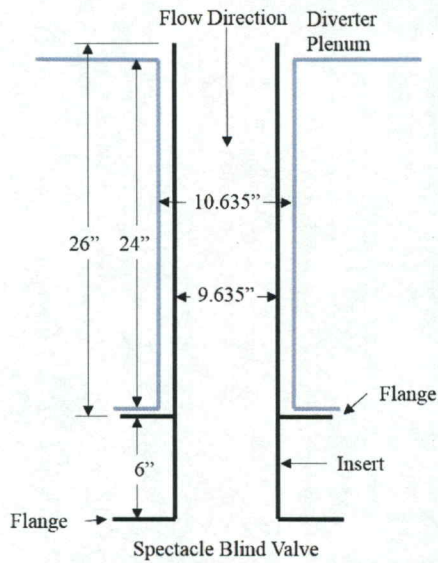


Figure 3.24. Top view of the inlet to the branch of the wind tunnel from the diverter plenum used in the current research.

A schematic drawing of the spectacle blind valve is shown in Figure 3.25. The spectacle blind valve is a ½ inch thick sheet of steel. It is in the open position, so the 9.635 inch square hole is the entrance to the inlet duct.

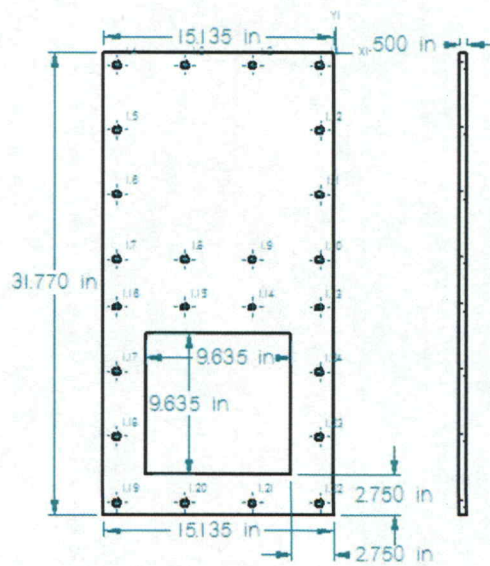


Figure 3.25: Inlet spectacle blind valve

The inlet duct, drawn in Figure 3.26, is a constant-area square duct that is located downstream of the spectacle blind valve. It is 24 inches long including the thickness of the flanges. Thin 1/8<sup>th</sup> inch neoprene sheets are adhered to the flanges of the inlet duct. The neoprene sheets prevent leaks and provide strain relief from thermal expansion and contraction during tests. The inlet duct is bolted to the converging diverging nozzle.

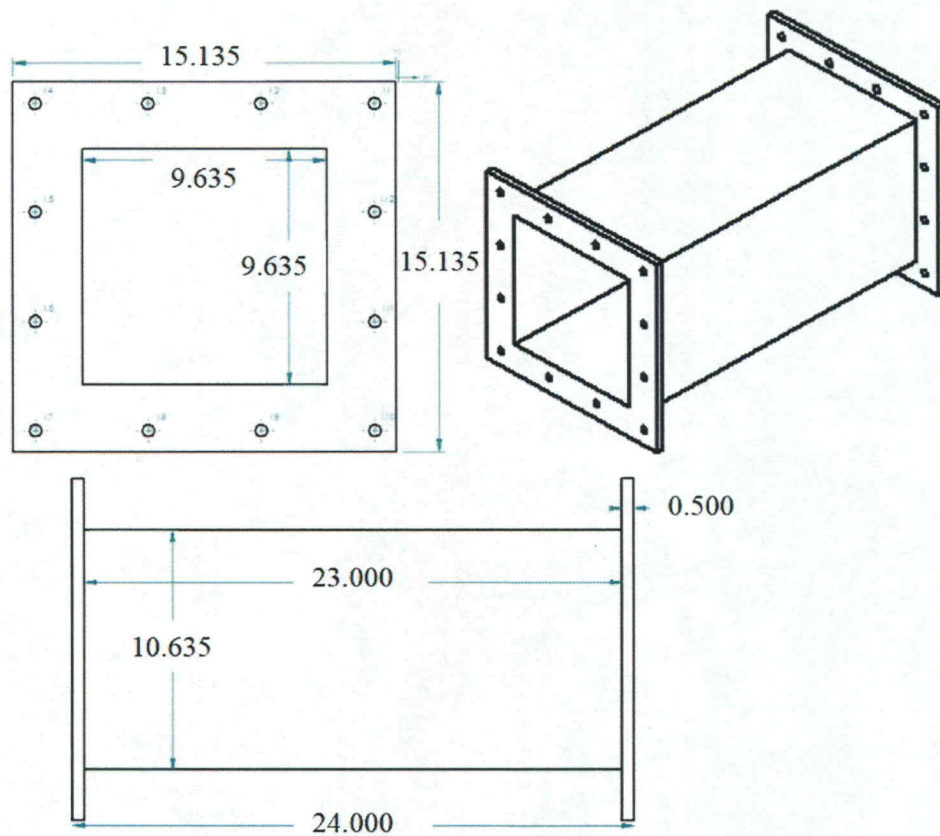


Figure 3.26: Technical drawing of the inlet duct.

Figure 3.27 shows the inlet to the nozzle. Note that the flange and opening at the entrance to the nozzle have the same dimensions as the exit to the inlet duct. The entrance of the nozzle is also tangent to the exit of the inlet duct such that there are no discontinuous surfaces or sharp angles that could disturb the flow.

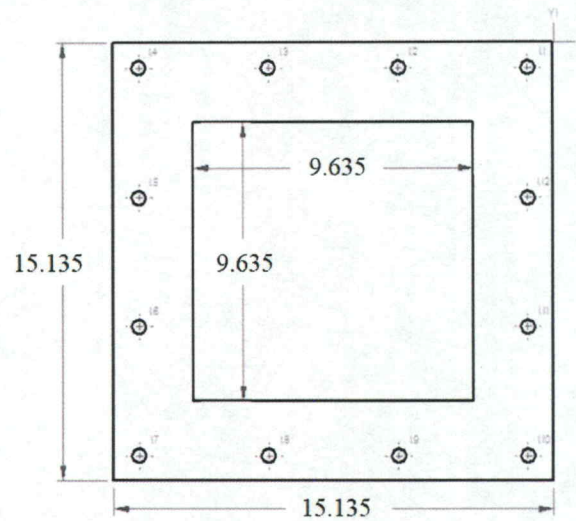


Figure 3.27: The inlet to the nozzle that connects with the inlet duct as viewed from upstream.

### 3.3.2 Nozzle

The converging diverging nozzle is shown in Figure 3.28. The width of the nozzle is a constant 9.635 inches throughout its length. The height is 9.635 inches at the entrance. The flow is choked with a nozzle height of 2.204 inches. The nozzle diverges gradually to an outlet height of 2.7 inches. Note that these dimensions are measured from the inside of the nozzle; they do not include the thickness of the nozzle walls. The nozzle is 30 inches long.

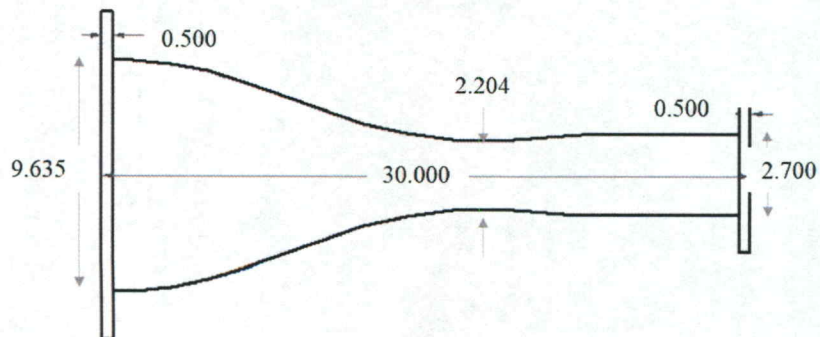


Figure 3.28: Side view from a technical drawing of the converging diverging nozzle. Flow enters from the left.

A plot of the contour of the inner surface of the nozzle measured from the centerline is shown in Figure 3.29. It is designed to match the contour of a fifth-order polynomial. The nozzle is symmetric across the horizontal centerline.

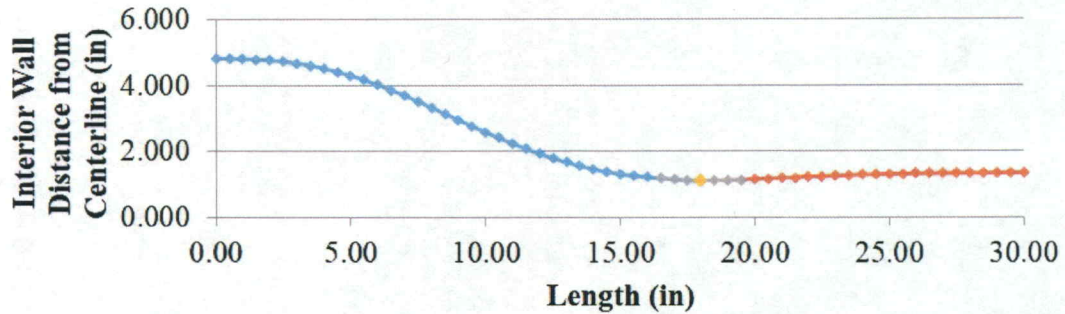


Figure 3.29: Plot of the vertical interior wall distance of the nozzle measured from the centerline of the nozzle with respect to distance from the nozzle entrance. The nozzle is symmetric across the centerline. The width is 9.635 inches.

Figure 3.30 shows a drawing of the outlet to the nozzle. This is the same as the entrance to the test section. The nozzle is tangent to the test section at this location. All-purpose putty is applied to the internal joints between the nozzle outlet and the top and bottom walls of the test section entrance. The putty is part number 20052, manufactured by 3M Bondo. The putty that is applied to these joints is sanded using 320 grit sandpaper until the joints are completely smooth.

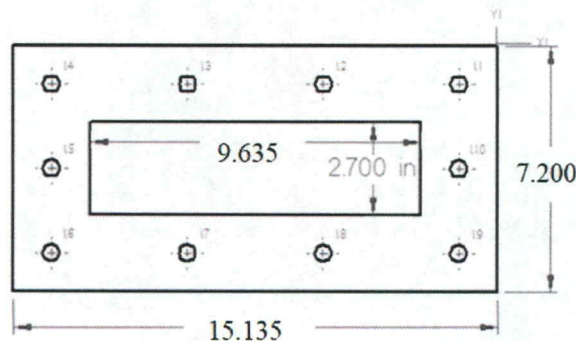


Figure 3.30: The exit to the converging-diverging nozzle that connects with the test section as viewed from downstream.

Figure 3.31 is a photograph of the test section, nozzle, and inlet duct as they are assembled in the wind tunnel. The nozzle and inlet duct are supported with custom made stands. The stands are made by Nicole Tool and Die and are visible in Figure 3.31.



*Figure 3.31: The nozzle and test section.*

### **3.3.3 The Test Section**

The test section contains a shock wave holding plate and a choking flap. The test section is made from a flat bottom wall, a diverging top wall, and two side walls. During tests, a shock wave is generated near the tip of the shock wave holding plate. The position of the shock wave holding plate is measured using digital calipers. The choking flap is angled so that it chokes the flow that is beneath the shock wave holding plate.

To determine the angle of the choking flap, a picture is taken of the test section. The picture is taken using the camera on a Samsung Galaxy Note 5 cellular phone. The picture is opened in Microsoft Paint. Microsoft Paint displays the pixel locations of the tip and the base of the choking flap when the mouse is hovered over those positions. Two pixel locations on the surface of the bottom wall are also determined using this method. Trigonometry is used to calculate the angle of the choking flap relative to the bottom wall based on these four pixel locations. Figure 3.32 shows an example image denoting the locations used in this calculation. In some tests, the physical height of the choking flap is also measured using digital calipers.



*Figure 3.32: An example image showing the choking flap angle calculation.*

Figure 3.33 shows a photograph of the test section as it is configured for the wind tunnel tests on 04 and 05 April 2018. Figure 3.34 shows the test section for these tests schematically. The same general configuration is used in all tests, however the placement of the shock wave holding plate and the angle of the choking flap vary among tests. Note that the photograph and the schematic show the test section viewed from opposite sides: in the photograph in Figure 3.33, flow enters from the right; in the schematic in Figure 3.34, flow enters from the left.

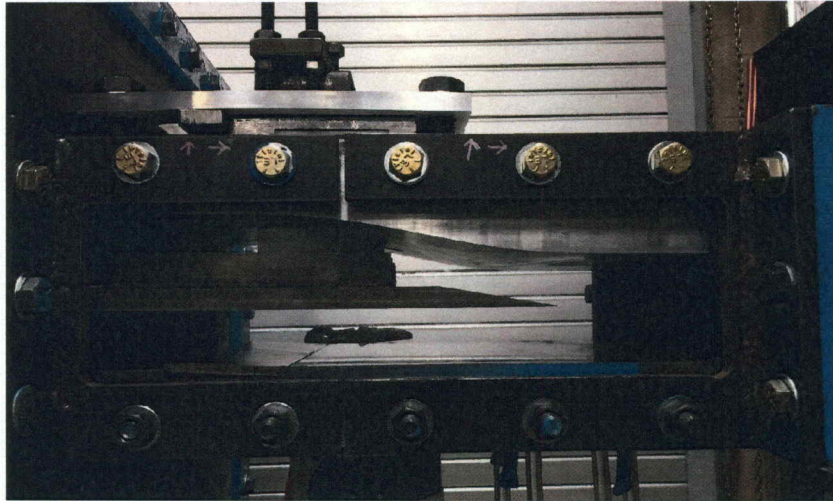


Figure 3.33: A photograph of the test section. Flow enters from the right.

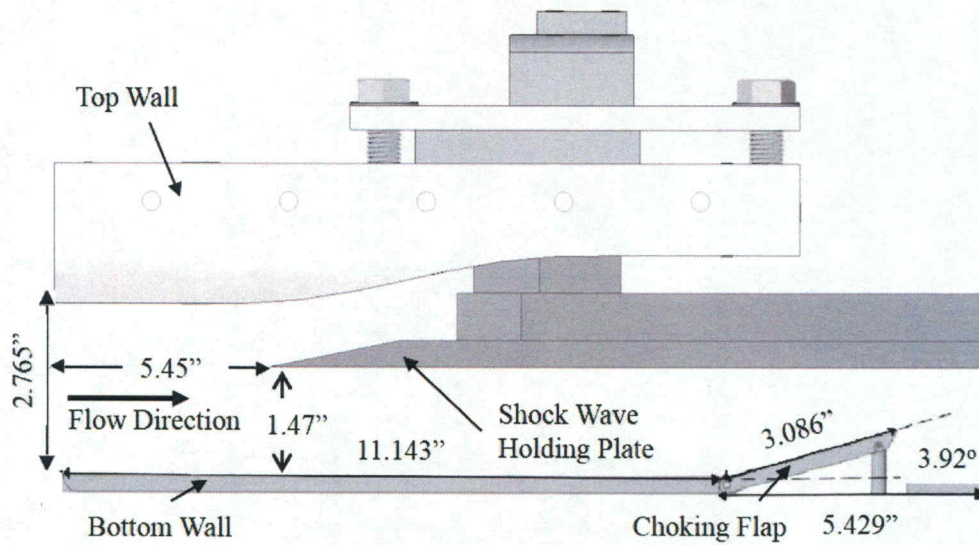


Figure 3.34: Schematic diagram of the test section. The dimensions shown correspond to the configuration for the tests on 04 and 05 April 2018.

The top wall of the test section diverges. Figure 3.35 shows an orthographic projection of the top wall. Figure 3.36 is a plot of the contour of the top wall. The top wall begins diverging at a location 3.800 inches into the test section. It stops diverging 4.45 inches before the test section exit.



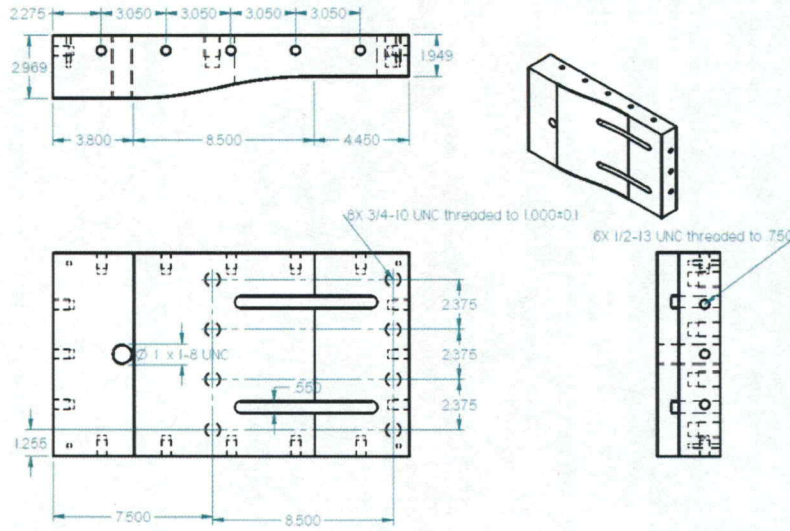


Figure 3.35: Drawing of the top wall of the test section.

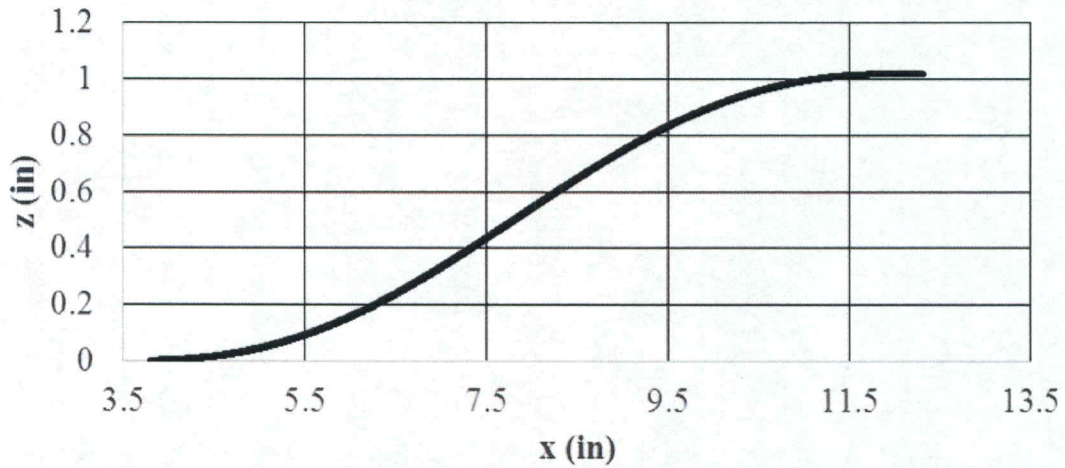
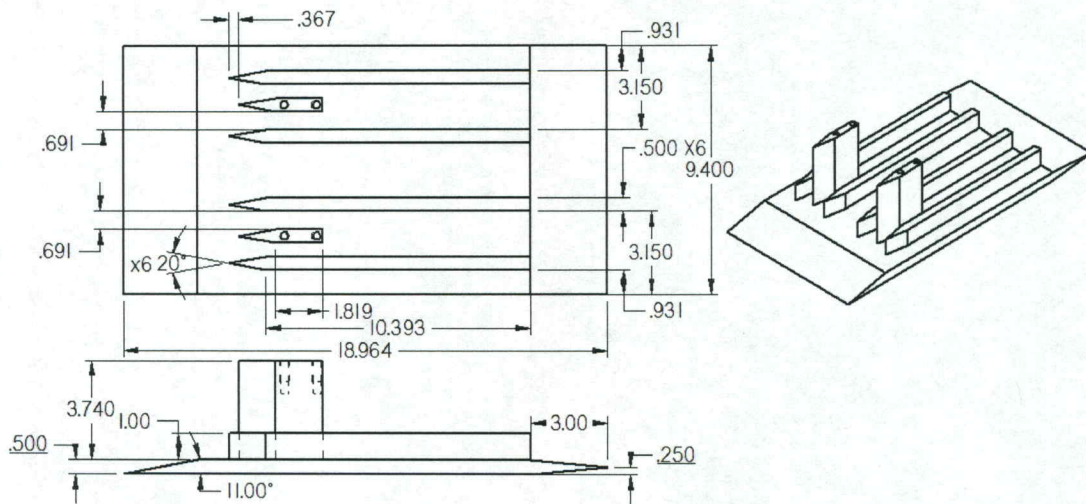


Figure 3.36: Vertical profile of the top wall with respect to the distance from the entrance to the test section.

The final version of the shock wave holding plate is dimensioned in Figure 3.37. The bottom of the shock wave holding plate is flat. At the leading edge of the shock wave holding plate, the top of the plate makes an angle of  $11^\circ$  with respect to the bottom of the plate. Several structural supports and mounting struts are located along the top of the shock wave holding plate to minimize deflection in the shock wave holding plate.



*Figure 3.37: The final design of the shock wave holding plate and supports. In this diagram, flow would enter from the left.*

### 3.3.4 Exhausting the Flow

Downstream of the test section, the exhaust plenum diffuses the air. Figures 3.38 and 3.39 are drawings of the exhaust plenum. The surface of the plenum that connects to the test section is a ½ inch thick sheet of neoprene. A steel plate is mounted to the back of the neoprene to provide additional support for the test section walls. The remaining walls of the exhaust plenum are ½ inch thick steel. Figure 3.38 shows the top view of the plenum. It illustrates the locations of the two 8 inch diameter exhaust duct holes, two 1.5 inch diameter holes, and an 8 inch square hole.

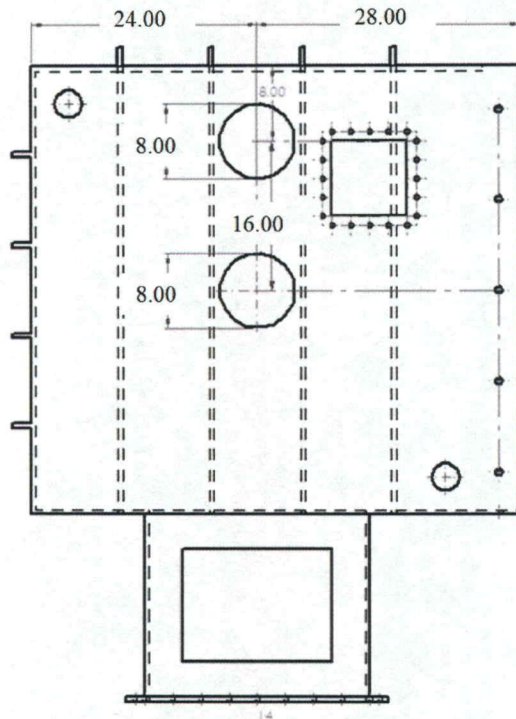


Figure 3.38: Top view of the exhaust plenum.

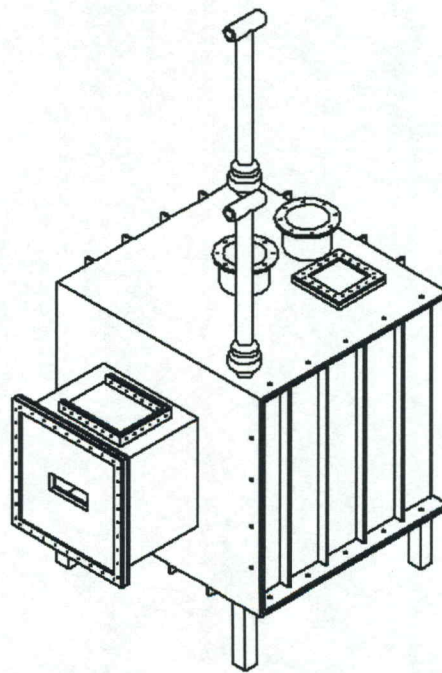
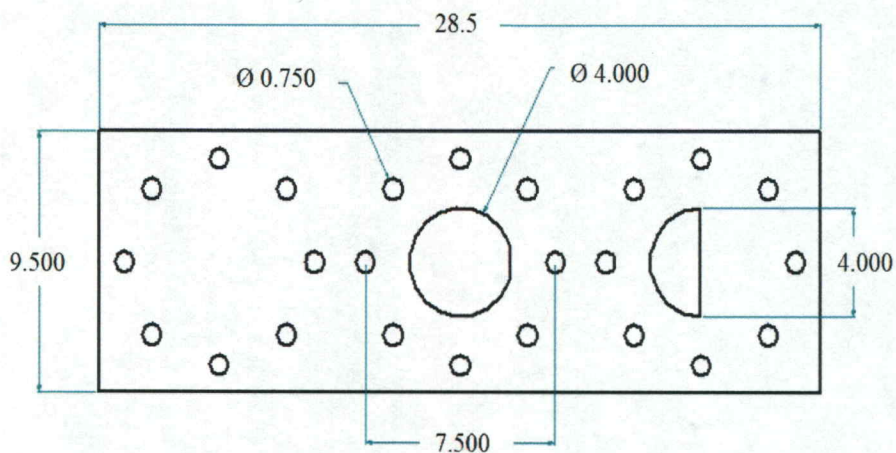


Figure 3.39: Isometric view of the exhaust plenum.

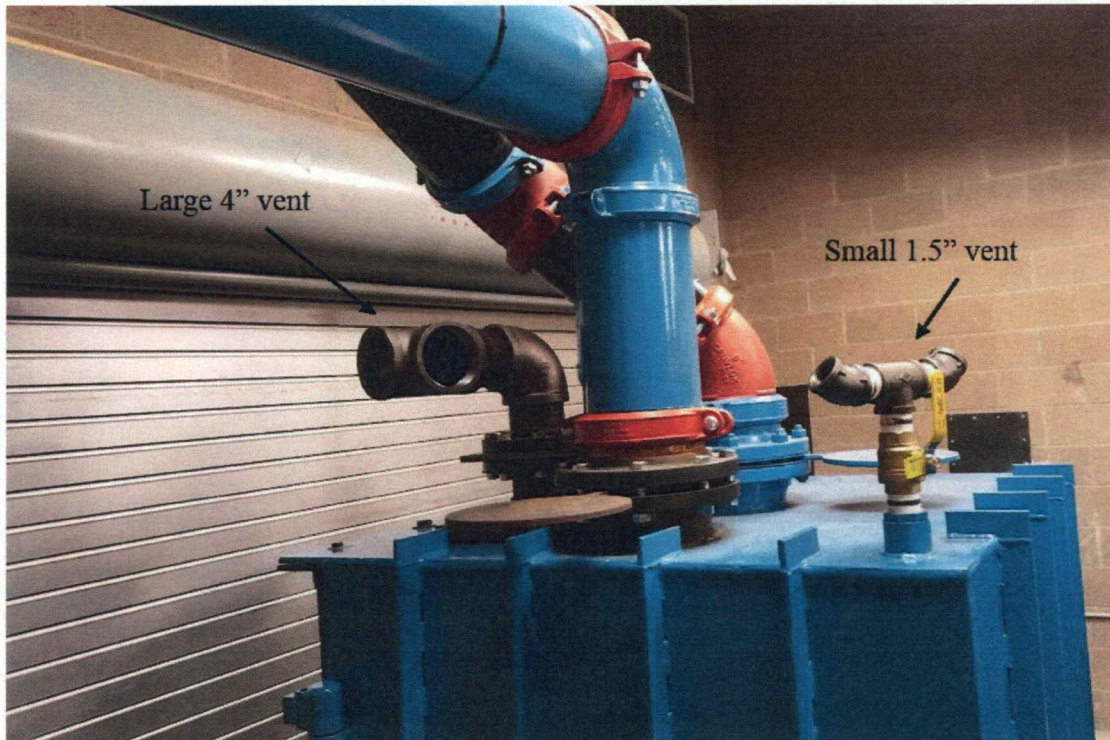
One of the two 1.5 inch diameter holes is used as a small 1.5 inch diameter vent; the other goes to a pressure relief valve and burst disk. The pressure relief valve is Kunkle Valve 6010HGM01-NM, and the burst disk is Zook type RA-4. The pressure relief valve exhausts 355 SCFM at pressures above 10 psig. The burst disk will rupture at 20 psig.

The square hole is designed as an instrumentation port, however, it is modified to be a large 4 inch diameter vent. The 4 inch diameter vent can be fully open, partially open, or fully closed by moving a spectacle blind valve. A drawing of the spectacle blind valve is shown in Figure 3.40.



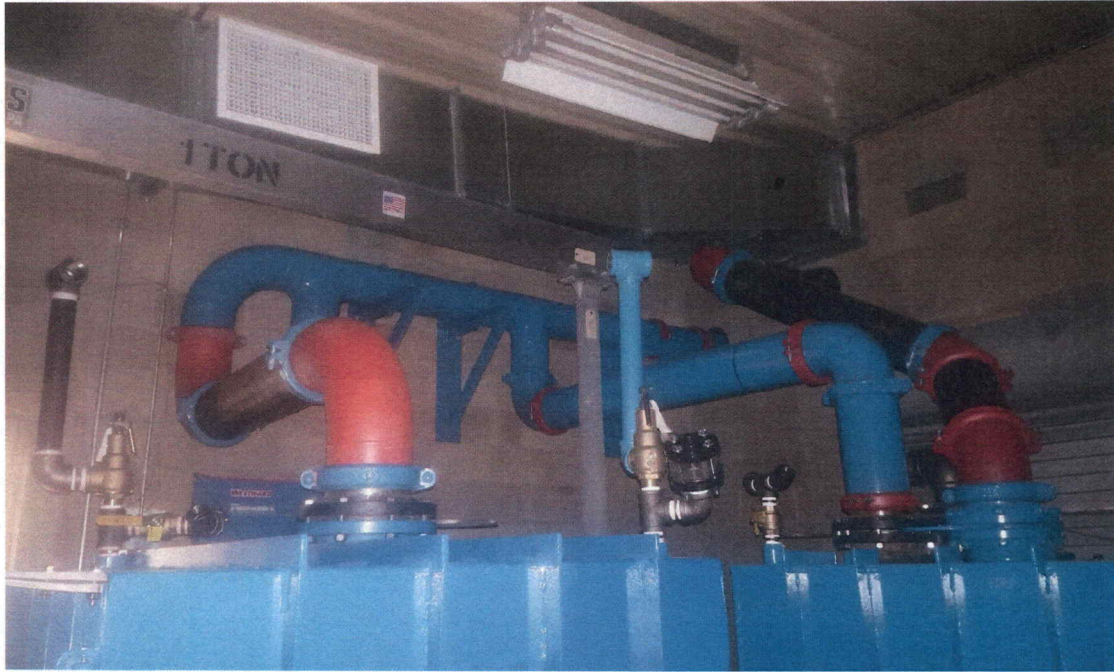
*Figure 3.40: The spectacle blind valve for the 4 inch diameter vent. The spectacle blind valve can be fully closed, fully open, or half open.*

The Figure 3.41 is a photograph of the exhaust plenum with the exhaust ducts and vents attached. The 1.5 inch and 4 inch diameter vents vent inside the building. The two 8 inch diameter ducts exit the building to vent the air outside.



*Figure 3.41: The exhaust piping attached to the downstream exhaust plenum.*

The first 8 inch exhaust ducts is centered in the exhaust plenum. This duct contains two 45° bends, one 90° bend and 30 feet of straight 8 inch diameter groove lock piping. The second 8 inch exhaust duct has two 90° bends and 8 feet of straight piping upstream of a tee connection. The tee connects the exhaust from this test section to the exhaust from another test section. A closed spectacle blind valve is used when needed to block air from passing between the two test sections. The exhausts exit outside the building through 25 feet of straight 8 inch diameter pipe. Figure 3.42 shows a photograph of the exhaust piping inside the building. The plenum and exhaust ducts on the right side of the photograph are the ones used during the tests.



*Figure 3.42: Exhaust Piping inside the building*

Outside of the building, a tee connection separates the second 8 inch diameter exhaust duct into two 8 inch ducts. Each of those two ducts then turns 90°. Each of the three ducts contains a noise baffling segment. The noise baffles are part number A1602302, manufactured by The New York Blower Company. The noise baffles have inner diameters of 8 inches and bolt to the 8 inch exhaust ducts with flanges. The noise baffles are 3 feet in length. Downstream of the noise baffles, each exhaust pipe has a straight pipe segment 8 inches in length and a 45° bend. Figure 3.43 shows the exits to the exhaust ducts and the noise baffles. Eight inch diameter end caps are inserted into the exits of the exhaust pipes when testing is not underway. These are H/P 0910133409 cap plugs. They keep debris and other undesired items out of the exhaust pipes to help ensure that a blockage does not form.



*Figure 3.43: Exhaust piping for the wind tunnel facility.*

## **CHAPTER 4. DATA ACQUISITION**

Wind tunnel tests are characterized by pressure data and flow visualization images. The locations of the measurement, apparatus, and techniques used to acquire these data are discussed within this chapter.

### **4.1 Pressure Data Acquisition**

During wind tunnel tests, static pressures are measured and recorded in various locations throughout the wind tunnel. Pressures are measured using transducers. The data is processed and saved using a National Instruments data acquisition device and LabVIEW code.

#### **4.1.1 Pressure Measurement Locations**

Inside the test section, there is an array of static pressure taps. Honeywell FPA pressure transducers of part number 060-C54985172080 measure the static pressure from those taps. Figure 4.1 shows an image of the pressure taps with some of the transducers attached. There are 15 pressure taps in the bottom wall of the test section. The pressure taps are arranged according to Figure 4.2. 4.2 shows a drawing of the bottom wall of the test section. The dots indicate locations of pressure taps. The four dots that are circled are the pressure taps with transducers connected. The taps with the transducers are along the centerline of the test section. The remaining taps are plugged, as can be seen in Figure 4.1. A fifth pressure transducer measures atmospheric pressure in the laboratory.



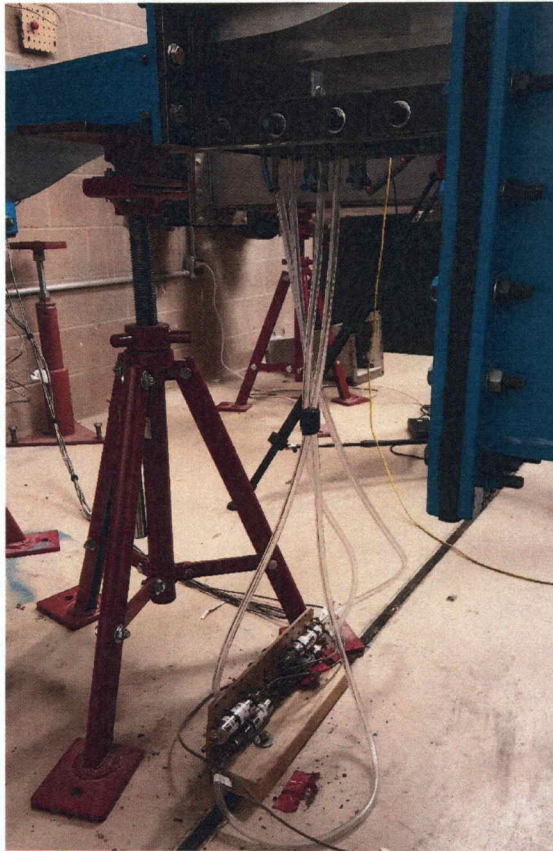


Figure 4.1: The pressure taps and transducers located along the bottom wall of the test section.

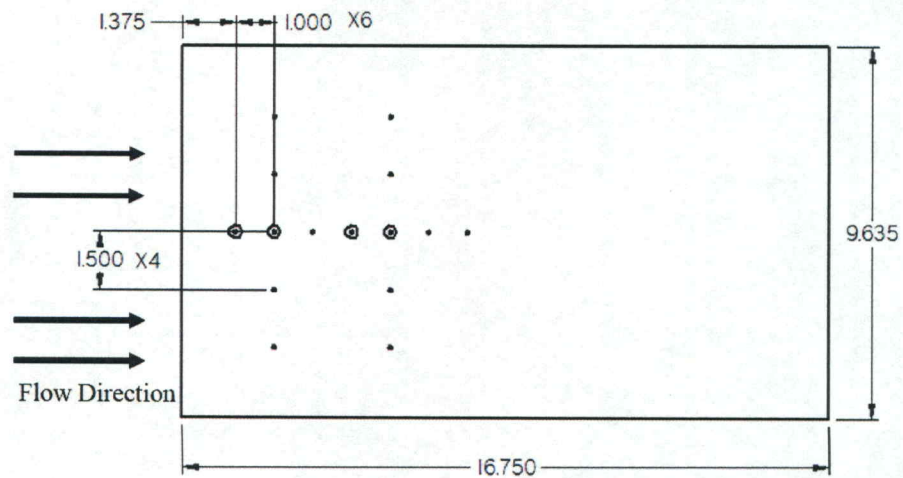
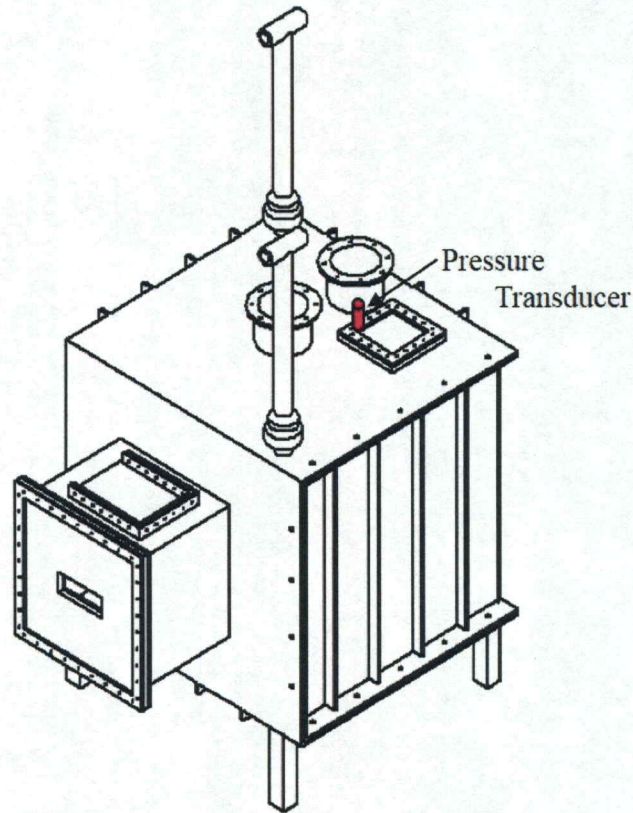


Figure 4.2: The bottom wall of the test section. The used pressure taps locations are circled.

Pressures are also measured in the exhaust plenum. Figure 4.3 shows the location of the transducer that measures the exhaust plenum pressure. This transducer is a Honeywell FPA transducer of part number 060-C860 with a pressure range up to 30 psia.



*Figure 4.3: The location of the pressure transducer that measures the pressure in the exhaust plenum.*

The pressure downstream of the pressure regulating valve in the low-pressure piping system is recorded during tests as well. This pressure can be used as an approximation of the stagnation pressure at the entrance to the test section.

#### **4.1.2 Pressure Data Acquisition Hardware**

Each of the transducers is wired into a National Instruments terminal block, NI 9923. The terminal block transmits the differential analog signals from the transducers to a National Instruments Voltage Input Module, NI 9209. The voltage input module

accepts up to 16 differential connections or 32 single ended connections. Seven differential connections are used; one for each transducer. The voltage input module has a maximum sampling frequency of 500 Hz aggregate. This means that the maximum sampling frequency of an individual channel is equal to the maximum aggregate rate, 500 Hz, divided by the number of channels used. The module is installed within a National Instruments CompactDAQ USB Chassis, NI cDAQ-9174. Together, the voltage input module and the Compact DAQ USB Chassis convert the analog voltage signal from the transducers into a digital signal readable by LabVIEW 2015 Full Development System version 15.0f2 software.

#### **4.1.3 Pressure Data Acquisition Software**

LabVIEW 2015 Full Development System version 15.0f2 code is used to sample, display, and record the pressure data. When a user runs the code, the DAQ Assistant Express VI subroutine is employed first. The DAQ Assistant Express VI subroutine uses NI-DAQmx to collect the digital voltage data from the Compact DAQ. The data is sampled continuously at a rate of 50 Hz, in most tests. This system uses a multiplexed scanned sampling mode. Some modifications to the code during the later tests allow for faster sampling rates, however the data is only accurate up to the 500 Hz aggregate digitization rate. The maximum sampling rate used in any test is 120 Hz while reading only 4 of the 7 channels. Data are collected and stored in LabVIEW until the user presses the “Stop, Hammer Time” button on the graphical user interface (also called the front panel). This button has a latch when released mechanical action, so it remains pressed until its value is used by the code.

Once all the voltage data are collected, “Configure Scaling and Mapping” express VI subroutines convert the voltage signals to pressure signals in psia. Each channel has its own “Configure Scaling and Mapping” express VI subroutine, since they are all uniquely calibrated.

Each transducer is calibrated by Honeywell before shipment to UAH. The rated range of pressures corresponds to a rated range of output voltages, typically from 0 V to 5 V. Because of the voltage drop due to resistance in the wires connecting the transducers to the data acquisition chassis and digital displays, the same voltage to pressure ratio cannot be accurately applied to convert voltage signals back to pressures. In order to calibrate the complete pressure acquisition system, a known pressure, such as atmospheric pressure, is applied to each transducer. The voltage from the “DAQ Assistant” Express VI subroutine and the applied pressure are recorded. A second pressure is applied and the output voltage is recorded. This pressure should be near the maximum rated pressure of the transducer. For the transducers rated to high-pressures (greater than 100 psig), 100 psig is applied. A linear relationship between pressure and voltage is calculated from these two calibration points. This relationship is entered into the “Configure Scaling and Mapping” Express VI. Note that a similar process is used to calibrate the digital displays to the transducers. While the displays are set to calibration mode, pressure is applied to the transducers and the pressure value is manually entered into the display. Again, two pressures must be entered. The conversion from voltage to pressure is internal to the display.

Once represented as pressures, the signals in the pressure acquisition software are converted from arrays of waveform signals to arrays of double precision floating point

values. The data in these arrays are plotted on the front panel in LabVIEW. The “Write to Measurements File” express VI writes and saves the raw voltage and the pressure data to a Microsoft Excel spreadsheet. Microsoft Excel 2013 is used. The user can also enable a data export process by clicking the “Data Export” switch on the front panel. The switch will be displayed in green if the data will be exported. It has a switch when pressed mechanical action. If the user enables the data export process, Labview uses a “System Exec VI” subroutine that calls a batch process file. The batch process uses MATLAB R2015b to plot the pressure data in both a MATLAB figure and in the Microsoft Excel spreadsheet. With the “DataExport” switch enabled, the Mach number is calculated at the entrance to the test section based on the Rayleigh-pitot formula. The pressure data from the upstream most static pressure tap and the fifth transducer are used in the calculation. The fifth transducer should be connected to a pitot-static-probe positioned downstream of pressure tap 1 and upstream of the shock wave for this approach. During the current test sequence, the Honeywell FPA 060-C54985172080 transducer is measuring atmospheric pressure, not a stagnation pressure in the test section, so the results of the inlet Mach number calculation are spurious. The LabVIEW program stops when all data has been processed and saved.

## **4.2 Visualization System**

A shadowgraph system is used to visualize the shock wave structure during most wind tunnel tests. The details of this system are explained in the following sections.

### **4.2.1 Visualization System Instrumentation**

A shadowgraph system captures the changes in density of the flow features in the test section as a time sequence of digitized images. As is described by Settles [26], light

changes speed and direction as it encounters a medium with a different index of refraction. The index of refraction of a medium depends on its density. When part of a light beam encounters a medium of one density and another part of the light beam encounters a medium of a different density, the parts of the light beam bend differently, altering the light's energy distribution pattern. The new energy distribution pattern is called a shadow image. Areas with large changes in density appear as a dark and bright region adjacent to one another. Shadowgraph images are representations of the magnitude of the Laplacian of the density field [26]. The Laplacian is the second derivative with respect to space. Shadowgraph systems are similar to schlieren systems, but shadowgraph systems do not have a knife edge altering the image that reaches the camera. Schlieren images show the density gradients, not the Laplacian. The shadowgraph system used in this study is made from a light source, two mirrors, and a high speed camera. The system is shown schematically in Figure 4.4 and as a photograph in Figure 4.5. The system is from Edmond Optics Inc., part number 71-013.

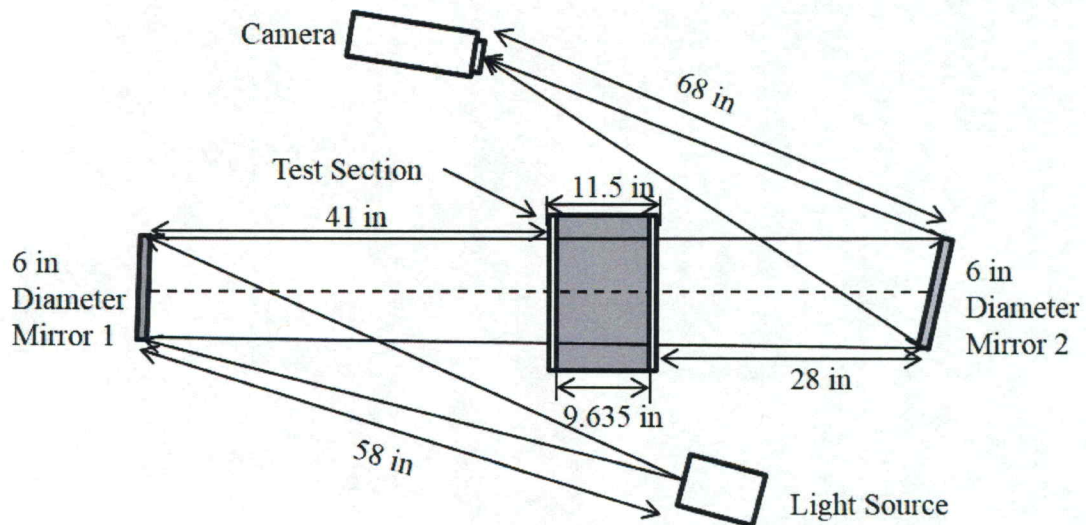


Figure 4.4: A schematic diagram of the flow visualization system



*Figure 4.5: Photograph of the flow visualization system.*

The light source is a SugarCUBE LED Illuminator. It is manufactured by Edmond Optics and is model number 66-032. The SugarCUBE LED Illuminator is strapped to a stand. The strap is a 1 inch HDX ratchet strap. The stand is custom manufactured by Nicole Tool and Die. The stand has a triangular base. A bolt is located at each vertex of the triangular base. The bolts are used to tilt the stand to an appropriate angle. The main support of the stand is in the center of the triangular base. This support has a telescoping extension. The extension has several pin holes at discrete heights. A pin is inserted in the hole that holds the extension at the appropriate height. A threaded extension protrudes from the telescoping extension. This threaded extension allows for a finer adjustment in the height. A square plate is atop the main support and extensions. The SugarCUBE LED Illuminator is placed on the square plate. The custom manufactured stands are visible in Figure 4.5.

The stand holds the base of the SugarCUBE LED Illuminator approximately 31 inches off the ground. This configuration places the light beam at 33.5 inches off the

ground. The SugarCUBE LED Illuminator is set to the lowest light intensity setting. The SugarCUBE LED Illuminator produces a beam of focused white light. The beam of light reflects off of a 6 inch diameter focusing mirror.

The mirror is on a second custom stand manufactured by Nicole Tool and Die. It is the similar to the stand that holds up the SugarCUBE LED Illuminator. These stands also have an attachment to the square plate that allows fine adjustments of the mirrors. The angle and position of the mirror on the stand are adjustable. The stand holds the center of the mirror approximately 41 inches off the ground and 58 inches from the light source. This mirror directs the reflected light through the side walls of the test section.

Since the viewed image is generally invariant in the spanwise direction, the light beam is aligned to be parallel to the spanwise direction and orthogonal to the side walls. This alignment provides the images with the greatest distinction of the flow features. After passing through the test section, the light beam reflects off of a second mirror. This mirror is identical to the mirror previously described. The mirror is on a third stand that is similar to the stands previously described. The light beam travels from the mirror to a Phantom v711 camera.

#### **4.2.2 Phantom v711 Camera**

The Phantom v711 camera is manufactured by the Ametek Materials Analysis Division of Vision Research Company. An AF Micro NIKKOR 200 mm 1:4D ED lens on the camera focuses the image. The lens is manufactured by Nikon. The camera is mounted on a Manfrotto tripod. The tripod's part number is MVH502A, 546BK-1.

The Phantom v711 camera captures a time sequence of digitized flow visualization images. The images are acquired in a grayscale format. The standard



exposure for the camera is 1 microsecond. The camera is capable exposure times as small as of 300 nanoseconds. The Phantom v711 high speed camera can digitize images at sampling frequencies up to 1400 kHz. The camera has a limited acquisition speed of 7 gigapixels per second. In order to maintain this limit, the resolution decreases as the sampling frequency increases. The maximum image size is 1280 x 800 pixels. These largest images can be acquired at sampling frequencies less than 7530 frames per second. The image size decreases incrementally until it reaches 128 x 8 pixels. For standard settings, these images have sampling frequencies greater than 675,800 frames per second. Table 4.1 shows the size and speed specifications of the Phantom v711 camera. The pixel size remains constant at 0.7874 milli-inches (20 micrometers), so the physical size of the images decreases as the resolution decreases. The present study uses images sizes of 1280 x 800 pixels with sampling rates of 100 Hz, 400 Hz, 500 Hz, 1000 Hz, 2500 Hz, and 5000 Hz, as well as an image size of 1024 x 512 pixels with a sampling rate of 10000 Hz, depending on the specific test.

The camera has a limited amount of internal memory. During a test, the data is stored on the camera. This limited memory determines the number of frames that can be saved per test. The number of frames that can be saved changes based on the image size. The total duration of time between the first image and last image in the time sequence is the number of frames divided by the sampling frequency. The shortest duration is 2.97 seconds which occurs for conditions where the maximum speed for a given image size is used.

*Table 4.1: The fastest sampling rate for each standard image resolution size for the Phantom v711 camera [27].*

Resolution	Highest FPS
1280 x 800	7530
1280 x 800 (720p)	8360
1024 x 768	9520
896 x 480 (DVD)	17000
768 x 576 (PAL)	16100
768 x 480 (NTSC)	19300
640 x 480	22400
512 x 512	25000
512 x 256	49500
512 x 128	97500
384 x 256	60900
256 x 256	79000
256 x 128	153200
256 x 64	288800
128 x 128	215600
128 x 64	397100
128 x 32	685800
128 x 16	1077500*
128 x 8	1400000*
*FAST Option	

#### **4.2.3 Visualization Data Acquisition Software**

A Dell desktop computer running Windows 7 is connected to the camera with an Ethernet connection. This connection is used for control and data communications. The computer uses Phantom Camera Control Application 2.7 software. Through this software, the sampling frequency, image size, exposure time, and image brightness are set. After data are acquired, the Phantom Camera Control Application 2.7 software saves the time sequence of images as a video Cine file on the computer. The camera software also saves each image as an eight-bit bitmap image file.

## CHAPTER 5. ANALYTICAL PROCEDURE

### 5.1 Flow Characterization

The Mach number at the entrance to the test section is measured to be 1.54 to 1.56 using measured values of static and stagnation pressure. Test section inlet Mach number is also experimentally determined using the Rayleigh formula [29]. Using measured quantities, the velocity is calculated using the equation given by

$$u_{\infty} = M \cdot \sqrt{\gamma R \cdot \left(\frac{T}{T_t}\right) \cdot T_t} \quad (5.1)$$

As such, the velocity at the entrance to the test section is 1411 feet per second. The outdoor ambient air temperature is considered the stagnation temperature upstream of the shock wave. This value and arrangement of Eq. (5.1) are used because the outdoor ambient temperature is the only temperature data collected. The ratio of temperature to stagnation temperature is calculated based on isentropic flow relationships. The ratio of specific heats and the gas constant are associated with atmospheric air. Air within the wind tunnel is assumed to be an ideal gas. The mass flow rate at the test section inlet is determined using

$$\dot{m} = \frac{P}{\sqrt{R \cdot T}} \cdot \sqrt{\gamma} \cdot A \cdot M \quad (5.2)$$

The boundary layer thickness at the entrance to the test section is estimated to be 0.354 inches.

## **5.2 Frequency Analysis of Flow Visualization Data**

The time sequence of flow visualization images are processed to compute frequency spectra using National Instruments' LabVIEW software and Mathworks' MATLAB software in six steps: extract data from a pixel location, filter the data, transform and normalize the data into the frequency domain, smooth the frequency domain results, remove the white noise, and ensemble average the data of several pixel locations.

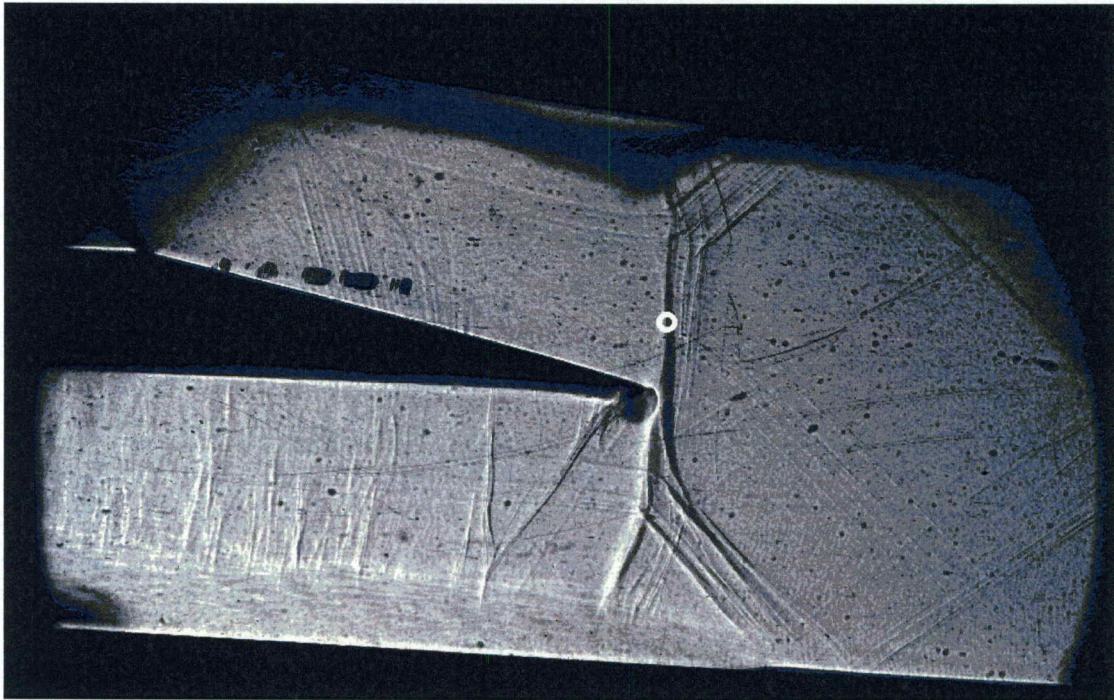
### **5.2.1 Extract Pixel Data**

For a selected collection of images, a MATLAB program extracts the time sequence of grayscale values at any specified pixel location. This code is used in MATLAB versions R2014b through R2018a.

During a wind tunnel test, flow conditions are established and maintained for a time interval. Only this portion of the wind tunnel test is considered during the analysis. The images captured during start-up and shut-down, prior and after flow is established, are removed because the results contain anomalous frequency content. The user must decide which of the eight-bit bitmap images correspond to the times with established flow conditions. This is done based upon the position of the shock wave within the flow visualization images. The criteria for determining when established flow conditions begin is when the shock wave begins to move upstream for the first time. The image in the time sequence immediately before this happens is selected to be the first one with established flow conditions. This is generally after the shock wave fully enters the frame. The last image during the time interval with established flow conditions is the last one in the time sequence before the shock wave moves upstream for the last time. As data processing

progresses, digital versions of these images are saved in a folder that only contains associated images.

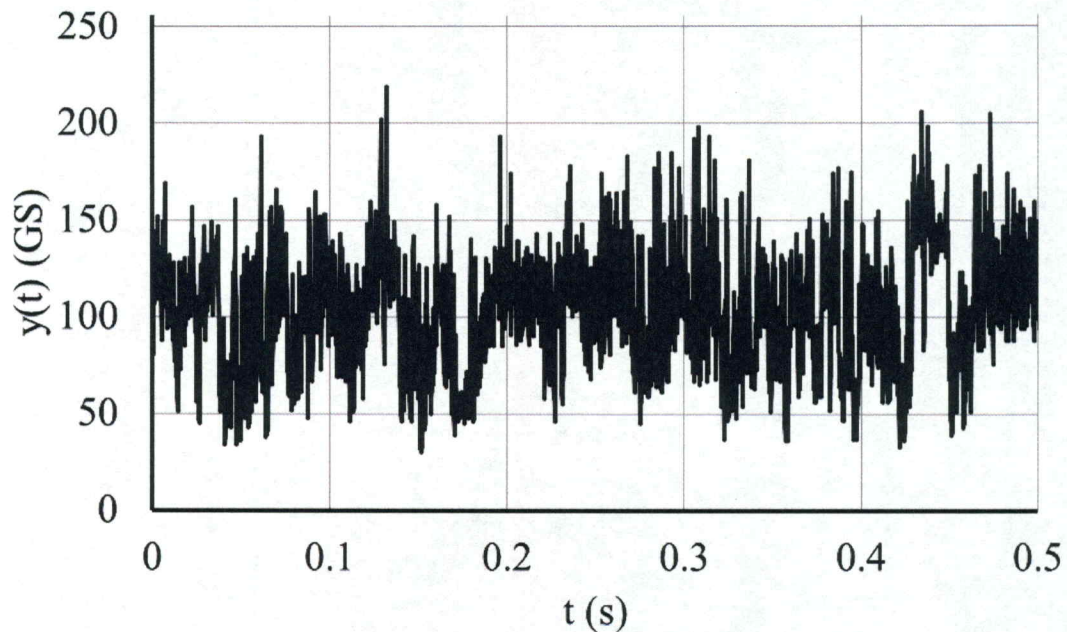
The MATLAB code used to extract grayscale value data from specific pixel locations in the images has three necessary inputs. The user indicates which pixel location to analyze, the file path to the folder of bitmap images during established flow conditions, and the output file name. Figure 5.1 shows an example of a pixel location in the shadowgraph image that is analyzed.



*Figure 5.1: A pixel location at [736, 329] on the shock wave is circled in a shadowgraph image from the test on 13 November 2017.*

MATLAB's "imread" function determines the grayscale value of the specified pixel location for each image in the folder. The output is a time sequenced array of grayscale values. MATLAB's "xlswrite" function saves the associated array in a Microsoft Excel spreadsheet. To make this compatible with LabVIEW 2011, the Excel spreadsheet is saved as a tab delimited text file with the extension ".lvm." A segment of

the grayscale data with respect to time at the pixel location in Figure 5.1 is shown in Figure 5.2.



*Figure 5.2: Grayscale value of a pixel location [736, 329] with respect to time for a half second of data from the test on 13 November 2017.*

## 5.2.2 Filter

A low-pass filter is applied to the time sequence of grayscale values. LabVIEW software is used to filter this data.

### 5.2.2.1 Read Grayscale Data in LabVIEW for Filtering

The time sequence of grayscale values must be read into LabVIEW software in order to be filtered. LabVIEW 2011 Full Development System with Service Pack 1 is used.

LabVIEW has three types of subroutines: Express Virtual Instruments (VI), sub VIs, and functions. An Express VI is standard code made by National Instruments

that is readily available in LabVIEW. Express VIs differ from standard sub VIs because Express VIs use dialog boxes to configure the inputs and outputs; note that inputs and outputs must be coded for sub VIs. Express VIs and sub VIs make up sequences of multiple functions and other sub VIs. Functions are the most basic components that are available to the user in LabVIEW. The inputs and outputs of Express VIs are in the form of the dynamic data datatype. Dynamic data is versatile in that it can be easily converted to other forms of data—such as waveforms, arrays, and scalars.

The file path to the saved text file is specified within a subroutine in LabVIEW called the “Read from Measurements File” Express VI. The subroutine imports the time sequence of grayscale values into LabVIEW from the tab delimited text file. Once in LabVIEW, the data is converted from the dynamic data datatype to an array of double precision floating point values.

#### **5.2.2.2 Filter the Time Sequence**

A low-pass Butterworth filter is used to filter the time sequence data. A Butterworth filter is used, as opposed to another type of filter, because of its relatively uniform transfer function scaling over the frequencies of interest [28]. The transfer function is the ratio of the filtered value to the unfiltered value as a function of frequency. Uniform scaling over the transfer function is important because it does not add extraneous frequency content to the data. This ensures that any peaks in the frequency domain data are from real events, not distortion from the filter.

Figure 5.3 shows the magnitude of the transfer function with respect to frequency ratio for the first through fifth order Butterworth filters. The first through fifth order filters are labeled as A through E, respectively, in the figure. The frequency ratio on the

abscissa is the frequency divided by the cut-off frequency. The figure shows how the transfer function is generally uniform but drops rapidly as the frequency approaches the cut-off frequency. The cut-off frequency is defined as the frequency where the filtered frequency content is 3 dB lower than the unfiltered frequency content. The drop-off of the transfer function's magnitude near the cut-off frequency is more abrupt for higher order filters than lower order filters. The fifth order filter is used in this analysis because of the abrupt decrease in magnitude of the transfer function near the cut-off frequency.

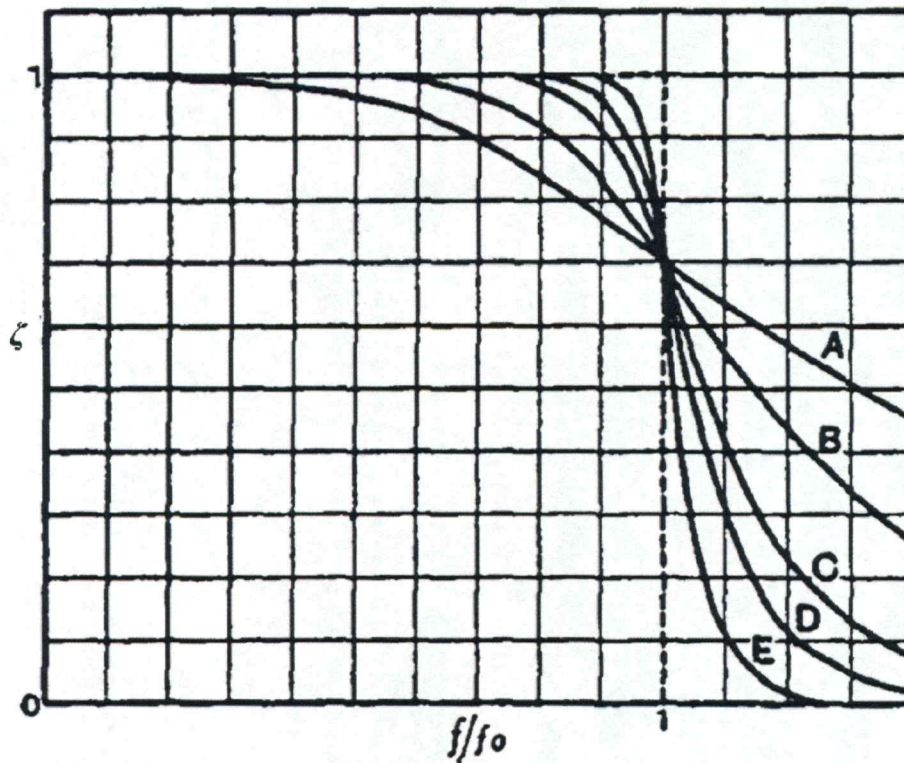


Figure 5.3. The transform function of a Low Pass Butterworth Filter. Lines A through E represent orders 1 through 5. This image is from [27].

The time sequence array of grayscale values is filtered with a fifth-order, low-pass Butterworth filter, using a cut-off frequency of 1 Hz less than the Nyquist folding frequency. The filtering is done with LabVIEW's "Butterworth Filter" VI subroutine.



The data, the cut-off frequency, the sampling rate, the type of filter (low pass, for example), and the order of the filter are inputs to this subroutine. This output is the filtered data as an array of double precision floating point values.

After being filtered, the data is converted back to the dynamic data datatype. The filtered data in the dynamic data datatype is specified within the LabVIEW subroutine called “Write to Measurements File” Express VI. The file path that indicates where on the computer to save the data is also input into that subroutine. The subroutine saves the filtered data to a tab delimited spreadsheet.

### **5.2.3 Transform to the Frequency Domain**

The transformation from the time domain to the frequency domain is accomplished using MATLAB software. This transformation gives the square root of the power spectral density of grayscale values as it varies with frequency, also referred to as the grayscale spectral energy distribution. MATLAB versions R2013a through R2018a are used. The filtered data is read into MATLAB from the spreadsheet using the “xlsread” function. This function’s inputs are the file path and the range of cells in the spreadsheet that contain the data. The function’s output is an array of the filtered data. The array of the filtered time sequence data undergoes a single sided discrete fast Fourier transform. This transform is done using the Fast Fourier Transform —“fft”— function in MATLAB software. The filtered time sequenced array of grayscale values is input into the Fast Fourier Transform function. The function gives the double sided frequency transform of that time sequenced array. Next, the second half of the frequency transform array is discarded. The resulting array is the single sided frequency transform.

This transform is normalized such that it becomes the square root of the power spectra of the time domain function. With the exception of the first term in the frequency spectra array, this relationship is described by the equation given by

$$Y(f) = \frac{2}{N} \cdot |\mathcal{F}(y(t))| \quad (5.3)$$

Equation (5.3) indicates that the magnitude of each term in the single sided frequency transform is multiplied by 2 and divided by the number of indices in the time sequence array. The first term in this transform represents the time averaged grayscale value and corresponds to a frequency of zero. The value of this term is set equal to half of the value attained by using Eq. (5.3). Each term in the frequency transform corresponds to a unique frequency. The frequencies steadily increase from zero to the Nyquist folding frequency. The frequency resolution is the difference in frequency between any two consecutive terms in the frequency transform.

The frequency resolution is determined using

$$\Delta f = \frac{Fs}{N} \quad (5.4)$$

The frequency resolution is defined as the number of points in the time sequence array divided by the sampling frequency. The frequency resolution is therefore a function of the sampling frequency and the amount of time that useful data are collected.

The transformation preserves spectral energy content such that the variance of the time domain function is equal to half of the sum of the squares of the frequency domain function, excluding the steady state term. This relationship is described using the equation given by

$$\frac{1}{2} \cdot \overline{Y(f)^2} = \overline{y(t)^2} \quad (5.5)$$

The variance formula used on the time domain data to attain the energy is expressed using

$$\overline{y(t)^2} = \frac{\sum_{k=1}^N (y(t)_k - \frac{\sum_{j=1}^N y(t)_j}{N})^2}{N} = \overline{(y(t)_k - \overline{y(t)_k})^2} \quad (5.6)$$

The first step in determining the variance is to calculate the average of the grayscale values in the time sequence. Next, the difference between each of the grayscale values in the time sequence and that average value is computed. Each of these differences is then squared. Finally, all of those squared differences are averaged together. That average gives a single value that is the variance of the time sequence. It is also equal to the total spectral energy.

The energy from the frequency domain is evaluated as

$$\frac{1}{2} \cdot \overline{Y(f)^2} = \frac{1}{2} * \sum_{k=2}^{\frac{N}{2}-1} Y(f)_k^2 \quad (5.7)$$

Equation (5.7) states that the total spectral energy is equal to half of the sum of the squared grayscale values in the single sided frequency spectra. The summation does not include the value of the first term where the frequency is zero.

These results may be expressed with respect to frequency or to the Strouhal Number. The Strouhal Number is defined as

$$St_r \equiv \frac{2\pi \cdot f \cdot \delta_o}{u_\infty} \quad (5.8)$$

The Strouhal Number is the frequency scaled by the boundary layer thickness and the incoming velocity at the entrance to the test section. Similar to frequency, the Strouhal number has a resolution. The resolution of the Strouhal Number is determined using an equation given by

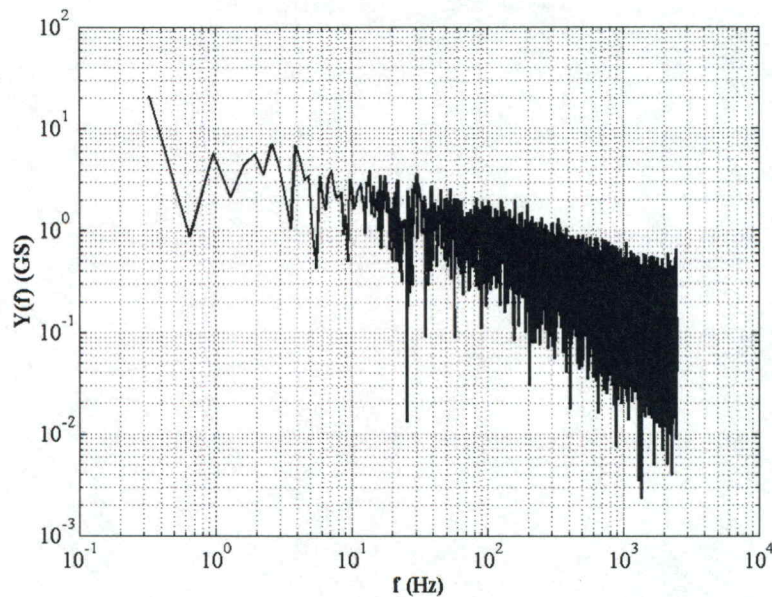
$$\Delta St_r = \frac{2\pi \cdot \Delta f \cdot \delta_o}{u_\infty} \quad (5.9)$$

The resolution of the Strouhal number is the dimensionless form of the frequency resolution.

#### 5.2.4 Smooth the Frequency Transform

The transformed arrays have large variations of grayscale spectral energy distribution values, given as  $Y(f)$ , over small ranges of frequency. As mentioned,

$1/2 \cdot \overline{Y(f)^2}$  is the spectral energy content. The variation of the grayscale spectral energy distribution increases as frequency increases. Figure 5.4 shows a typical example of the frequency transform with respect to frequency. The data in Figure 5.4 are obtained using Eq. (5.3). With such a result, it is difficult to determine detailed frequency content. Smoothing is therefore necessary.



*Figure 5.4: The grayscale spectral energy distribution before smoothing. This is for the data associated with pixel location identified in Figure 5.1. It is representative of all unsmoothed grayscale spectral energy distribution data.*

Smoothing is imposed using a simple running average which is applied to the normalized transform array data, such as are shown in Figure 5.4. For a simple running average, each data point in an array is replaced by the average of the data within a specified interval centered on that data point. Table 5.1 summarizes the smoothing process used in the analysis.

*Table 5.1: Summary of the smoothing process. This scheme is used for all sampling frequencies.*

<b>Frequency range (Hertz)</b>	<b>Averaging and Applied Data Range</b>
$0 < f \leq 20 \cdot \Delta f$	None
$21 \cdot \Delta f < f \leq 20$	Running Average $\pm 1$ point
$20 < f < 0.95 \cdot F_s/2$	Running Average $\pm 0.05 \cdot f/\Delta f$ points
$0.95 \cdot F_s/2 < f < F_s/2$	Replace all values with a single value determined by the average over all frequencies in this range

With this approach, the first 20 points in each array, corresponding to the points at the 20 lowest frequencies, are not averaged; they retain their initial values. For data between the 21<sup>st</sup> point and the data point corresponding to 20 Hz, each data point is replaced by the value which is equal to the average of 3 data points comprised of the considered data point and the adjacent point on each side of the data point considered. A similar scheme is done for data corresponding to frequencies greater than 20 Hz, but the number of points per side employed to determine the smoothed value is given by

$$0.05 \cdot \frac{f}{\Delta f}$$

This expression is equal to 5 percent of the array index of the data point considered. The array index is the frequency at the considered point divided by the frequency resolution. This expression is a function of the data point's frequency. Note that the expression

$0.05 \cdot f / \Delta f$  is inapplicable for very high frequency data because there are not  $0.05 \cdot f / \Delta f$  points at higher frequencies remaining in the array. The expression becomes invalid for frequencies that are greater than approximately 95 percent of the Nyquist folding frequency which equals  $F_s/2$ . This limit is given by the expression

$$f \leq 0.95 \cdot \frac{F_s}{2}$$

As a result, averaging is not applied to the data points at frequencies greater than this limit. For the data corresponding to frequencies greater than approximately 95 percent of the Nyquist folding frequency, each value is replaced by a single value that is determined by averaging of all the non-smoothed high frequency data. This is the average of the frequency content over the high frequency range for a specific pixel location during a specific test. Each of the points in this range is subsequently given that value. The data smoothing procedure is typically implemented one time for each spectral data set.

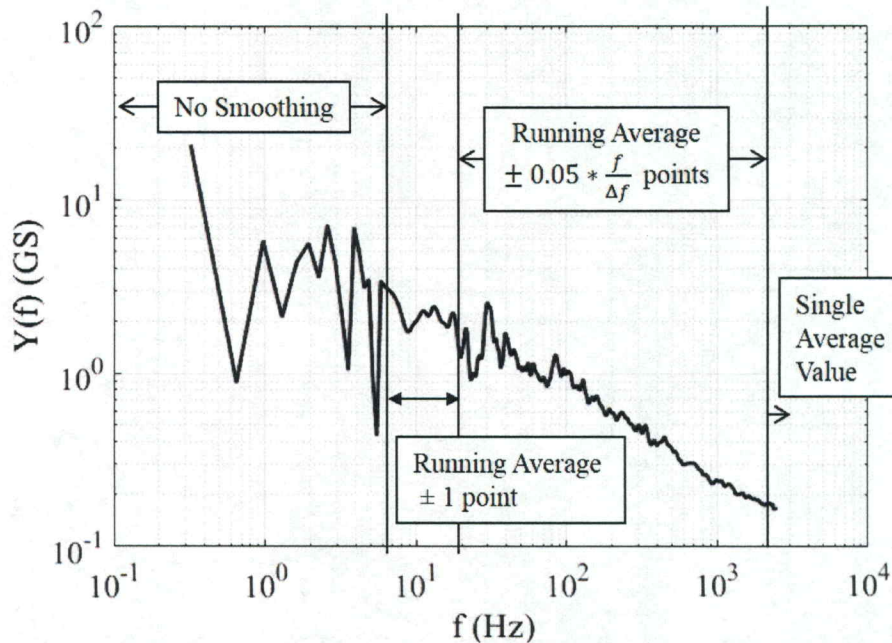


Figure 5.5: The grayscale spectral energy distribution after smoothing. This is from the data in Figure 5.4.

Figure 5.5 is representative of the smoothed data. It shows the same frequency data as Figure 5.4, but after the smoothing process is complete. Note that the spectral peaks are much more evident than in Figure 5.4.

### **5.2.5 Remove White Noise**

The white noise is associated with the background electronic noise within the time series signal. The next step in the analysis is to subtract the white noise from the frequency domain data. The average value that replaces the grayscale spectral energy distribution data corresponding to frequencies greater than 95 percent of the Nyquist folding frequency during the smoothing process is considered the white noise energy content level. The same value of the white noise energy content level is subtracted from every spectral data point at each frequency within the smoothed frequency array. Note that each image pixel location is associated with a unique frequency transform and therefore a unique white noise energy content level. Removing the white noise gives greater definition of the spectral variations on a log-log plot, especially at higher frequencies. Figure 5.6 shows a typical example of the smoothed data before and after the white noise is removed.

The white noise is not removed in all data sets. However, all spectral comparisons (presented later in the thesis) are consistent as to whether the white noise is removed or included. For example, the white noise is removed from the data from the test on 13 November 2017 which is described in Chapter 7. White noise is not removed from the comparisons of the effects of test section modifications which are described in Chapter 6.

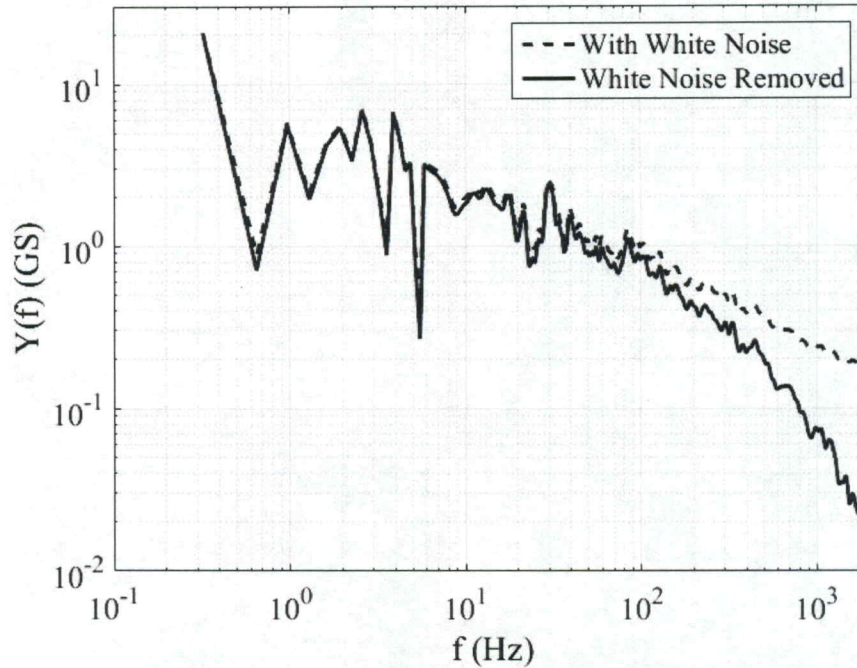


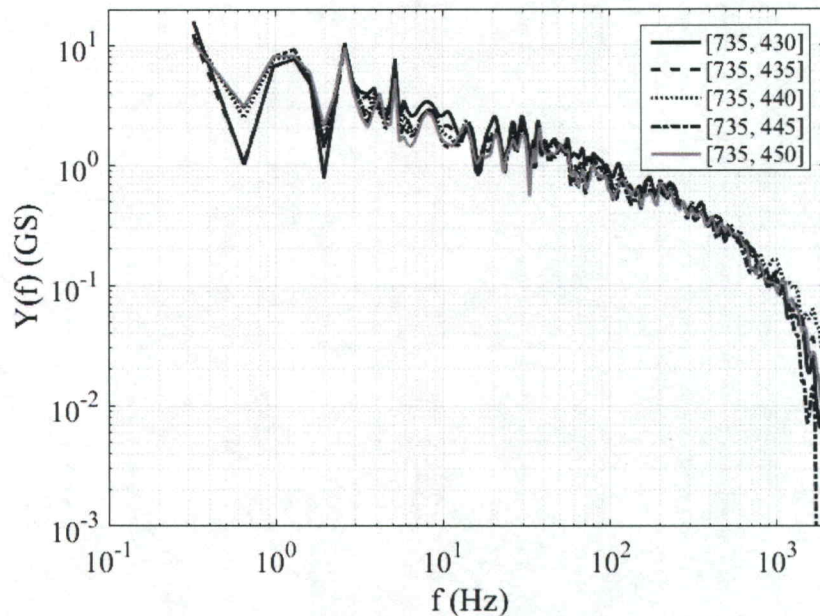
Figure 5.6: The grayscale spectral energy distribution with and without removing the white noise. The data is from the pixel [736, 329] from the test on 13 November 2017. It is representative of all data before and after removing the white noise.

### 5.2.6 Ensemble Average the Frequency Data

Grayscale spectral energy distribution results are also ensemble-averaged. Five pixel locations within the same flow structure are selected for this purpose at specific positions below the shock wave holding plate at the stream-wise-averaged shock wave position, which is determined using the scheme discussed in Section 5.3. The pixel locations selected on the downstream lambda foot are located at specific positions above the bottom wall. Because the resolution of each pixel is the same, regardless of image size, pixel locations correspond to the same physical distance relative to test section features, such as the bottom wall and shock wave holding plate.

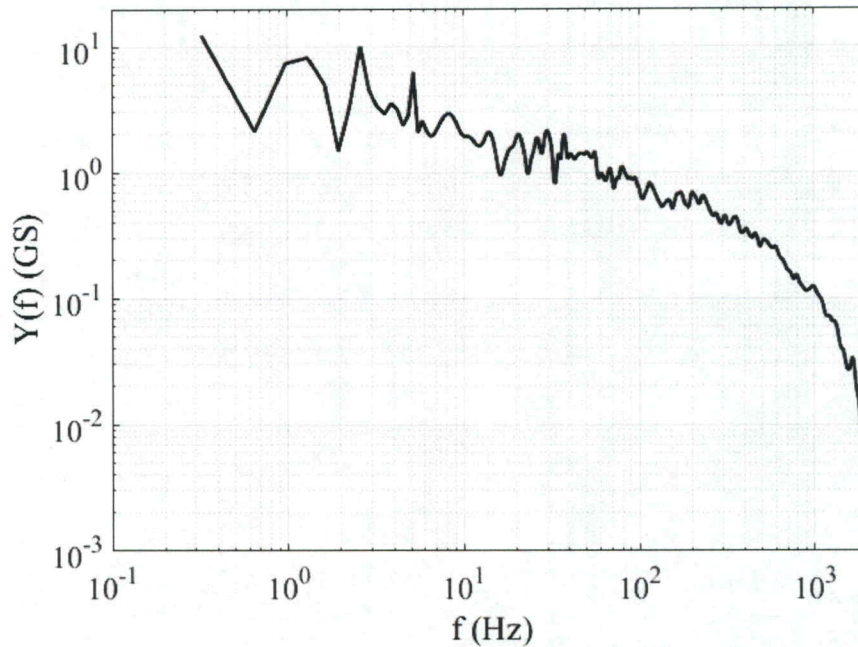


Grayscale spectral energy distribution data associated with the five pixel locations on the shock wave (from the test on 13 November 2017) are shown with respect to frequency in Figure 5.7.



*Figure 5.7: The five grayscale spectral energy distribution with respect to frequency plots for the five pixels analyzed near the shock wave. Data is from the test on 13 November 2017.*

Grayscale spectral energy distribution data for the five pixel locations are averaged together at each distinct frequency. The ensemble-averaged grayscale spectral energy distribution with respect to frequency for this data is shown in Figure 5.8.



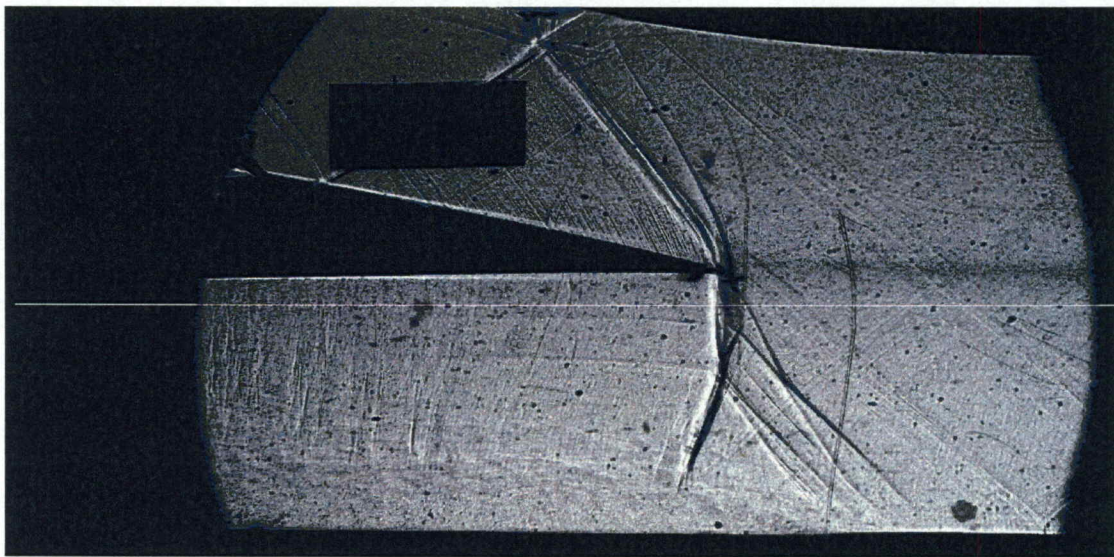
*Figure 5.8: Ensemble averaged grayscale spectral energy distribution with respect to frequency for pixels near the shock wave from the test on 13 November 2017. This is the average of the grayscale spectral energy distribution data shown in Fig. 5.7*

Note that the grayscale spectral energy distribution results described in Chapters 6 and 8 employ this ensemble averaging scheme. Results presented in Chapter 7 are not ensemble-averaged.

### 5.3 Shock Wave Position Tracking

The MATLAB R2013a code is used to track the position of a shock wave in a time sequence of shadowgraph images. Shock waves generally appear as a dark line next to a bright line within shadowgraph images, as is described in Chapter 4.2. Typically, the dark portion has the most contrast relative to the background. Hence, streamwise shock wave positions are represented by locations of the darkest pixels in a particular portion of the shadowgraph visualization images.

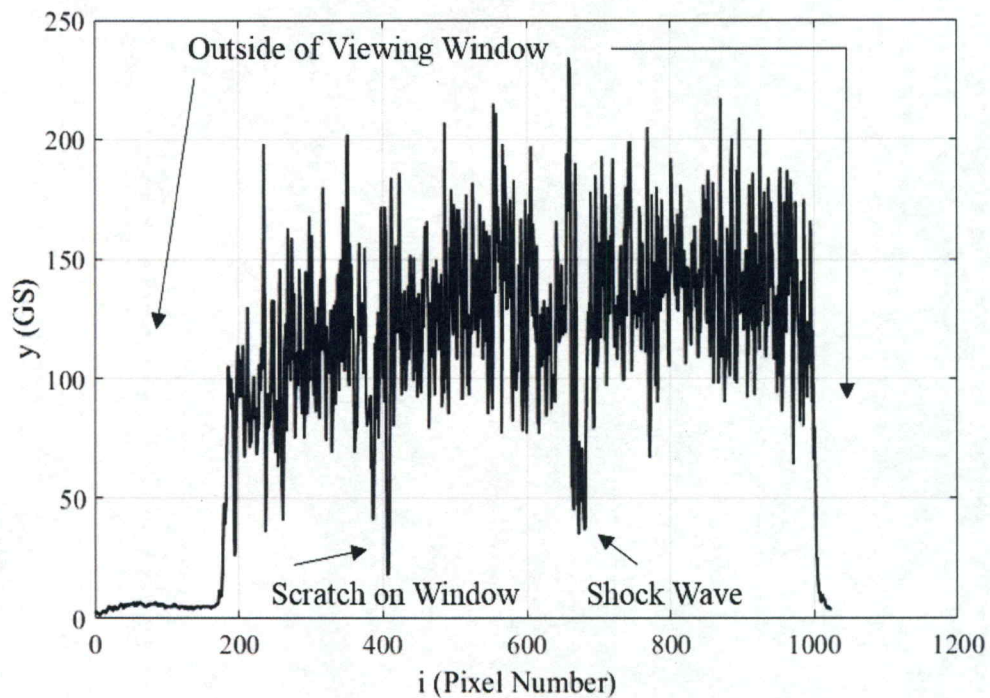
In order to track the shock wave position, the user first specifies the file path containing the time sequence of shadowgraph images. The file path and name of the first image in the time sequence is passed into the “imshow” function in MATLAB. This function displays the image in a MATLAB figure. The user must double click a location near the shock wave or lambda foot in the figure. The Get Points function, “getpts,” determines the pixel coordinates at the location clicked by the user. Only the vertical coordinate is used. It is paired with all horizontal,  $i$ , coordinates, creating a horizontal line of pixels. Figure 5.9 shows a white horizontal line at the selected vertical pixel coordinate from data obtained on 05 April 2018.



*Figure 5.9: The white line indicates the locations of all the pixels where the grayscale data is analyzed. This is from the test on 05 April 2018. The vertical coordinate is 277.*

The coordinates of each pixel location along this line are input into the “imread” function. This “imread” function obtains the grayscale pixel value at every pixel location along this line. The program determines the grayscale pixel value along the same horizontal line for each image in the time sequence array. An example of the grayscale pixel values with respect to horizontal pixel coordinate,  $i$ , at any instant of time from the

time sequence, is shown in Figure 5.10 for one image. This figure shows the grayscale pixel values for the last image in the time sequence associated with the 05 April 2018 test.



*Figure 5.10: Grayscale of the last frame in the time sequence with respect to  $x$  pixel location. This is for the horizontal line of pixels all with  $z = 277$  for the test on 05 April 2018.*

The user must specify a region of streamwise,  $i$ , pixel coordinates where the shock wave is expected to appear. Doing this minimizes the possibility that the shock wave finding algorithm mistakes an image effect (not related to flow structure) for the shock wave. As an example, scratches on the side wall of the wind tunnel appear as dark spots within the shadowgraph images. A scratch is identified in Figure 5.10, as are the edges of the viewing window. Microsoft Paint is used to determine the pixel location range in which the shock wave is expected. The Minimum function, “min,” in MATLAB

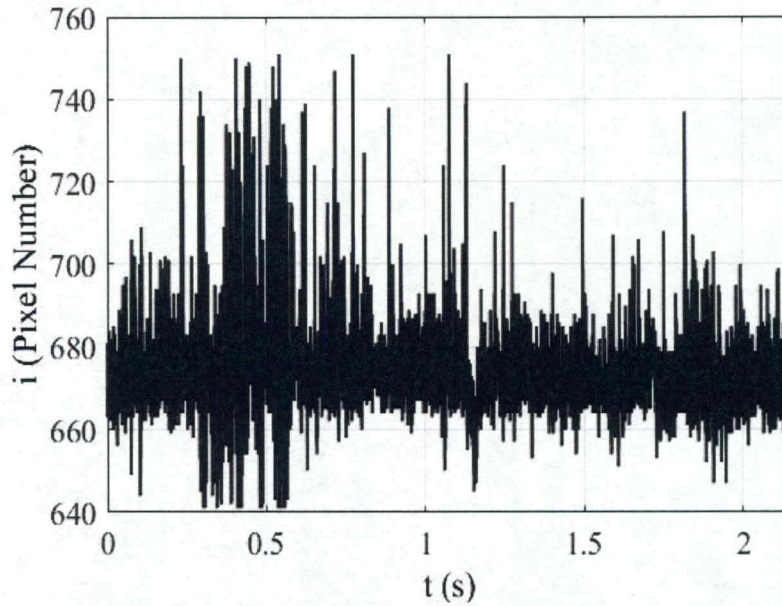
then determines the pixel location with the lowest grayscale value within the specified region which is present along the horizontal line. This is done for each image within the time sequence. This pixel is the darkest pixel. As such, it represents the location of the shock wave. The horizontal pixel number,  $i$ , is saved to an array. The darkest pixel in the range between  $i = 500$  and  $800$  is identified as the shock wave in Figure 5.10.

The average pixel number representing the average shock wave position is determined. This average value is subtracted from each value in the time sequence so that a value of 0 corresponds to the average shock wave location. Negative values indicate the shock wave is downstream of its average position. Positive values indicate the shock wave is upstream of its average position.

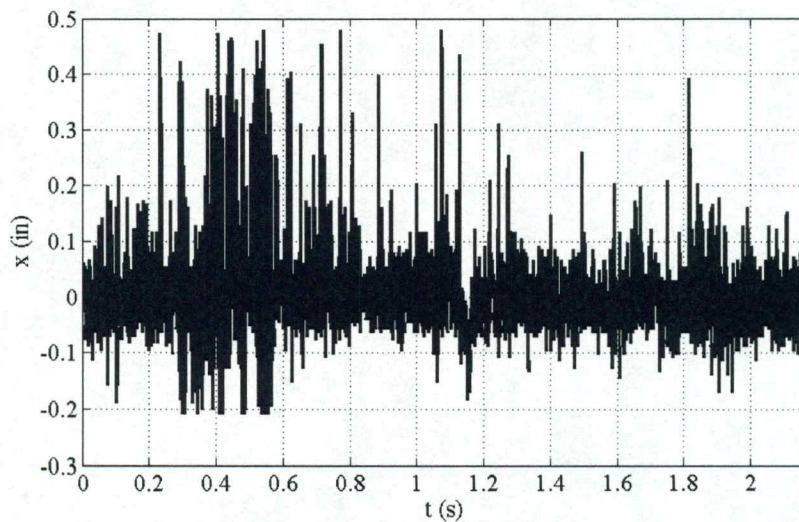
The physical location corresponding to the pixel location is then determined. A scaling factor is used to convert the pixel coordinate of the shock wave into a physical distance in inches. The scaling factor is determined by dividing the physical length of a piece of tape, located on the test section window, by the number of pixels along its length in the shadowgraph image. The number of pixels is found using Microsoft Paint. The length is measured using Mitutoyo 500-196-30 Absolute Solar digital calipers.

The streamwise shock wave position, relative to its average position, is determined as it varies with time. Time is the index of the time sequence array associated with each shock wave position divided by the sampling frequency. Figures 5.11 and 5.12 show an example of the streamwise shock wave position with respect to time. Figure 5.11 shows the position represented as number of pixels. Figure 5.12 shows the position represented in inches from the shock wave average location. Figure 5.13 shows a subset of the data in Figure 5.12 that better illustrates the motion of the shock wave. The time

domain shock wave position data is filtered, transformed into the frequency domain, and smoothed, per Sections 5.2.2 through 5.2.5. Figure 5.14 shows the associated spectral energy with respect to frequency.



*Figure 5.11: 2018-04-05 Shock location as a function of time. This is for vertical pixel location 277.*



*Figure 5.12: 2018-04-05 Shock location (with respect to the time averaged shock position) as a function of time. This is for vertical pixel location 277.*

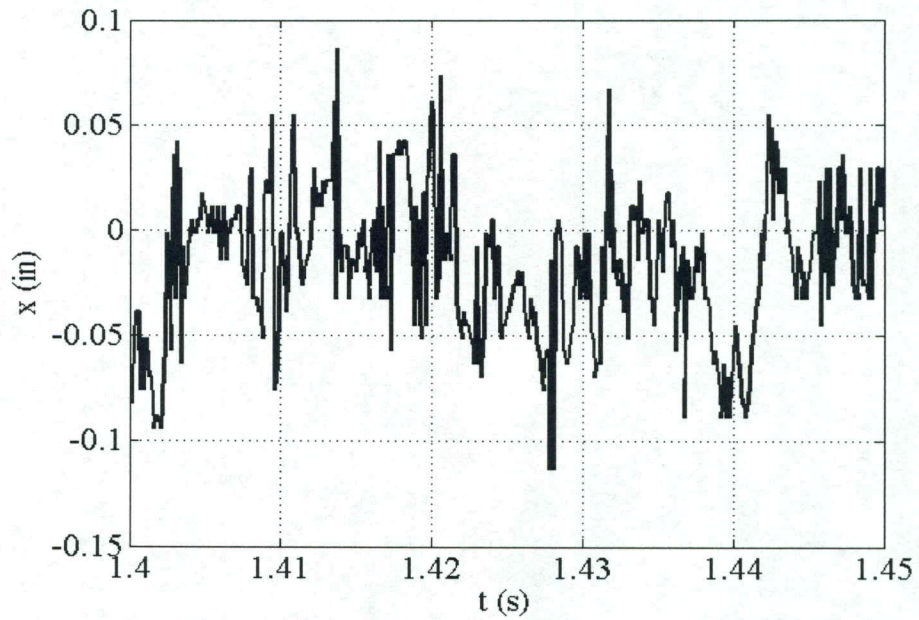


Figure 5.13: A subset of the data from Figure 5.12. This shows shock wave position from 1.40 to 1.45 seconds.

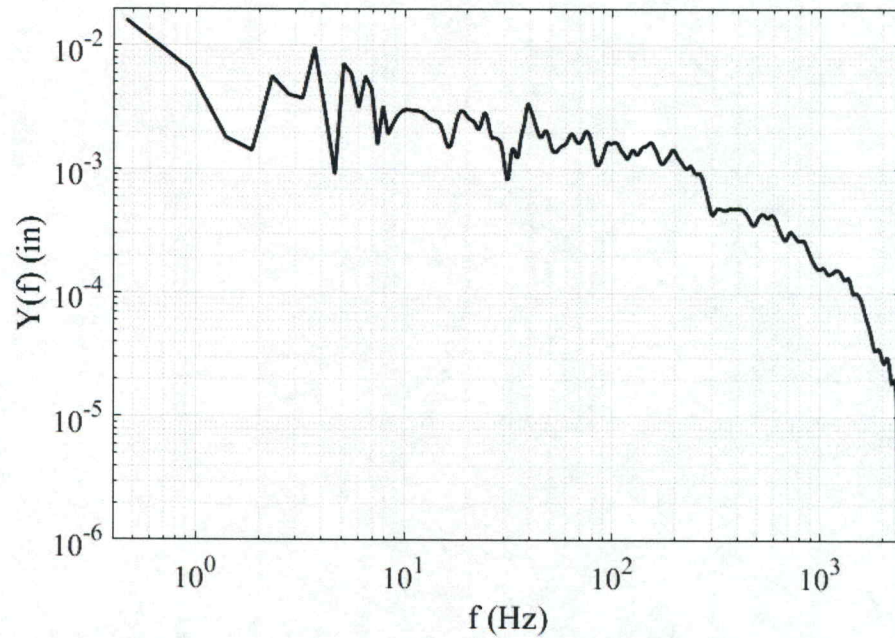


Figure 5.14: Spectral energy distribution associated with the shock wave position relative to the average shock wave position as a function of frequency.

## 5.4 Correlations

The MATLAB code is used in versions R2013a and R2018a to determine different spatial and time correlations as they vary with location, frequency, and phase lag magnitude. Filtered grayscale value time-varying data, as described in Section 5.2.2, are used as inputs for correlation determination.

### 5.4.1 Single Point Auto-Correlation

An auto-correlation of grayscale data from a single pixel location is computed as it varies with time. The auto-correlation function is defined by

$$ACF_k = \frac{c_k}{c_o} \quad (5.10)$$

This gives the normalized correlation between the grayscale value time sequence data and the same data sequence at a time lag of  $k$ . The correlation is expressed by the equation

$$c_k = \frac{1}{N} \sum_{n=1}^{N-k} (y_n - \bar{y})(y_{n+k} - \bar{y}) \quad (5.11)$$

The magnitude of  $ACF_k$  given by Eq. (5.10) is normalized by the variance of the time sequence, which is determined using the equation given by

$$c_o = \frac{1}{N} \sum_{n=1}^N (y_n - \bar{y})^2 \quad (5.12)$$

Large positive values of the  $ACF_k$  auto-correlation function indicate that the data are similar at both instances of time. Negative values outside of a confidence interval indicate that the data are strongly different, with less positive correlation. The confidence interval employed is 95 percent, as applied to the correlation to show the time lags at which the auto-correlation is significant.



MATLAB 2013a code is used to determine the auto-correlation of the grayscale time sequence data associated with a pixel located on the shock wave. The time sequence data is an input into the “autocorr” function. The number of lags to compute is the second input into the “autocorr” function. For this input, a number one less than the number of data points in the time sequence is used. Therefore, the auto-correlation is calculated over a range of possible time lag values. The auto-correlation, the lag, and the confidence interval bounds are outputs to the “autocorr” function. The “autocorr” function assumes a sampling frequency of 1 Hz for determination of time lag values, which is not correct for the collected data. The time lag that is output by the “autocorr” function is then divided by the sampling frequency to determine actual time lag in seconds.

#### 5.4.2 Magnitude Squared Coherence

Data associated with two separate pixel locations, each from a different region, are inputs to a magnitude squared coherence calculation. The magnitude squared coherence is the ratio of the cross power spectral density,  $P_{y_1y_2}$ , to the product of the power spectral densities of the two functions,  $P_{y_1y_1}$  and  $P_{y_2y_2}$ , expressed as

$$C_{y_1y_2} = \frac{|P_{y_1y_2}|^2}{P_{y_1y_1} * P_{y_2y_2}} \quad (5.13)$$

The power spectral density is represented by the equation

$$P_{y_1y_1} = Y(f)^2 \quad (5.14)$$

The cross power spectral density is then given by

$$P_{y_1y_2} = \sum_{m=-\infty}^{\infty} E\{(y_1)_{n+m}(y_2)_n\} \cdot e^{-j2\pi f \cdot m} \quad (5.15)$$

Equation 5.15 represents the Fourier transform of the cross correlation of the time sequences of grayscale data associated with two different pixel locations, designated  $y_1$

and  $y_2$ . Larger values of magnitude squared coherence indicate greater coherence between the grayscale data associated with the two pixels. Magnitude squared coherence, power spectral density, and cross power spectral density all vary with frequency. This is because unsteadiness is more prominent at certain frequencies than at others, and prominent frequencies change with spatial position within the flow field.

The magnitude squared coherence is determined using the “mscohere” subroutine in MATLAB. Filtered time sequence data from two separate pixel locations are inputs to the subroutine. The sampling frequency is also an input to the “mscohere” subroutine. This subroutine uses Welch’s Overlapped Segment Averaging procedure. Use of this procedure requires input information related to window type, window size, and size of overlapped region. The averaging scheme employs Hanning windowing. The window size is equivalent to one quarter of the length of the filtered time sequence array of grayscale data. This is the same as a quarter of the number of shadowgraph flow visualization images acquired and analyzed. For example, there are 21620 images captured during the test on 05 April 2018, so each window consists of 5405 data points (21620 divided by 4). The default size of the overlapped region is also required. This default size is half of the size of the window length, rounded down. Hence, the windows overlap by 2702 data points.

Magnitude squared coherence for five pairs of pixel locations within the same regions are ensemble-averaged. For example, data from five pixel locations in the upstream boundary layer are correlated, respectively, with data from five pixels locations on the shock wave. Those five coherence results are ensemble-averaged. Next, the resulting ensemble-averaged data are smoothed, as described in Section 5.2.4; however,

smoothing begins at the sixth data point, not the twentieth. Table 5.2 summarizes this procedure.

*Table 5.2. The smoothing process for the magnitude squared coherence results*

<b>Frequency range (Hertz)</b>	<b>Averaging and Applied Data Range</b>
$0 < f \leq 6 * \Delta f$	None
$7 * \Delta f < f \leq 20$	Running Average $\pm 1$ points
$20 < f < 0.95 * F_s/2$	Running Average $\pm 0.05 * f / \Delta f$ points
$0.95 * F_s/2 < f < F_s/2$	Replace all values with a single value determined by the average over all frequencies in this range

#### **5.4.3 Cross Power Spectral Density, Phase Lag and Time Lag**

The cross power spectral density, which is given by Eq. (5.15), is used to calculate the phase lag and the time lag between time sequences of grayscale data associated with two different pixel locations. The time lag is a function of frequency. Perturbations occur at a location and propagate to other locations. Time is required for flow perturbations to travel, so the signals detected at two locations are similar, but differ by some time lag. All the perturbations do not originate in the same location, nor do they propagate along the same path at the same rate. Hence, the perturbations at unique frequencies have unique time and phase lags when considered at the same two pixel locations.

Time sequences of grayscale values associated with individual pixel locations in different regions are inputs to the cross power spectral density, “cpsd,” function in MATLAB. For example, one way used for such correlation determination is the variable containing the data associated with the boundary layers is entered as the first parameter, and the variable containing the data associated with the shock wave or lambda foot is

entered as the second parameter. The “cpsd” function also uses Hanning windowing. The window size is equivalent to one quarter of the length of the filtered time sequence array of grayscale data. The default overlap is used, which is half of the window length. The sampling frequency is the last input parameter in the “cpsd” function. These parameters are all the same for the “cpsd” function as they are for the “mscohere” function, described in Section 5.4.2.

In regard to cross power spectral density results, the angle of the phase lag is calculated based on the real and imaginary parts of the complex result at each frequency. This is done using the negative of the “angle” function in MATLAB. The resulting phase angles are smoothed using the smoothing process presented in Table 5.2. Phase angle results associated with five pairs of pixel locations from the same regions are ensemble-averaged. The phase lag value at a particular frequency represents the angle associated with the difference in phase of the two signals at that frequency.

Phase lag magnitudes are converted into time lag magnitudes by dividing phase lag values by associated radial frequency values, as given by

$$\tau = \frac{\phi}{2\pi f} \quad (5.11)$$

Although the phase and time lags are calculated at each discrete frequency between 0 and the Nyquist Folding frequency, the only meaningful phase lag results are at frequencies associated with strong coherence. Because the boundary layer signal is represented by the first term in the cross-power spectral density function, positive times and positive phase lag values indicate that the perturbation in the boundary layer occurs prior to the perturbation in the shock wave. Negative values indicate that the boundary layer disturbance occurs after the shock wave disturbance at the same frequencies. Note that

the range of phase lag in this analysis is limited to values between  $-\pi$  and  $\pi$ . Spurious results may arise if the actual time lag corresponds to a phase lag that is outside of these limits (at a value of  $3\pi/2$ , for example).

#### **5.4.4 Spatial Variations**

The magnitude squared coherence and the time lag are determined for different pixel locations for certain frequencies. The magnitude squared coherence and the time lag are determined between pixels along line locations in the boundary layer or along line locations in the shock wave, relative to a pixel location associated with the shock wave. In this process, the magnitude squared coherence and time lag are calculated and smoothed, but are not ensemble averaged.

The magnitude squared coherence and time lag results at frequencies of 20 Hz, 40 Hz, and 100 Hz are considered with respect to spatial position. As such, the magnitude squared coherence and time lag at these frequencies are determined for one location, relative to a range of other spatial locations. Within the present investigation, analysis results are given: (i) between a location associated with the normal shock wave, relative to locations near to the shock wave, and (ii) between a location associated with the normal shock wave, relative to other locations within the upstream and downstream boundary layers. For (ii), the magnitude squared coherence and time lag are smoothed spatially using a running average scheme. The data associated with a pixel location is replaced by the average of the data from the considered pixel location and from the 5 adjacent pixel locations on both sides of the considered location.

## **CHAPTER 6. TEST SECTION MODIFICATIONS**

Test section and facility changes which are investigated include: (i) the distance from the entrance of the test section to the leading edge of the shock wave holding plate, (ii) the height of the bottom of the shock wave holding plate with respect to the bottom wall, (iii) the angle of the choking flap, and (iv) the spectacle blind to the 4 inch diameter venting valve is positioned as fully closed, fully open, or half open. Tests illustrating the results of these changes are described within the present chapter.

Although these four parameters are changed between each test, the general configuration of the test section is the same for all tests, except for the test on 22 February 2017, which uses a different shock wave holding plate. Figure 6.1 shows the configuration of the test section for these tests. The three dimensions that are modified are labeled with variables. Table 6.1 indicates the values for those dimensions, the state of the 4 inch venting valve, and other notes pertinent to each test.

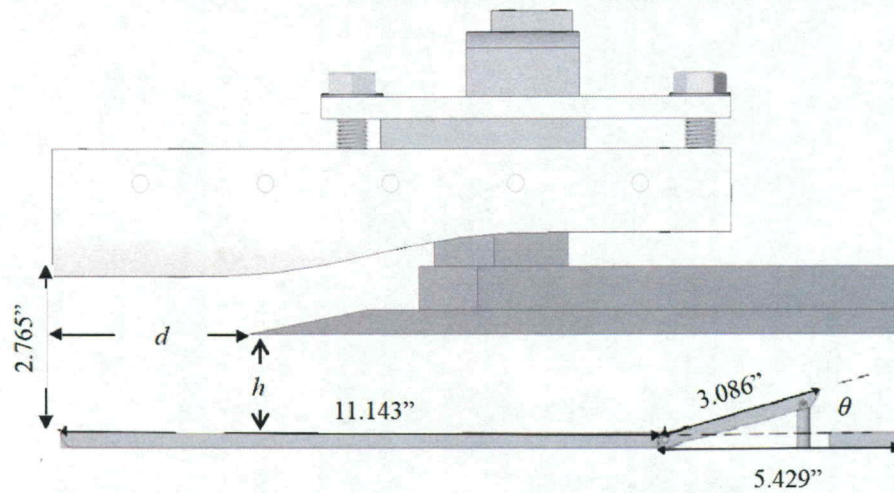


Figure 6.1: The configuration of the test section. Three of the dimensions vary among tests and are labeled with variables.

Table 6.1: The wind tunnel configuration for each of the tests. The dimensions correspond to the variable dimensions in Figure 6.1.

Test Date	Shock Wave Holding Plate Placement		Choking Flap Angle $\theta$ ( $^{\circ}$ )	4" Vent	Notes
	Height $h$ (in)	Entrance Distance $d$ (in)			
22-Feb-17	--	--	1.5	Closed	Different SWHP
29-Sep-17	1.4	4.77	3.3	Closed	
8-Nov-17	1.4	4.77	3.58	Closed	Refinished SWHP
13-Nov-17	1.4	4.77	3.7	1/2 Open	
15-Nov-17	1.4	4.77	3.7	Open	
5-Dec-17	1.65	4.77	3.7	1/2 Open	
8-Dec-17	1.21	4.77	3.7	1/2 Open	
13-Dec-17	1.21	4.77	3.16	1/2 Open	
20-Mar-18					
22-Mar-18	1.47	5.2	4.3	1/2 Open	
04-Apr-18					
05-Apr-18	1.47	5.45	3.92	1/2 Open	

For the test on 29 September 2017, the shock wave holding plate is positioned 1.4 inches above the bottom wall and 4.77 inches from the entrance of the test section. The total height of the test section, from the bottom wall to the top wall, at the tip of the shock wave holding plate, is 2.79 inches. The total mass flow rate through the test section is 27.6 lbm/s. The shock wave holding plate is approximately centered such that 50 percent of the flow goes through the bottom passage and 50 percent goes through the

top passage. The mass flow rate below the shock wave holding plate is approximately 13.9 lbm/s; the mass flow rate above the shock wave holding plate is approximately 13.6 lbm/s. The choking flap is angled at  $3.3^\circ$ . The exhaust is completely closed. Note that, for tests conducted after 29 September 2017, the tip of the shock wave holding plate is sharpened to remove any divots or non-uniformities. Material from the bottom of the shock wave holding plate is also removed to flatten its surface and make it parallel with the bottom wall. Furthermore, an extension to the back of the shock wave holding plate is added. Figure 6.2 shows a technical drawing of the shock wave holding plate used during the test on 29 September 2017. Figure 6.3 shows the shock wave holding plate with the piece added to the back. This modified shock wave holding plate is then employed for all tests during this test series after the test on 29 September 2017.

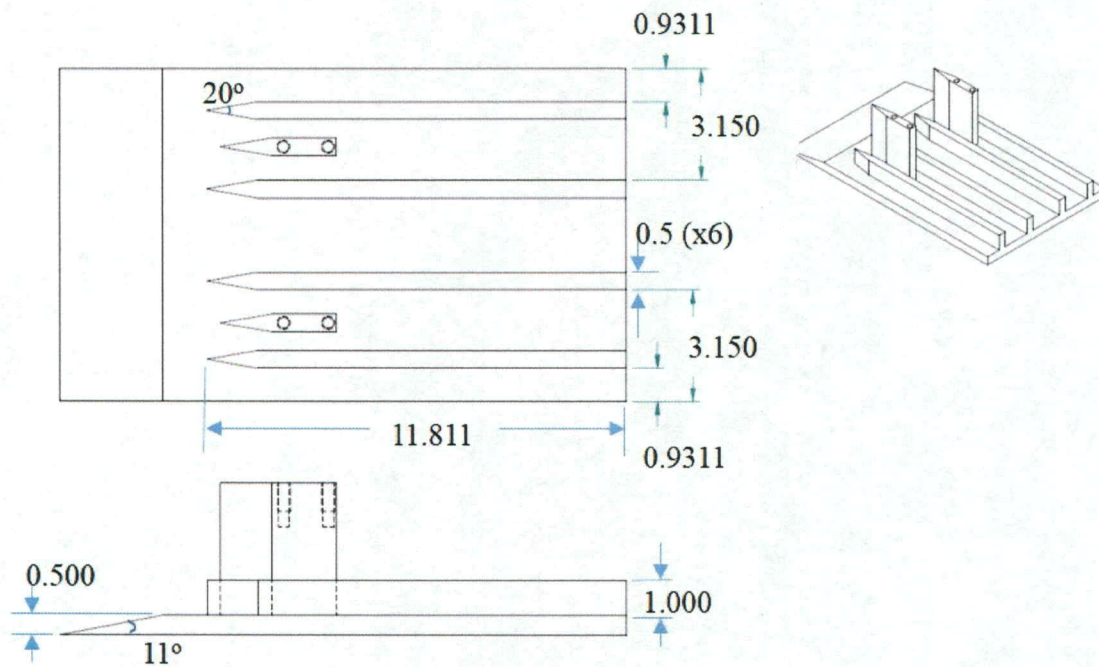


Figure 6.2: The shock wave holding plate prior to its modifications between September and November 2017.



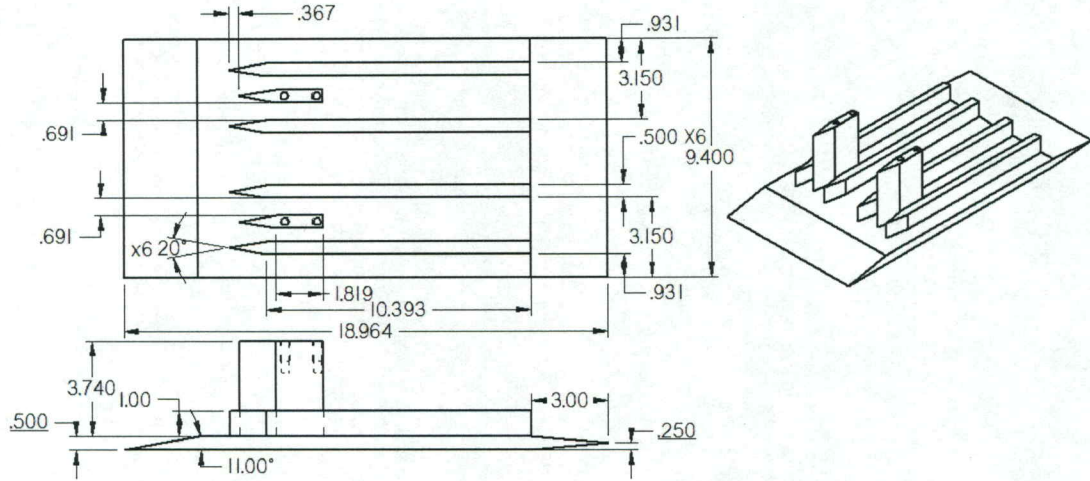


Figure 6.3: The modified shock wave holding plate. This plate is used for all tests after and including 08 November 2017.

Between the test on 29 September 2017 and the test on 08 November 2017, the shock wave holding plate is refinished and the choking flap is raised  $0.28^\circ$  from  $3.3^\circ$  to  $3.58^\circ$ . With the flattened surface and higher choking flap angle, the ratio of the flow area at the entrance to the bottom passage to the smallest flow area at the choking flap is 1.16.

The choking flap is raised to  $3.7^\circ$  for the test on 13 November 2017, increasing the area ratio to 1.17. The 4 inch vent is also installed on the exhaust plenum. The 4 inch vent is described in Section 3.3.4. The spectacle blind valve to this vent is positioned such that the vent is half open for the test on 13 November 2017. The vent is then fully opened for the test on 15 November 2017. Increasing this venting area decreases the pressure in the exhaust plenum.

On 05 December 2017, the shock wave holding plate is moved upward, away from the bottom wall. It is moved 0.25 inches upward, to a position 1.65 inches from the bottom wall. This arrangement provides a mass flow rate of approximately 16.3 lbm/s below the shock wave holding plate and 11.2 lbm/s above the shock wave holding plate.

This corresponds to 59 percent and 41 percent of the mass flow rate in the lower and upper passages, respectively. This also changes the area ratio in the bottom passages to 1.14. The ratio of the entrance area and the smallest area in the top passage is 1.12. The 4 inch venting valve is returned to the half open position. On 08 December 2017, the shock wave holding plate is moved down 0.44 inches to a position 1.21 inches above the bottom wall. This arrangement gives mass flow rates of 11.9 lbm/s and 15.7 lbm/s, corresponding to 43 percent and 57 percent of the mass flow, below and above the shock wave holding plate respectively. This increases the area ratio in the bottom passage to 1.20. For the test on 13 December 2017, the choking flap is lowered  $0.54^\circ$  from  $3.7^\circ$  to  $3.16^\circ$ . This lowers the area ratio in the bottom passage from 1.20 to 1.16.

For the tests on 20 and 22 March 2018, the shock wave holding plate is moved downstream and upward. The choking flap is also raised. The shock wave holding plate is moved 0.43 inches downstream. The tip of the shock wave holding plate is 5.2 inches from the entrance to the test section. Recall that the top wall of the test section diverges. The total height of the test section at the tip of the shock wave holding plate is 2.83 inches. The maximum Mach number at this location using quasi-one-dimensional, isentropic, flow relationships is 1.60. The shock wave holding plate is also moved upward such that the bottom of the shock wave holding plate is 1.47 inches from the bottom wall. It is estimated that a mass flow rate of 14.3 lbm/s flows beneath the shock wave holding plate; a mass flow rate of 13.2 kg/s flows above the shock wave holding plate. The choking flap is raised to  $4.3^\circ$ . This combination of changes makes 52 percent of the mass flow rate go through the bottom passage and 48 percent go through the top

passage. The entrance to smallest flow area ratios are 1.19 and 1.06 for the bottom and top passages respectively.

The shock wave holding plate is moved downstream for the tests on 04 and 05 April 2018. The tip of the shock wave holding plate is 5.45 inches from the entrance to the test section. The total height of the test section at this location is 2.87 inches. Using quasi-one-dimensional, isentropic, flow relationships, the maximum Mach number upstream of the shock wave is 1.63. The mass flow rate beneath the shock wave holding plate is estimated to be 14.1 lbm/s, and the mass flow rate above the shock wave holding plate is 13.4 lbm/s, corresponding to 51 percent and 49 percent of the mass flow rate, respectively. The choking flap is lowered from  $4.3^\circ$  to  $3.92^\circ$ , decreasing the area ratio in the bottom passage to 1.17. The area ratio in the top passage also decreases to 1.04.

## **6.1 Pressure Data**

Pressure is measured and recorded for the majority of the wind tunnel tests. Pressure is measured at the pressure regulating valve, upstream of the shock wave along the bottom wall of the test section, downstream of the shock wave along the bottom wall of the test section, and in the exhaust plenum. Additional details about the location and acquisition of the pressure data are given in Section 4.1. The pressures from the pressure regulating valve, the test section upstream of the shock wave, and the exhaust plenum are presented here. The pressures with respect to time are similar for all of the tests.

The pressures measured during the test on 08 November 2017 are shown in Figure 6.4 with respect to time. A transient period, during start-up of the facility, lasts between 0 seconds and 7 seconds. Flow conditions are established at approximately 7 seconds and are maintained until approximately 10 seconds. Note that during times

when flow conditions are established, except for signal noise, the pressures are relatively constant and invariant with respect to time. After 10 seconds from the start of the test, there is another transient period, during shut-down of the facility, during which the pressure regulating valve is closed. While flow conditions are established, the static pressure in the test section is approximately 13.5 psia. The pressure regulator reads an inlet stagnation pressure of approximately 55 psia. The pressure in the exhaust plenum is approximately 19.5 psia. This gives an exhaust plenum pressure to regulator pressure ratio of 0.355.

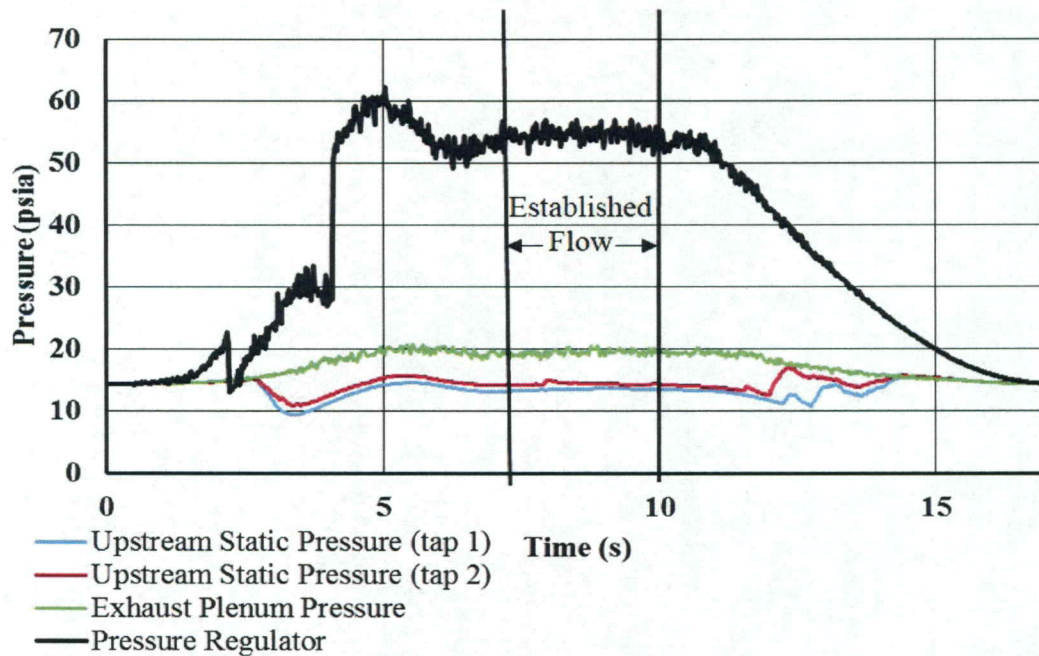


Figure 6.4: The measured pressures in the test section, the exhaust plenum, and the pressure regulator with respect to time for the test on 08 November 2017. Flow conditions remain established for approximately 3 seconds between 7 and 10 seconds.

The pressures are shown with respect to time in Figure 6.5 for the test on 13 November 2018. The static pressure upstream of the shock wave in the test section is approximately 13.5 psia. The pressure near the pressure regulating valve is approximately 55 psia, which is considered to be the test section inlet stagnation pressure. With the

4 inch valve half open, the pressure in the exhaust plenum is less than during the test of 08 November 2017, when the vent is closed. The pressure in the exhaust plenum is approximately 18.8 psia. The exhaust plenum to pressure regulator pressure ratio is 0.342. Flow conditions are established at 7 seconds. The established flow conditions are maintained until 12 seconds. The duration of start-up, shut-down, and the established flow periods vary between tests; however, the average pressures during the established flow period are about the same for most of the tests after 13 November 2017. Figure 6.5 is a representative plot for all the tests conducted after 13 November 2017, except for the test on 15 November 2017 which never achieves stable flow conditions.

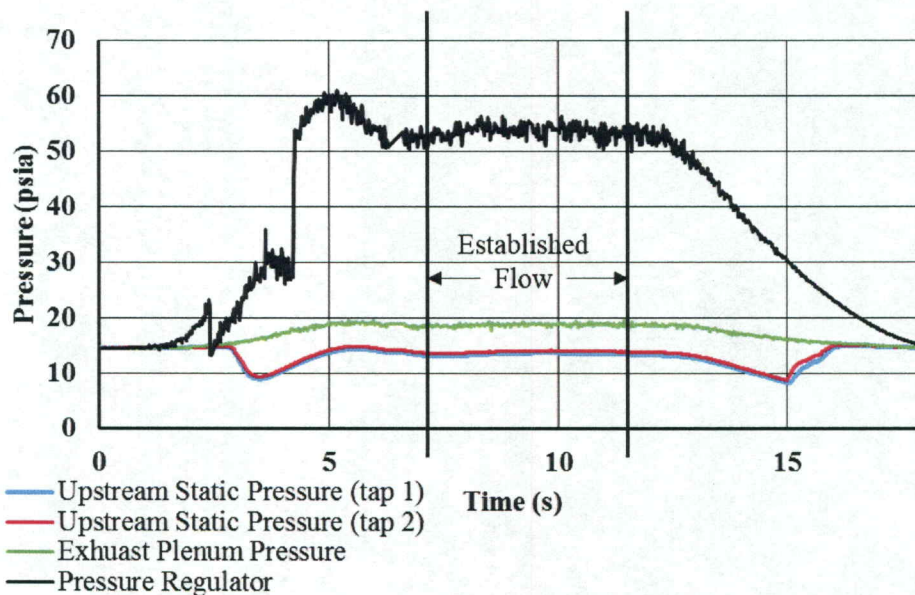


Figure 6.5: Pressure data from the test on 13 November 2017. Pressures are relatively constant between 7 and 12 seconds. This plot represents the pressure data collected during all tests where the 4 inch vent is half open.

## 6.2 Characteristic Flow Visualization Data

The shadowgraph images from each test show the structure of the shock wave and other flow features. The effects of the test section modifications are made apparent by

comparing characteristic shadowgraph flow visualization images from each test.

Figure 6.6 and 6.7 show flow visualization images with the relevant features labeled.

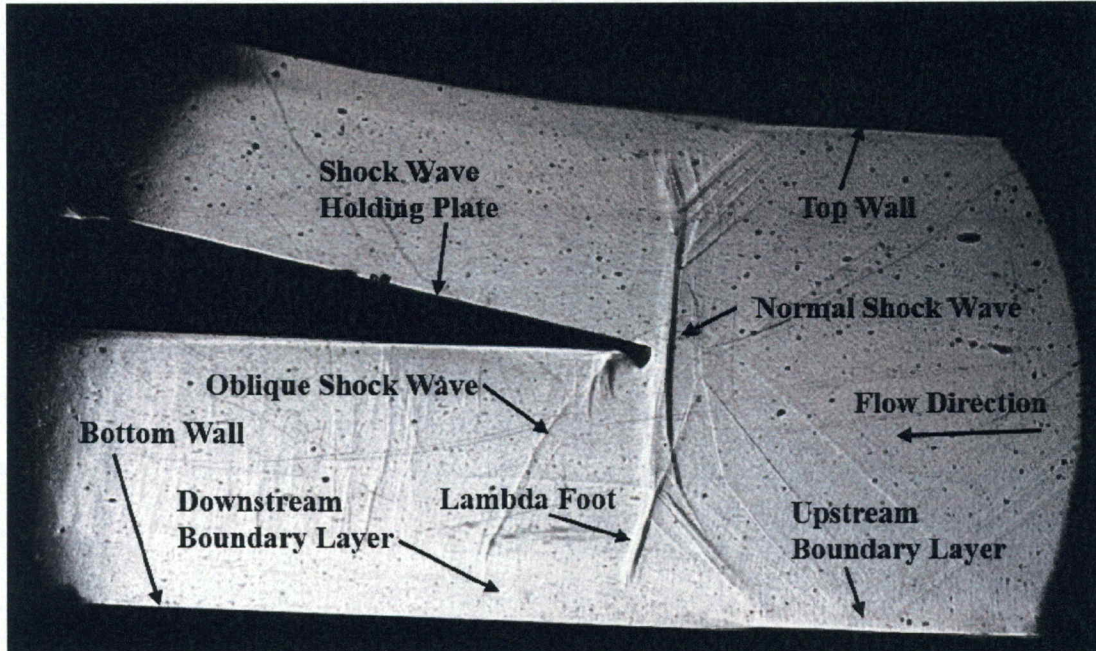


Figure 6.6: Flow Visualization image with flow features labeled. This image is from the test on 29 September 2017.

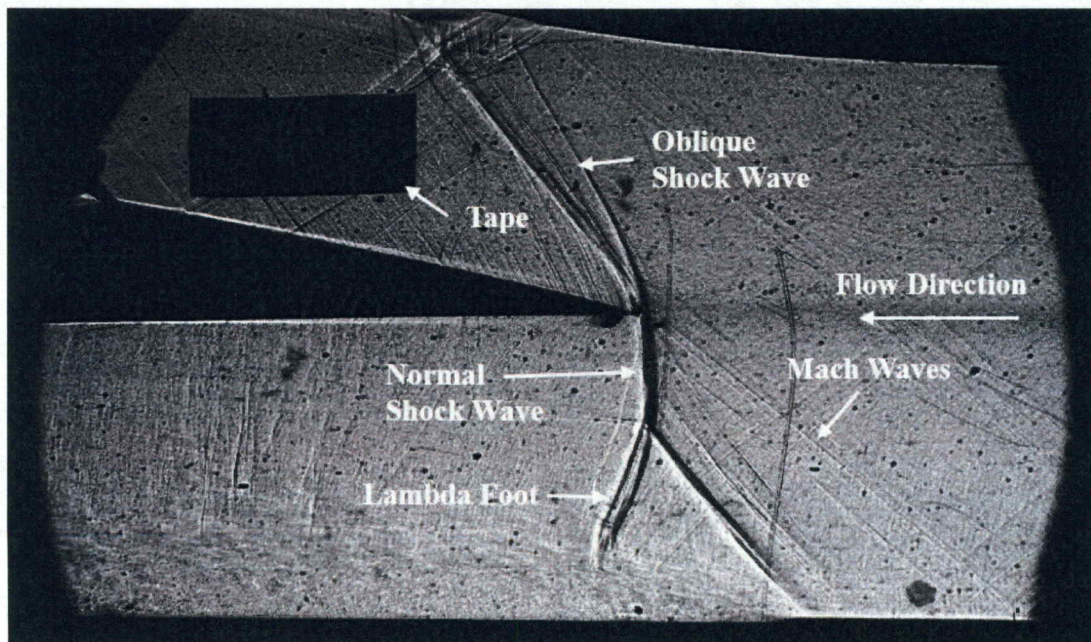
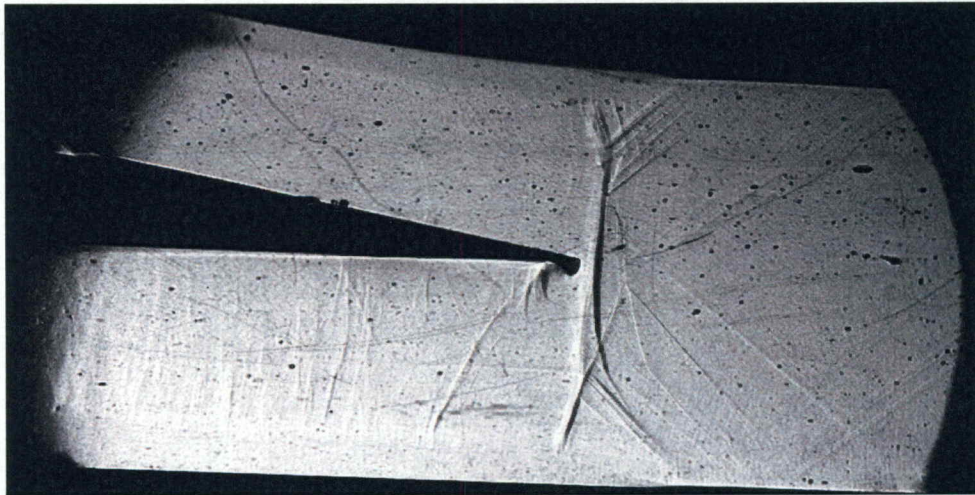


Figure 6.7: Flow visualization image showing an oblique shock wave impinging on the top wall. This image is from the test on 05 April 2018.

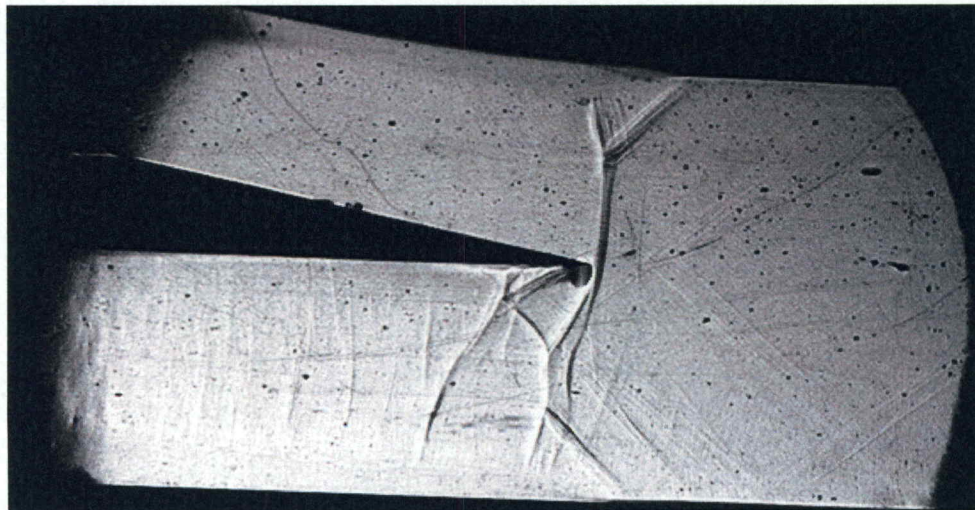
A shock wave forms upstream of the tip of the shock wave holding plate and impinges on the top and bottom walls of the test section. The shock wave impinging on the bottom wall is normal. The shock wave impinging on the top wall can be normal or oblique, depending on the test section configuration. Figure 6.6 shows normal shock waves impinging on the top and bottom walls. Figure 6.7 shows an oblique shock wave reflecting off the top wall and a normal shock wave impinging on the bottom wall. With a normal shock wave or oblique shock wave, the shock wave can be attached or separated from the tip of the shock wave holding plate. The normal shock waves have a distinct lambda pattern that is characteristic of normal shock wave boundary layer interactions. A flow separation region forms within the boundary layer downstream of the shock waves. In Figures 6.6 and 6.7, flow enters from the right side of the images. Mach waves are also visible as faint oblique lines in these images. According to Ogawa and Babinsky [1], these Mach waves have “negligible effects on the flow.” The Mach waves are caused by imperfections on the surfaces of the wind tunnel and joints between the sections of the wind tunnel. The dark spots are due to imperfections on the side walls of the wind tunnel. They do not affect the flow. In some shadowgraph images presented in this thesis, such as in Figure 6.7, a dark rectangle is located above the shock wave holding plate. It is a piece of tape on the outside of the side wall windows that provides a length scale for the image. Also, note that the bottom wall of the test section is horizontal in all tests. It appears to be at an angle in some of the flow visualization images due to misalignment of the Phantom v711 camera.

Sequences of flow visualization images from the same tests illustrate the unsteadiness surrounding the shock wave based on the changing position of the shock

wave. The unsteadiness causes the shock wave to oscillate in the streamwise direction. Figures 6.8 and 6.9 exemplify such unsteady flow variations. Both images are from the time when flow conditions are established during the test on 29 September 2017. The significant amplitude of the shock wave oscillation is evident by comparing the streamwise location of the shock wave, particularly in the bottom passage, with respect to the shock wave holding plate tip in the two images.



*Figure 6.8: A typical flow visualization image from the test on 29 September 2017.*

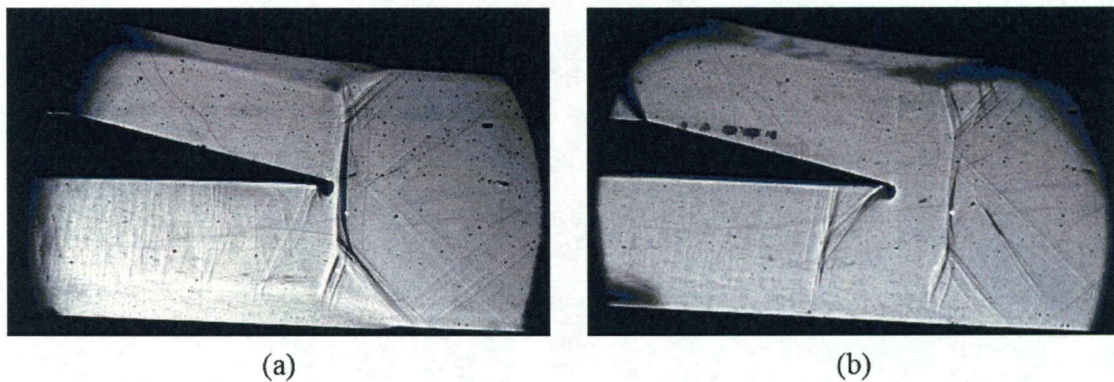


*Figure 6.9: Another typical flow visualization image from the test on 29 September 2017.*



### 6.3 Effect of SWHP Refinishing

Figure 6.10 shows flow visualization images from (a) 29 September 2017 with the original shock wave holding plate and (b) 08 November 2017 with the refinished shock wave holding plate. Both images show the presence of a normal shock wave impinging on the top and bottom walls. During the test on 08 November 2017, the shock wave is detached from the shock wave holding plate tip; it is nearly attached during the test on 29 September 2017. Note that the two white dots in the Figure 6.10 represent the average pixel locations near the shock wave and lambda foot where the grayscale data are analyzed.



*Figure 6.10: Flow visualization images from (a) 29 September 2017 with the original shock wave holding plate, and (b) 08 November 2017 with the shock wave holding plate refinished.*

Figure 6.11 (a) and (b) show the grayscale spectral energy with respect to frequency at locations near the shock wave and the lambda foot for tests before and after the shock wave holding plate is refinished. Changing the shock wave holding plate does not significantly affect the unsteadiness of the flow field near the shock wave. The energy at low frequencies lessens slightly, especially between frequencies of 3 Hz and 10 Hz or Strouhal numbers of 0.00039 and 0.00132. The same spectral peaks are present before and after the shock wave holding plate is refinished. Near the lambda foot, the

unsteadiness seems to decrease at approximately 2 Hz and 11 Hz ( $St_r = 0.00026$  and  $0.00145$ ) and increase around 6 Hz ( $St_r = 0.0008$ ), but these changes are minimal. Both data sets have approximately the same sampling frequency and frequency resolution.

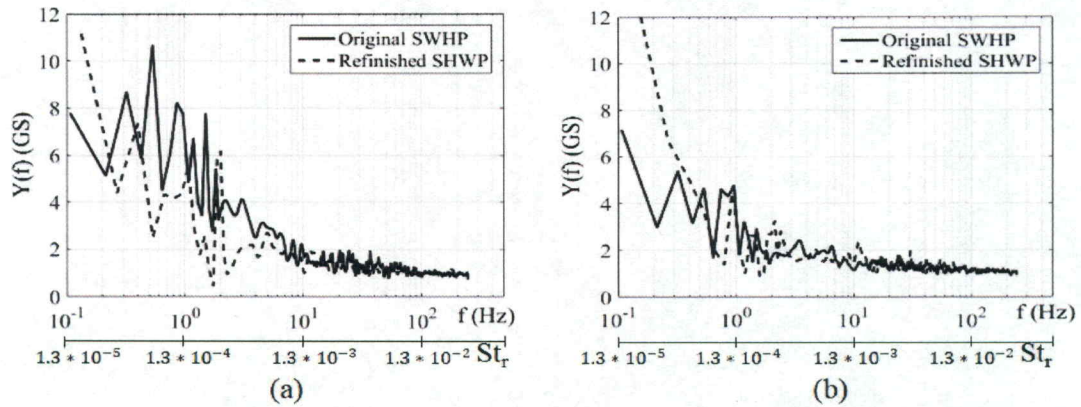


Figure 6.11: Grayscale spectral energy distributions from locations near the (a) shock wave and (b) lambda foot for the tests on 29 September 2017 and 08 November 2017 with the original and refinished shock wave holding plate.

#### 6.4 Effects of Plenum Venting

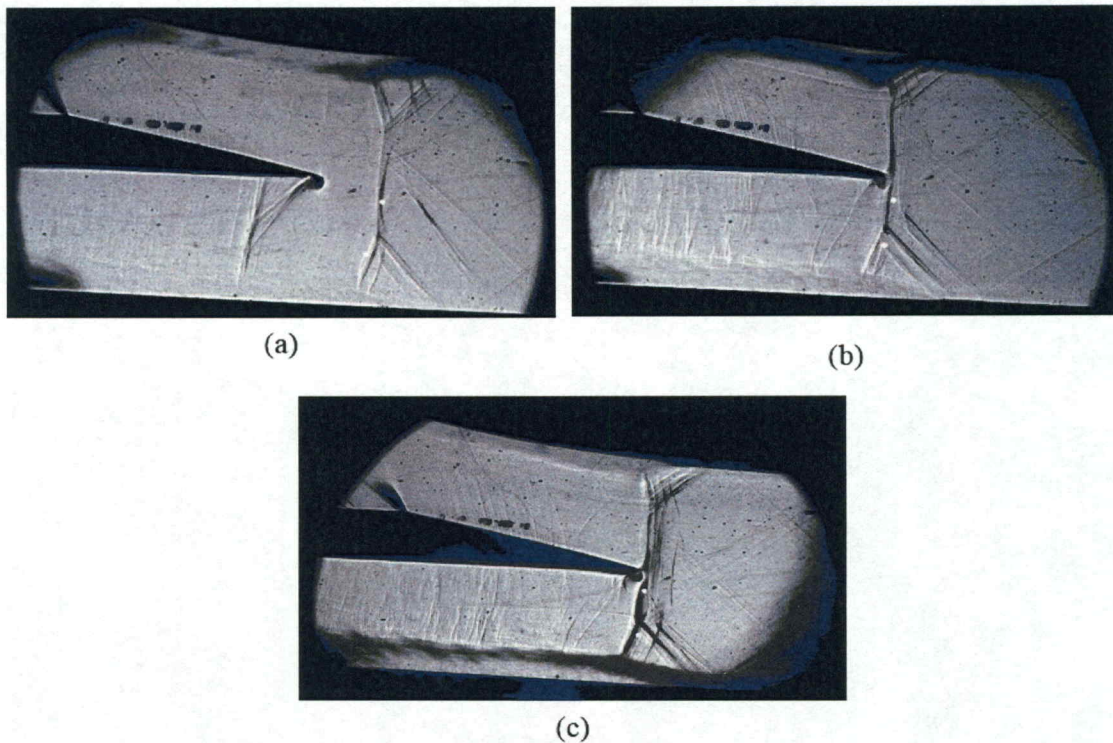
As the 4 in vent on the exhaust plenum is opened, the pressure in the exhaust plenum decreases. With the vent fully closed, the pressure in the exhaust plenum is approximately 19.5 psia. The average pressure in the exhaust plenum with the vent half open and fully open is 18.8 psia and 18.0 psia, respectively. The pressures upstream of the shock wave are unchanged when the valve is half open as compared to when it is closed. Thus, the ratio of exhaust plenum to pressure regulator pressure decreases from 0.355 to 0.342 to 0.332 as the vent is opened. These changes are shown in Table 6.2.

Table 6.2: Effects of opening the 4 inch diameter exhaust vent on the plenum pressure and pressure ratio

Test Date	4 inch Vent Setting	Vent Area (in <sup>2</sup> )	Exhaust Plenum Pressure (psi)	$P_e/P_t$
8-Nov-17	Closed	0	19.5	0.355
13-Nov-17	1/2 Open	6.3	18.8	0.342
15-Nov-17	Open	12.6	18.0	0.332

The average position of the shock wave moves downstream, closer to the shock wave holding plate, as the vent is opened and the pressure ratio decreases. This is shown in Figure 6.12, where the shadowgraph images in Figure 6.12 (a), (b), and (c) correspond to exhaust plenum to regulator pressure ratios of 0.355, 0.342, and 0.332, respectively. All three images show normal shock waves impinging on the top and bottom walls. The downstream change in the mean position of the shock wave can be attributed to the decrease in exhaust plenum pressure to regulator pressure ratio and the geometry of the test section. John [29] relates shock position in diffusers and exhaust pressure. In diffusers and diverging nozzles, such as the test section used in the present study, when the ratio of exhaust pressure to upstream stagnation pressure decreases, the shock wave becomes stronger and moves downstream where the flow area is larger. In this case, the regulator pressure is the best approximation of the stagnation pressure upstream of the shock wave. The shock wave changes position such that the combination of the pressure rise across the shock wave, and any changes in static pressure upstream and downstream of the shock wave, make the pressure at the test section exit equal to the pressure in the exhaust diffuser plenum.

A secondary oblique shock wave at the tip of the shock wave holding plate is present in all three of these tests. It is most prominent in Figure 6.12 (a) with the vent closed and the shock wave farthest upstream. With this configuration, the secondary oblique shock wave system also includes a normal shock wave.



*Figure 6.12: Shadowgraph images comparing the tests with exhaust pressure to regulator pressure ratios of (a) 0.355 (b) 0.342 and (c) 0.332. These correspond to test on 08 November 2017, 13 November 2017, and 15 November 2017, respectively.*

The very low frequency unsteadiness in the flow near the shock wave changes based on the amount of venting as well. The peak unsteady frequency is between 1 and 2 Hz, corresponding to Strouhal numbers between 0.00013 and 0.00026. Venting the exhaust plenum creates additional unsteadiness at approximately 5 Hz or a Strouhal number of 0.00066. This occurs for the tests with the 4 inch vent half open and fully open. The unsteadiness at this frequency is greatest when the vent is fully open. Opening the vent lessens the relative spectral peak at a frequency around 11 Hz ( $St_r = 0.00145$ ). Figure 6.13 shows the grayscale spectral energy near (a) the shock wave and (b) the lambda foot with respect to time. Note that some variations between grayscale spectral energy distribution data from different tests are present due to different acquisition rates and frequency resolutions.

As the pressure ratio decreases the total spectral energy increases. Figure 6.14 shows the spectral energy of the ensemble averaged spectra, as well as the maximum and minimum spectral energies based on a single pixel location. This increase in spectral energy is believed to be caused by additional unsteadiness in the flow or by a better defined or stronger shock wave structure in the shadowgraph visualization image.

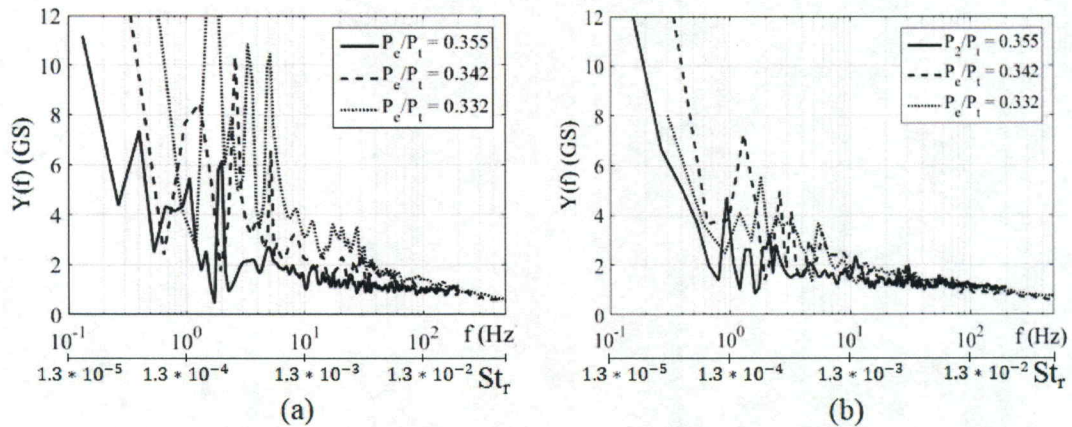


Figure 6.13: Representative grayscale spectral energy distributions for locations near the (a) shock wave and (b) lambda foot, comparing the effects of the 4 inch vent position. Pressure ratios are 0.355, 0.342, and 0.334 for closed, half, and fully open venting.

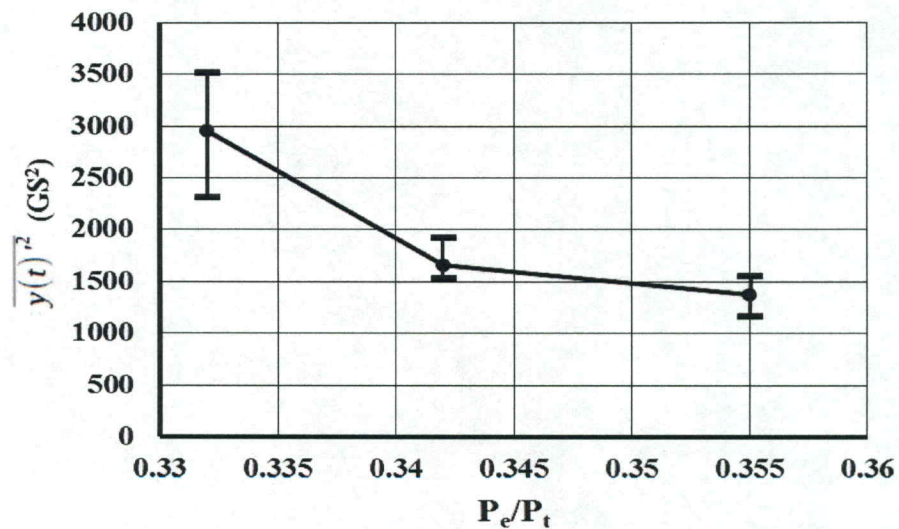
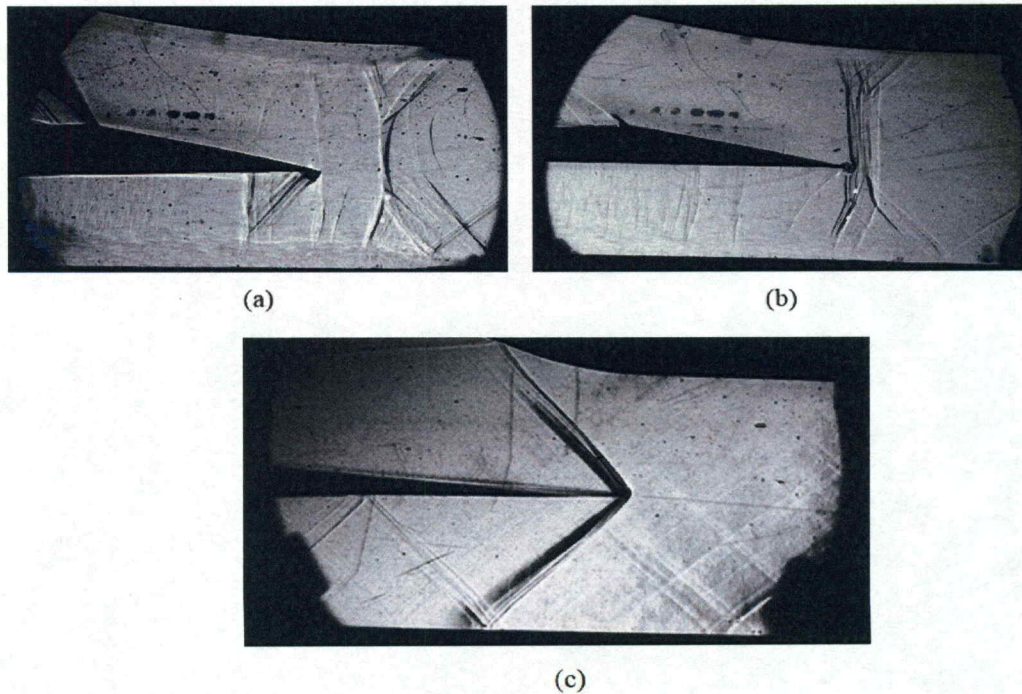


Figure 6.14: Total grayscale spectral energy near the shock wave with respect to exhaust plenum to regulator pressure ratio. Dots show average energy of five pixels; error bars indicate maximum and minimum energy.

## 6.5 Effect of Choking Flap Angle

Raising the choking flap moves the shock wave upstream, as is shown in Figure 6.15 (a), (b), and (c). This is due to a higher local pressure downstream of the shock wave when the choking flap is at a larger angle. Figure 6.15 (a) and (b) are from tests on 08 December 2017 and 13 December 2017. The choking flap angles for these tests are  $3.7^\circ$  and  $3.16^\circ$ . Figure 6.15 (c) is for the test on 22 February 2017 with the choking flap at  $1.5^\circ$ . This test uses a slightly different test section configuration and the data are collected using schlieren techniques, not a shadowgraph.

Note that there are many lines representing the shock wave in Figure 6.15 (b). This may indicate that the shadowgraph visualization system is misaligned. The visualization system is aligned using the methods presented by Settles [26] prior to the test but is not rechecked after the test.



*Figure 6.15: Flow visualization images from tests with bottom passage entrance to smallest area ratio of (a) 1.20, (b) 1.16, and (c) 1.04.*

When the choking flap is at a higher angle, there is a larger area ratio between flow area at the entrance to the bottom channel and the smallest flow area. This is presented in Table 6.3.

*Table 6.3: The entrance to smallest area ratio in the bottom passage due to adjusting the choking flap angle.*

<b>Test Date</b>	<b>Choking Flap Angle <math>\theta</math> (<math>^{\circ}</math>)</b>	<b><math>A/A_{\min}</math> Bottom Passage</b>
22-Feb-17	1.50	1.06
13-Dec-17	3.16	1.16
8-Dec-17	3.70	1.20

The flow through the smallest flow area is often choked with a Mach number equal to 1. With the choking flap angled at  $3.7^{\circ}$ , the area ratio is 1.20; the area ratio is only 1.16 with the choking flap angled at  $3.16^{\circ}$ . Since the flow is subsonic over that region, a larger area ratio creates a larger pressure ratio. The static pressure is measured 0.6 inches behind the tip of the shock wave holding plate (0.6 inches into the bottom, constant-area, channel). The pressures in this location are 24.60 psia and 23.42 psia for tests with  $A/A_{\min} = 1.20$  and  $A/A_{\min} = 1.16$ , respectively. This corresponds to a 5.04% increase in pressure between the two tests. The measurement location is near a shock wave in both cases, so it may not accurately represent the true back pressure. Note that the pressure jump is smeared over a larger streamwise distance because of the shock wave boundary layer interaction [17]. Nonetheless, it does indicate that the pressure in the lower passage increases as its area ratio increases. With the choking flap at  $1.5^{\circ}$ , the area ratio is estimated to be 1.04. In this case there is not enough back pressure to cause a normal shock wave and the shock wave in the bottom passage is oblique. Higher back pressure results in a shock wave farther upstream in a diverging nozzle [29]. This indicates that more severe restriction of the flow area downstream of the shock wave causes the shock wave to move upstream. This

is exactly the result observed in the present study. The results of present study are also similar to the results of Ott et al. [3], who choked the flow using a cam. The attached secondary oblique shock wave system is much more defined during the test with the higher choking flap angle. In fact, a third normal shock wave or Mach wave intermittently forms at the tip of the shock wave holding plate. This is visible in Figure 6.15(a). The presence of the second shock wave system does provide additional pressure rise to the flow as it travels downstream. Hence, without the secondary oblique shock wave system, the normal shock wave is expected to be farther upstream in the diverging nozzle.

The grayscale spectral energy are shown in Figure 6.16 (a) and (b) for the data taken near the shock wave and near the lambda foot, respectively. Smaller area ratios due to lower choking flap angles create unsteadiness at distinct frequencies, as opposed to the broadband unsteadiness associated with the larger area ratio and choking flap angle. The case with an area ratio of 1.16 also causes unsteadiness near the shock wave between 0.6 and 3 Hz, corresponding to Strouhal numbers between 0.00008 and 0.00039, that is not present in the test with the area ratio of 1.20.

The grayscale spectral data from the test with the smaller area ratio equal to 1.16 has more overall spectral energy than the test with an area ratio of 1.20. This could be from greater unsteadiness at frequencies between 0.6 and 3 Hz ( $St_r = 0.00008$  and  $0.00039$ ), or from the visualization of a stronger shock wave. This is shown in Figure 6.17.



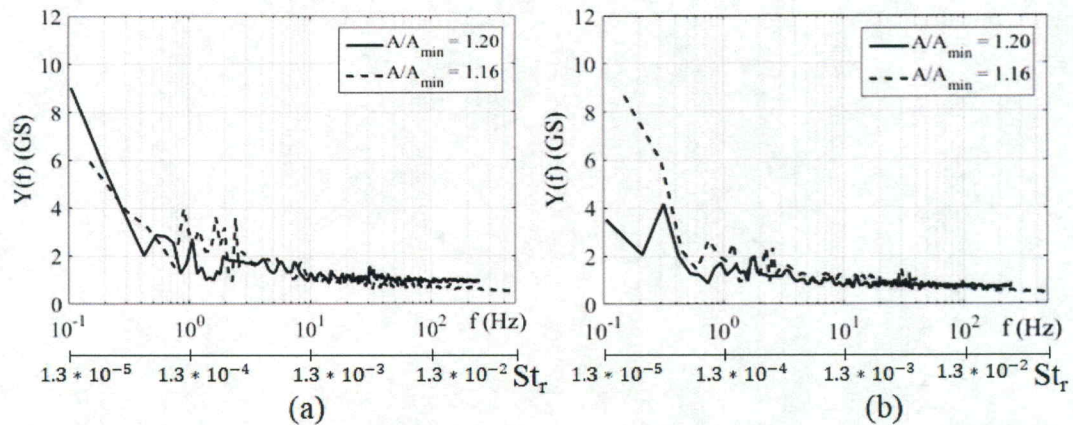


Figure 6.16: Comparison of characteristic grayscale spectral energy distribution due to a change in choking flap angle from data near the (a) shock wave and (b) lambda foot for tests with entrance to smallest area ratios of 1.20 and 1.16.

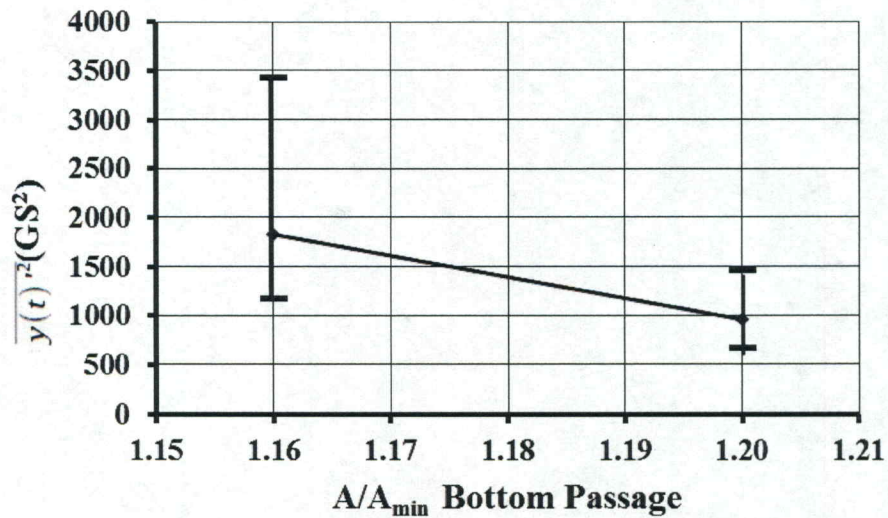


Figure 6.17: The overall spectral energy decreases as area ratio in the bottom passage increases (caused by raising the choking flap). The central line indicates the average energy and the error bars show the minimum and maximum energies from the five pixel locations considered near the shock wave.

## 6.6 Effects of SWHP Height

The shock wave holding plate height determines the area of the two flow channels above and below the shock wave holding plate. Figure 6.18 (a), (b), and (c) show

characteristic shadowgraph images when the shock wave holding plate is positioned 1.40 in, 1.65 in, and 1.21 in above the bottom wall, respectively. These positions correspond to percentages of mass flow in the upper and lower channels of 50 percent and 50 percent, 41 percent and 59 percent, and 56 percent and 43 percent. These are from tests on 13 November 2017, 05 December 2017, and 08 December 2017. Changing the shock wave holding plate height also changes the ratios of the area at the entrance to a passage to the smallest area in that passage. Table 6.4 shows how the mass flow rates and area ratios in the top and bottom passages change as the shock wave holding plate height is altered.

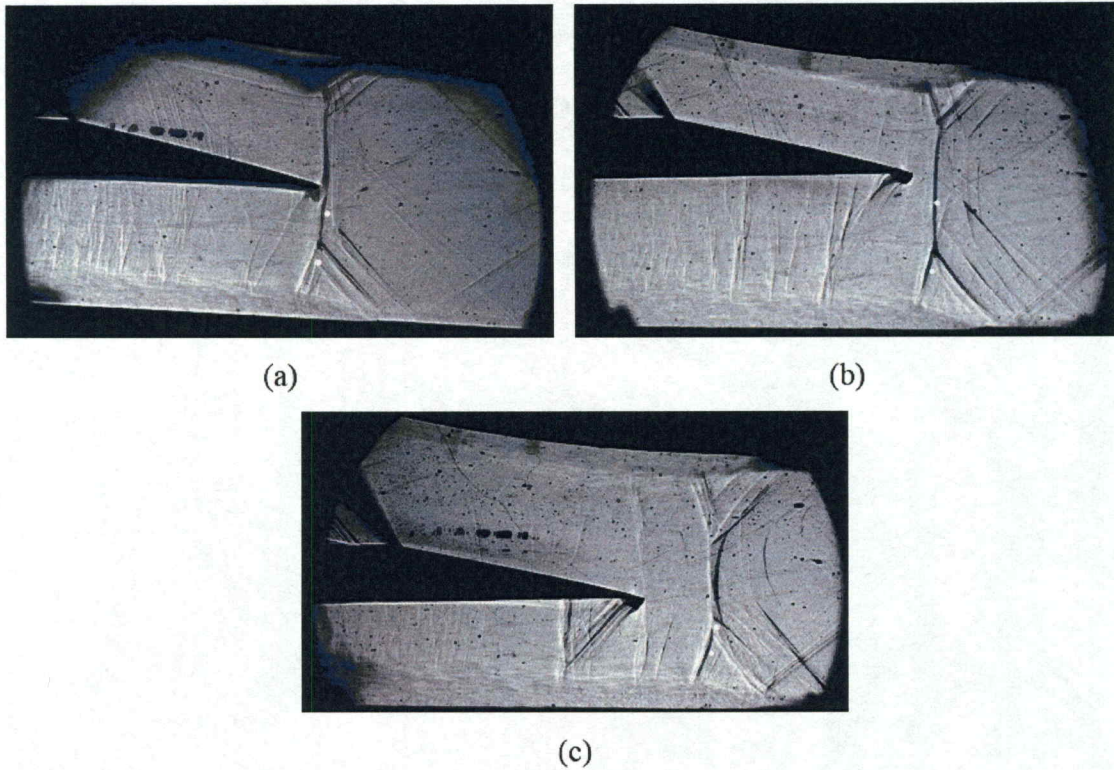
*Table 6.4: Area and mass flow rate changes dues to shock wave holding plate height*

Test Date	SWHP Height h (in)	A/A <sub>min</sub> Top Passage	$\dot{m}_t/\dot{m}$
		A/A <sub>min</sub> Bottom Passage	$\dot{m}_b/\dot{m}$
8-Dec-17	1.21	1.08	0.56
		1.20	0.43
13-Nov-17	1.40	1.10	0.50
		1.17	0.50
5-Dec-17	1.65	1.12	0.41
		1.14	0.59

When the mass flow rates are approximately equal, the shock wave is attached to the tip of the shock wave holding plate. When the shock wave holding plate is moved up or down, the shock wave separates from the shock wave holding plate. For lower shock wave holding plate positions, the separation is caused by the choking flap taking a larger percentage of the flow area; the area ratio increases from 1.17 to 1.20 as the shock wave holding plate is lowered below center. This, therefore, increases the back pressure upstream of the choking flap, moving the shock wave upstream. While the shock wave

holding plate is in a higher position, the supporting structures atop the shock wave holding plate create enough blockage to choke the flow and separate the shock wave from the shock wave holding plate. This is again related to the back pressure increase due to the greater area ratio between the entrance area and most restricted flow area in the top channel.

A secondary oblique shock wave system is also present during all three of the tests considered. It is most visible with the shock wave farthest upstream. It is least visible with the shock wave is very close to the shock wave holding plate. The prominence of the oblique shock wave is related to the stand-off distance between the shock wave and shock wave holding plate. The farther upstream the shock wave, the stronger the secondary oblique shock wave system. This trend is present in all of the tests considered. It is also noticed that the angle of the oblique shock wave is different based on the stand-off distance of the shock wave. The secondary oblique shock wave system is caused by a change in the effective cross sectional area downstream of the shock wave. This change in effective area causes the flow to re-accelerate to supersonic speeds. More distance between the shock wave and the shock wave holding plate permits more re-acceleration, speeding the flow to higher Mach numbers. Greater incoming Mach numbers create stronger shock waves. Also, the higher the Mach number, the smaller the shock wave angle (measured from the incoming flow direction). The change in angle qualitatively agrees with the shadowgraph image data.



*Figure 6.18: Shadowgraph images from the tests on (a) 13 November 2017, (b) 05 December 2017, and (c) 08 December 2017, with the shock wave holding plate positioned 1.4 inches, 1.65 inches, and 1.21 inches, respectively, above the bottom wall.*

There is large-scale unsteadiness in the wind tunnel at approximately 1.2 Hz, 2.5 Hz, and 5 Hz detected near the shock wave and lambda foot. These correspond to Strouhal numbers of 0.00016, 0.00033, and 0.00066, respectively. Decreasing the mass flow rate in the bottom passage from 57 percent to 50 percent and increasing the area ratio in the bottom passage from 1.14 to 1.17 decreases the unsteadiness at 1.2 Hz ( $St_r = 0.00016$ ), but increases the unsteadiness at 2.5 Hz and 5 Hz ( $St_r = 0.00033$  and 0.00066) in the shock wave upstream of the bottom passage. The opposite occurs near the lambda foot. Near the lambda foot, the unsteadiness at 1.2 Hz ( $St_r = 0.00016$ ) increases, and the unsteadiness at the higher frequencies decreases. The total spectral energy also decreases when the mass flow rate in the bottom passage decreases. This

occurs both in the shock wave and lambda foot regions. The overall spectral energy, and thus unsteadiness, lessens when the shock wave holding plate is lowered farther, decreasing the percentage of the mass flow rate in the bottom passage to 41 percent and increasing the area ratio in the bottom passage to 1.20. With this configuration, the unsteadiness at all frequencies lessens. The most prominent frequency is 2.5 Hz, followed by 5 Hz, and 1.2 Hz for the shock wave. It is 1.2 Hz, then 2.5 Hz, and 5 Hz for the lambda foot. The spectral data in Figure 6.19 show these peak unsteady frequencies. The overall spectral energy increases as the mass flow rate through the bottom passage increases and the area ratio in the bottom passage decreases, as is shown in Figure 6.20.

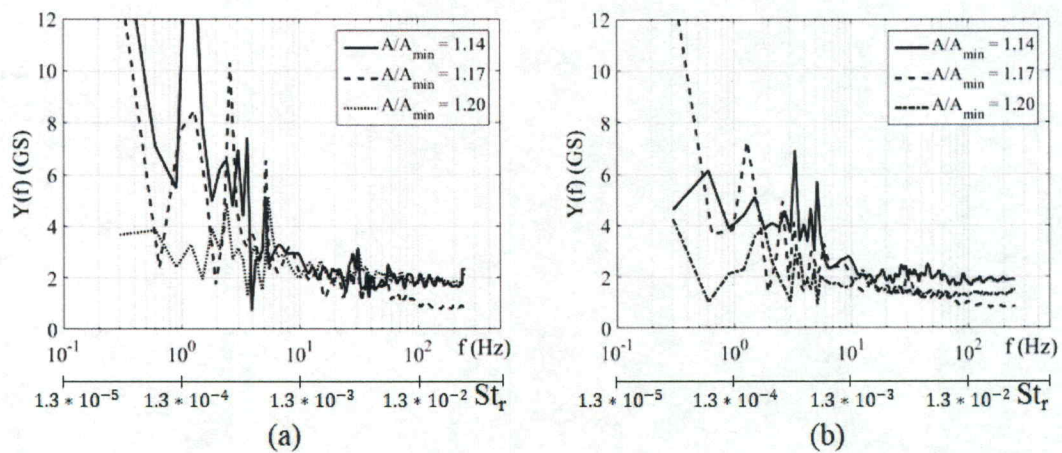


Figure 6.19: Grayscale spectral energy distribution from pixel locations near the (a) shock wave and (b) lambda foot comparing effects of the entrance to smallest area ratio in the bottom passage caused by changing the shock wave holding plate height.

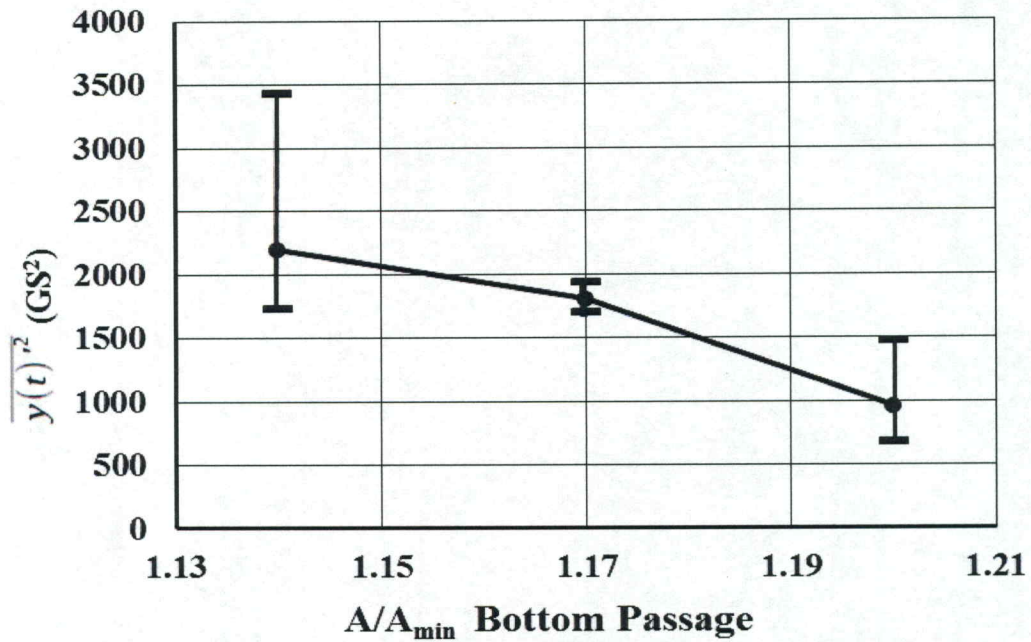


Figure 6.20: Total grayscale spectral energy decreases as the entrance to smallest area ratio in the bottom passage increases. Dots indicate the average of data from five pixels near the lambda foot. The error bars show the maximum and minimum energy.

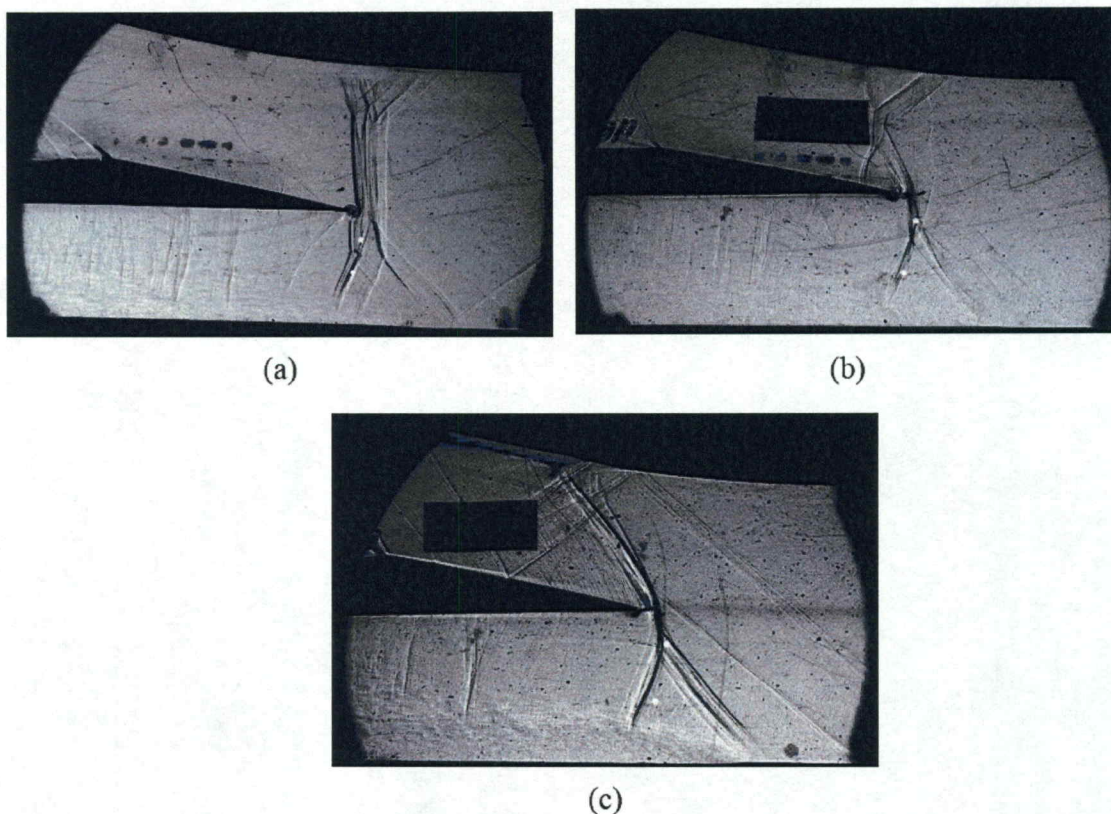
### 6.7 Effects of SWHP Height, SWHP Distance, and Choking Flap Angle

Many changes are implemented between the tests on 13 December 2017, 22 March 2018, and 05 April 2018. Note that the test on 04 April 2018 is the same as that on 05 April 2018. The shock wave is moved downstream and upward and the choking flap angle is adjusted. Table 6.1 provides dimensions for the variable parameters in these configurations. Table 6.5 shows the effects to the area ratios and mass flow rates in the top and bottom passages due to these changes.

*Table 6.5: Changes to the percentage of the mass flow rate and the entrance to smallest area ratios in the top and bottom passages due to a combination of changes associated with tests on 13 December 2017, 22 March 2018, and 05 April 2018.*

Test Date	A/A <sub>min</sub> Top Passage	% ṁ top
	A/A <sub>min</sub> Bottom Passage	% ṁ bottom
13-Dec-17	1.08	56.7
	1.16	43.3
22-Mar-18	1.06	48.0
	1.19	52.0
5-Apr-18	1.04	48.4
	1.17	51.6

Figure 6.21 (a), (b), and (c) show the shadowgraph images from the tests on 13 December 2017, 22 March 2018, and 05 April 2018, respectively. During the tests on 22 March 2018 and 05 April 2018, the shock wave holding plate is positioned such that an oblique shock wave impinges on the top wall of the test section. This is the shock wave pattern described by Ogawa and Babinsky [1]. The oblique shock wave is achieved because of the geometry of the top wall and the shock wave holding plate. In the tests prior to 20 March 2018, the ratio of the area at the entrance of the top channel to the smallest flow area in the upper channel causes the back pressure to be high enough to produce a normal shock wave instead of an oblique shock wave. By moving the shock wave holding plate backward, the contour of the top wall relative to the shock wave holding plate changes, lowering this area ratio and back pressure enough that an oblique shock wave can form. The area ratio in the top passage decreases from 1.08 to 1.04 between the tests on 13 December 2017 and 05 April 2018. The secondary oblique shock wave system in the bottom channel during the test on 13 December 2018 is no longer present in later tests obtained on 22 March 2018, 04 April 2018, and 05 April 2018.



*Figure 6.21: Shadowgraph images from the tests on (a) 13 December 2017, (b) 22 March 2018, and (c) 05 April 2018.*

The unsteadiness in these shock waves at frequencies less than 3 Hz (Strouhal numbers less than 0.00039) are caused by the wind tunnel. The largest unsteadiness is at frequencies approaching the frequency resolution—approximately 0.11 Hz ( $St_r = 0.00001$ ). This is on the timescale of the entire wind tunnel test. The unsteadiness for all three tests is similar for frequencies between 0.5 Hz and 3 Hz or Strouhal number of 0.00007 and 0.00066. There is no clear relationship between the unsteadiness in the shock wave or lambda foot and the changes made to test section configuration for each test. It is noted that the type of shock wave in the upper channel makes little effect on the unsteadiness. Figure 6.22 shows the spectra associated with these tests.



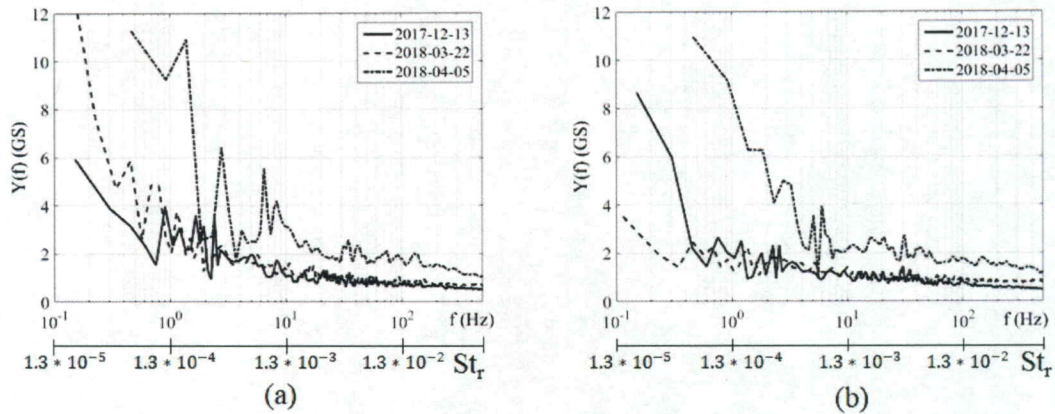


Figure 6.22: Comparison of characteristic grayscale spectral energy for locations near the (a) shock wave and (b) lambda foot. The data is from tests on 13 December 2017, 22 March 2018, and 04 April 2018, and 05 April 2018.

## 6.8 Overall Data Trends

Considering all changes, it is evident that shock wave location and orientation are related to the ratio of the static pressure downstream of the shock wave to the stagnation pressure upstream of the shock wave. As static pressures within the bottom flow passage increase (keeping upstream stagnation pressure a constant), shock waves generally become more normal and are positioned farther upstream. Increasing this pressure can be accomplished by increasing choking flap angle, decreasing the amount of venting from the exhaust plenum, or decreasing the height of the shock wave holding plate relative to the bottom wall. Due to the specific configuration of the present shock wave holding plate, raising the shock wave holding plate near to the top wall can also make the shock wave more normal. Note that increasing the choking flap angle and decreasing the height of the shock wave holding plate increase the ratio of the entrance flow area in the bottom passage to the smallest flow area in the bottom passage. This change in area ratio causes the local static pressure behind the shock wave to increase, thus increasing the downstream static to upstream stagnation pressure ratio.

Moving the shock wave holding plate downstream relative to the start of the curvature in the top wall causes the secondary oblique shock wave system to disappear and the shock wave impinging on the top wall to become more oblique. Also, the pristine condition of the shock wave holding plate appears to be irrelevant to the generated shock wave structure.

The grayscale spectral energy distribution of specific pixel locations near the shock wave and lambda foot impinging on the bottom wall are considered with respect to frequency. The grayscale spectral energy distribution with respect to frequency and Strouhal number vary as the amount of venting from the exhaust plenum, the angle of the choking flap, the height of the shock wave holding plate, or the streamwise position of the shock wave holding plate are changed. Increasing ratios of local static pressure in the bottom passage to inlet stagnation pressure generally give lower total spectral energy content. This is observed when decreasing venting, decreasing the height of the shock wave holding plate, and increasing the choking flap angle. For all of these arrangements, alterations to associated grayscale spectral energy distribution variations are generally most significant for frequencies less than 10 Hz and Strouhal numbers less than approximately 0.0013.

## CHAPTER 7. RESULTS FROM 13 NOVEMBER 2017

### 7.1 Configuration

During the test on 13 November 2017, the wind tunnel test section is configured as shown within the schematic diagram in Figure 7.1. The front of the shock wave holding plate is 4.77 inches from test section's entrance. The bottom surface of the shock wave holding plate is parallel to the bottom wall of the test section. The distance between the bottom wall of the test section and the bottom surface of the shock wave holding plate is approximately 1.40 inches. The choking flap is angled at  $3.7^\circ$ . This allows equal mass flow rate in the top and bottom passages. The entrance to smallest area ratio in the top passage is estimated to be 1.10. The entrance to smallest area ratio in the bottom passage is 1.17. The air exhausts downstream of the test section by way of the exhaust ducts and plenum vents. The small vent on the exhaust plenum is fully open. The large vent on the exhaust plenum is half open giving a plenum to regulator pressure ratio of 0.342.

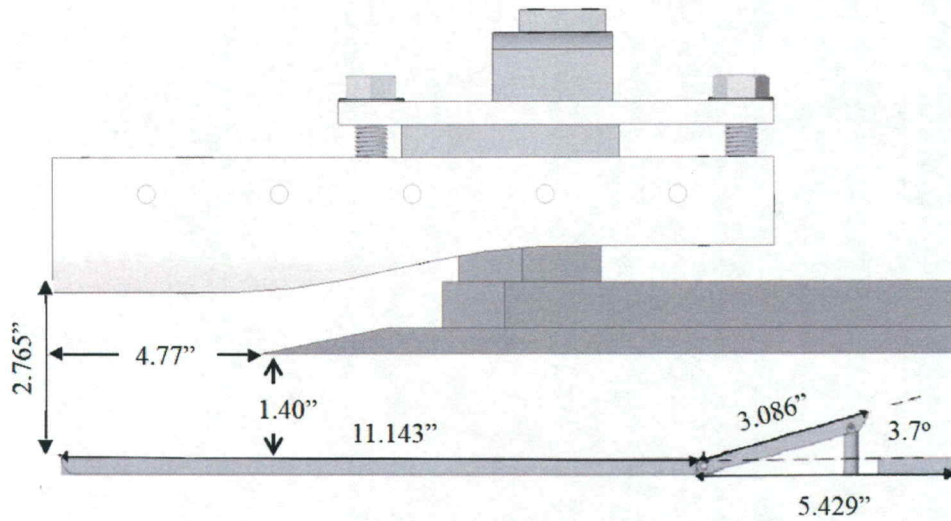


Figure 7.1: The configuration of the test section for the test on 13 November 2017

The wind tunnel test lasts approximately 8 seconds. The Phantom v711 camera records a time sequence of shadowgraph flow visualization images during the test at a rate of 5000 frames per second. The exposure time is 10 microseconds. The images are 1280 x 800 pixels in size. 15425 images are recorded, resulting in a time sequence lasting approximately 3 seconds. With a sampling frequency of 5000 frames per second, the Nyquist folding frequency is 2500 Hz. The low pass Butterworth filter is used with a cut off frequency of 2499 Hz. The frequency resolution is 0.324 Hz. Table 7.1 indicates how data at different frequencies are smoothed for the 13 November 2017 data set.

Table 7.1: Smoothing process summary associated with the test on 13 November 2017. Sampling rate is 5000 frames per second and frequency resolution is 0.3421 Hz.

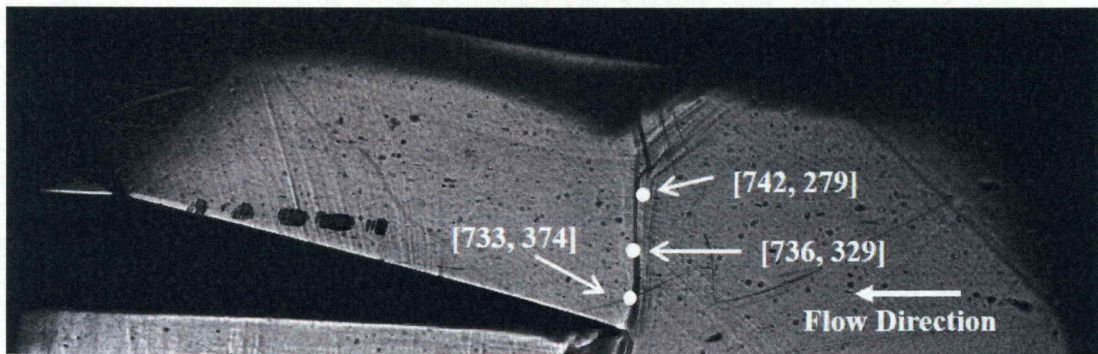
Array indices (points)	Frequency range (Hz)	Averaging and Applied Data Range
0 - 20	$0 < f \leq 6.5$	None
21-61	$6.5 < f \leq 20$	Running Average $\pm 5$ points
62 - 7328	$20 < f < 2375$	Running Average $\pm 0.05 * f / \Delta f$ points
> 7328	$2375 < f < 2500$	Replace all values with a single value determined by the average over all frequencies in this range

## 7.2 Overall Results

Flow regions, which are considered, include: the shock wave, the lambda foot, the upstream boundary layer, and the downstream boundary layer.

### 7.2.1 Shock Wave

The first region considered is associated with the shock wave. The specific pixel locations where data are analyzed are [742, 279], [736, 329], and [733, 374]. These pixel locations are denoted by white dots in Figure 7.2, relative to an instantaneous shadowgraph image.



*Figure 7.2: The locations of the analyzed pixels on the shock wave for the test on 13 November 2017.*

The results of the grayscale spectral energy distributions as functions of frequency indicate several notable frequencies. Here, large frequency content is present at frequencies lower than 4 Hz. There are also local spectral peaks at 15 Hz, 30 Hz, 38 Hz, 85 Hz, and 110 Hz. Figure 7.3 shows the grayscale spectral energy distribution with respect to frequency for each pixel location.

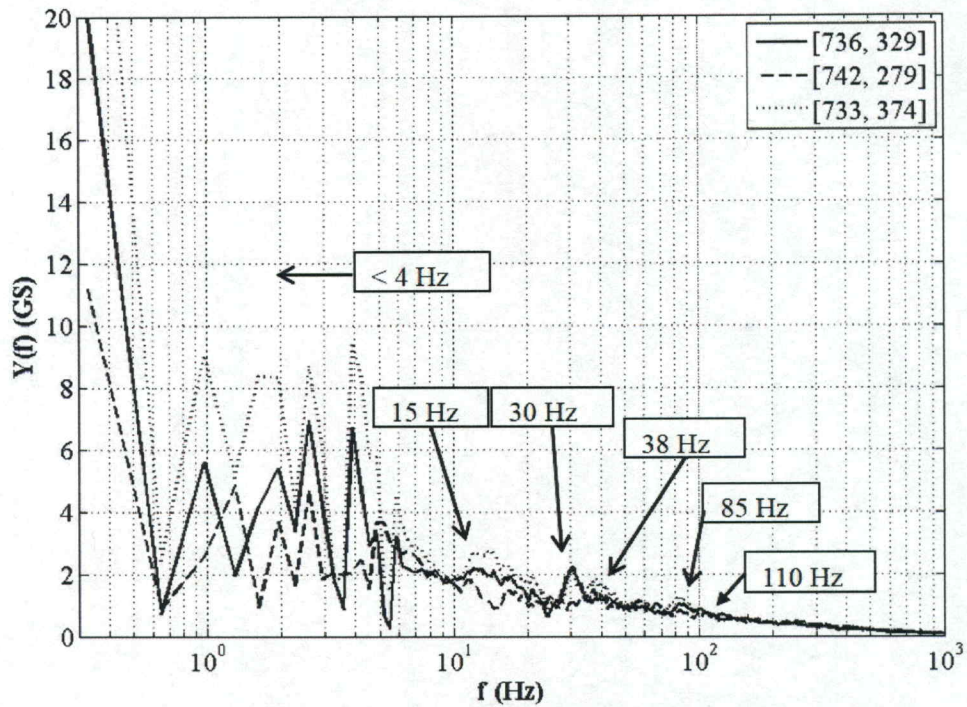


Figure 7.3: Grayscale spectral energy distribution associated the shock wave. The associated pixels' locations are shown in Figure 7.2.

The dimensionless frequency parameter, the Strouhal number, is useful for comparing test results at different flow conditions. For this test, the freestream velocity upstream of the shock is calculated to be 1410.8 feet per second with a Mach number of 1.54. The boundary layer is estimated to be 0.354 inches thick before it interacts with the shock wave. Figure 7.4 shows the grayscale spectral energy distribution with respect to Strouhal number. The Strouhal number's resolution is  $4.2E^{-5}$ . The Strouhal numbers corresponding to peaks within the grayscale values are 0.0020, 0.0039, 0.0050, 0.0111, and 0.0145, where associated frequencies are 15 Hz, 30 Hz, 38 Hz, 85 Hz, and 110 Hz, respectively.

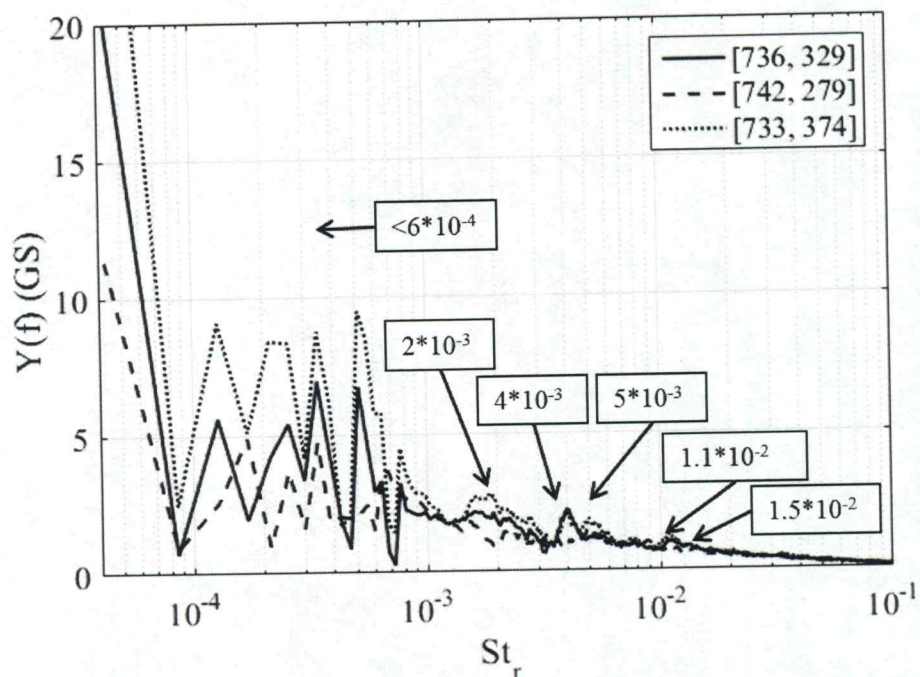


Figure 7.4: Grayscale spectral energy distribution associated with the shock wave with respect to the Strouhal number. The associated pixels' locations are shown in Figure 7.2

### 7.2.2 Lambda Foot

Three locations associated with the lambda foot are considered, at pixel locations from the time sequence data of [736, 200], [739, 226], and [744, 240]. Figure 7.5 shows the locations of these pixels, relative to an instantaneous shadowgraph image.

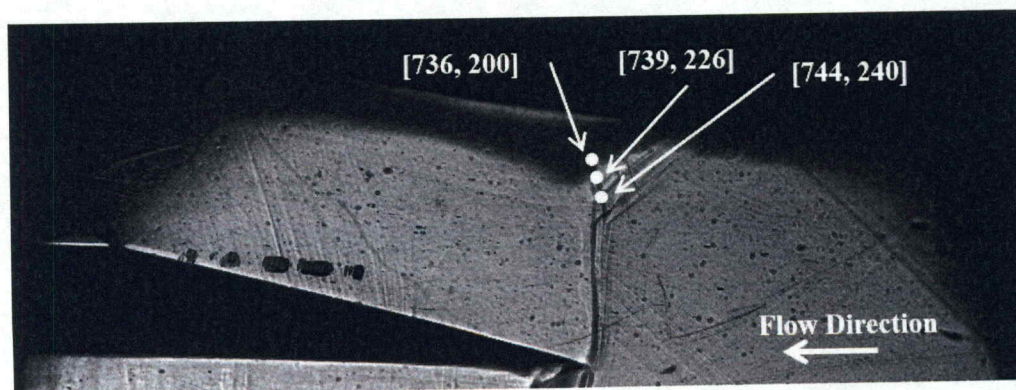


Figure 7.5: The locations of the analyzed pixels on the lambda foot from the test on 13 November 2017.

Prominent grayscale spectral energy distribution values for the lambda foot are present at different frequencies, compared to values associated with the shock wave. Multiple spectral peaks are present at frequencies less than 5 Hz. Other frequencies with prominent grayscale energy values include 7.5 Hz, 21 Hz, 42 Hz, and 65 Hz. Those frequencies correspond to Strouhal numbers of 0.0010, 0.0028, 0.0050, and 0.0085, respectively. Figure 7.6 shows the grayscale spectral energy distribution at pixel locations over which the lambda foot passes as a function of frequency, and Figure 7.7 shows grayscale spectral energy distribution as a function of Strouhal number.

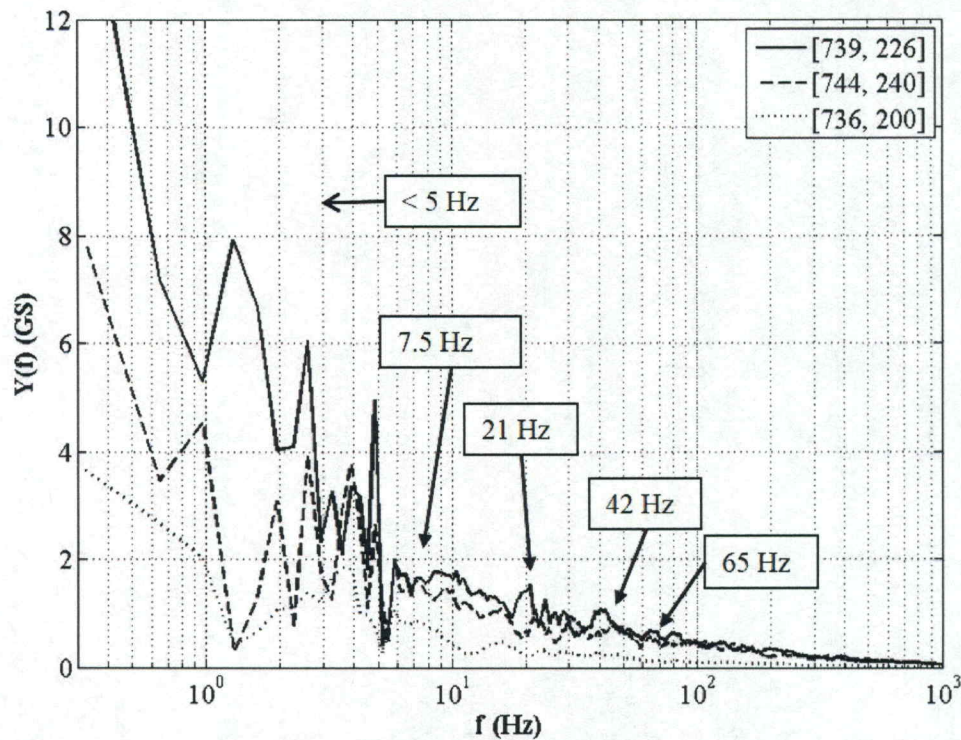


Figure 7.6: Grayscale spectral energy distribution associated with three pixel locations on the lambda foot. The associated pixels' locations are shown in Figure 7.5.



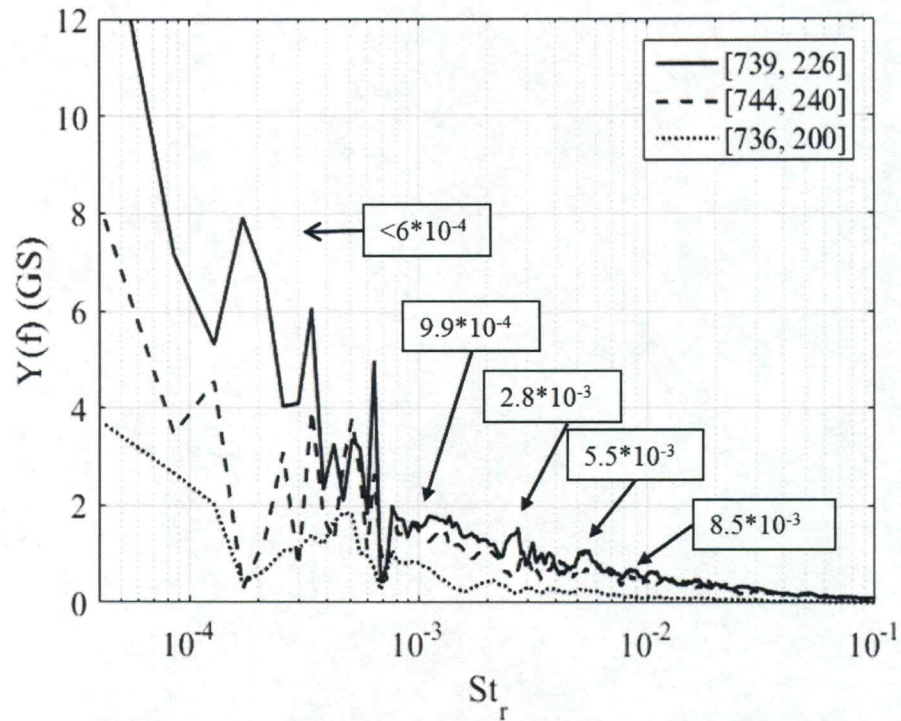


Figure 7.7: Grayscale spectral energy distribution associated with three pixel locations on the lambda foot with respect to the Strouhal number. The associated pixels' locations are shown in Figure 7.5.

### 7.2.3 Upstream Boundary Layer

Three pixel locations in the upstream boundary layer are selected. These pixel locations are [854, 189], [899, 200], and [987, 208]. They are shown relative to an instantaneous shadowgraph image in Figure 7.8.

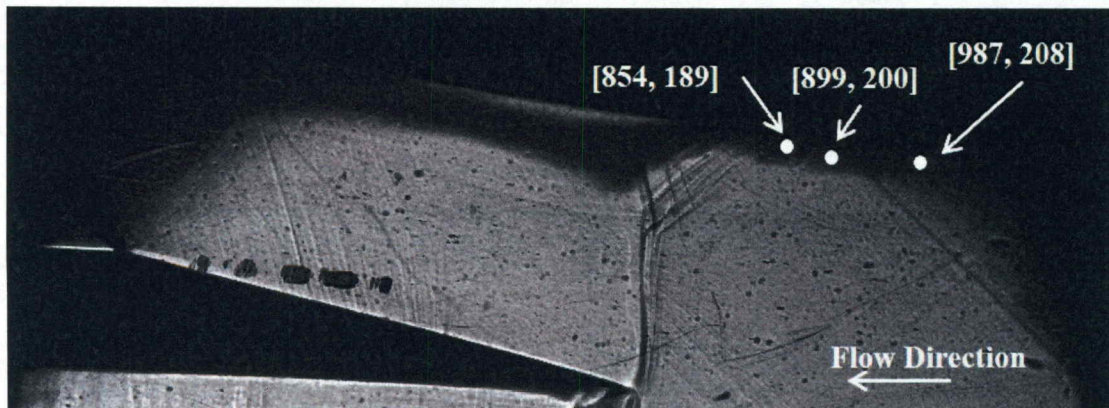


Figure 7.8: The locations of the analyzed pixels in the upstream boundary layer.

The grayscale spectral energy distribution of these pixel locations share common spectral peaks at frequencies of 7.5 Hz, 15 Hz, 30 Hz, 44 Hz, 65 Hz, and 110 Hz. The Strouhal numbers that correspond to these frequencies are 0.00010, 0.0020, 0.0039, 0.0055, 0.0085, and 0.0145, respectively. There are also several large grayscale spectral energy values for frequencies less than 5 Hz, which correspond to Strouhal numbers less than 0.0006. Figures 7.9 and 7.10 show the grayscale spectral energy distributions with respect to frequency and with respect to Strouhal number, respectively.

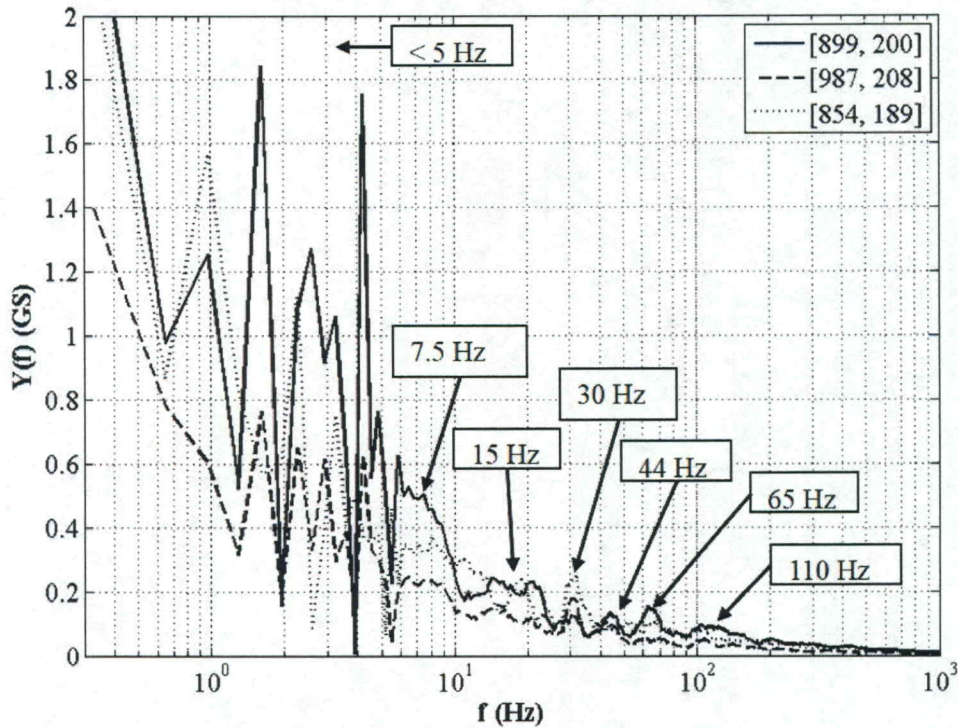


Figure 7.9: Grayscale spectral energy distribution associated with three pixel locations in the upstream boundary layer. The associated pixels' locations are shown in Figure 7.8.

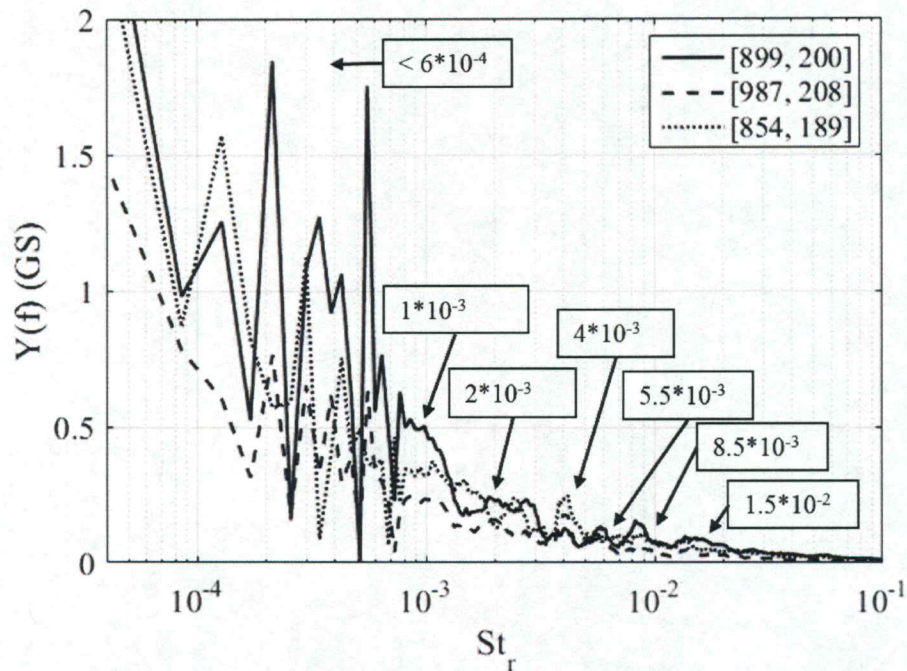


Figure 7.10: Grayscale spectral energy distribution associated with three pixel locations in the upstream boundary layer with respect to the Strouhal number. The associated pixels' locations are shown in Figure 7.8.

#### 7.2.4 Downstream Boundary Layer

Also considered is the downstream boundary layer. The pixel locations [589, 168], [651, 155], and [700, 198] are analyzed. Figure 7.11 shows the locations of these pixels, relative to an instantaneous shadowgraph image.

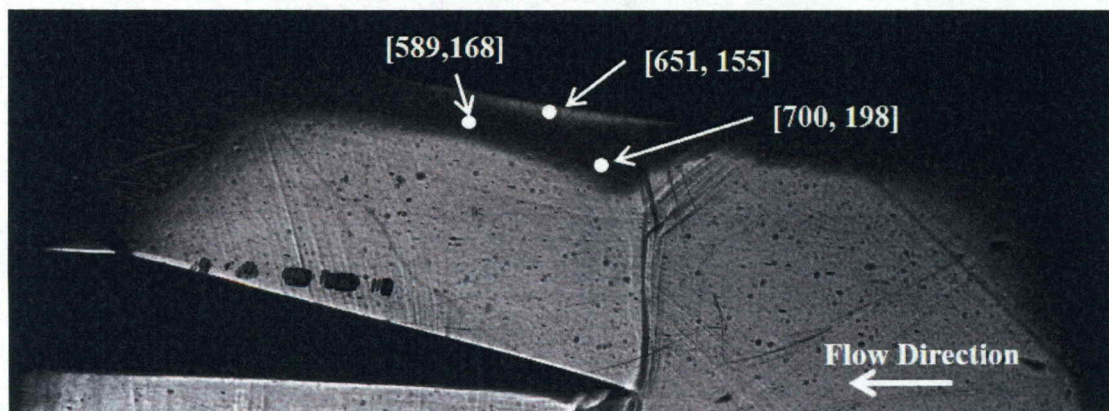


Figure 7.11: The locations of the analyzed pixels in the downstream boundary layer.

The grayscale spectral energy distributions values associated with those pixel locations show multiple peaks at frequencies less than 5 Hz, corresponding to Strouhal numbers less than 0.0006. The other prominent grayscale spectral energy peaks are present at frequencies of 7.5 Hz, 15 Hz, 30 Hz, 42 Hz, 65 Hz, and 110 Hz, which correspond to Strouhal numbers of 0.0010, 0.0020, 0.0039, 0.0055, 0.0085, and 0.0145, respectively. Figure 7.12 indicates the peaks of the grayscale spectral energy distributions with respect to frequency for the three pixel locations considered. Figure 7.13 shows the grayscale spectral energy distributions with respect to Strouhal number.

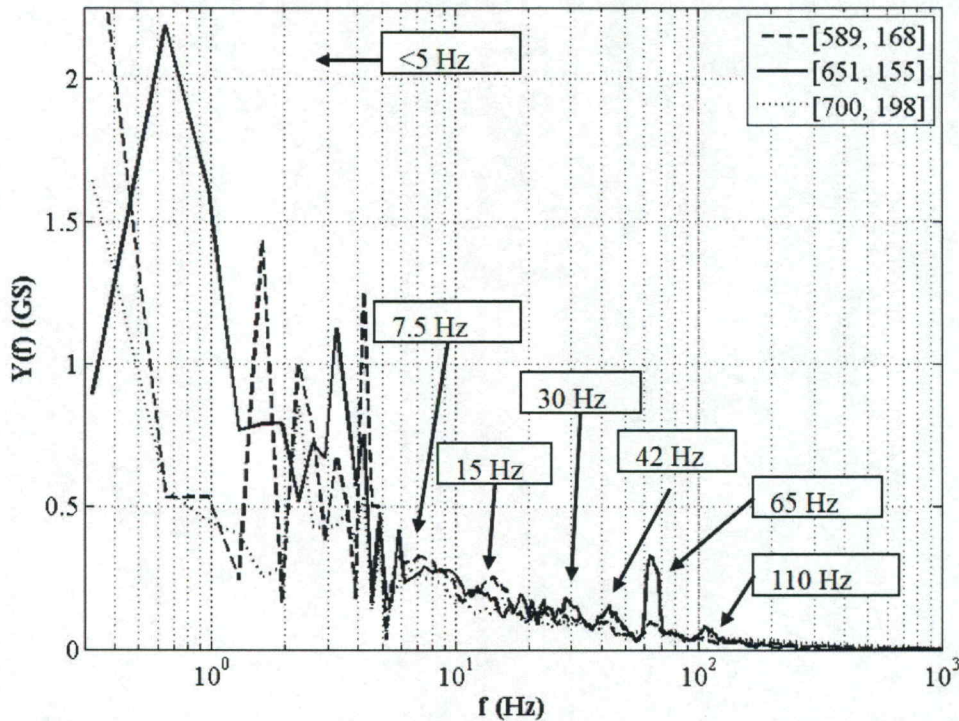


Figure 7.12: Grayscale spectral energy distributions associated with three pixel locations in the downstream boundary layer. The associated pixels' locations are shown in Figure 7.11.

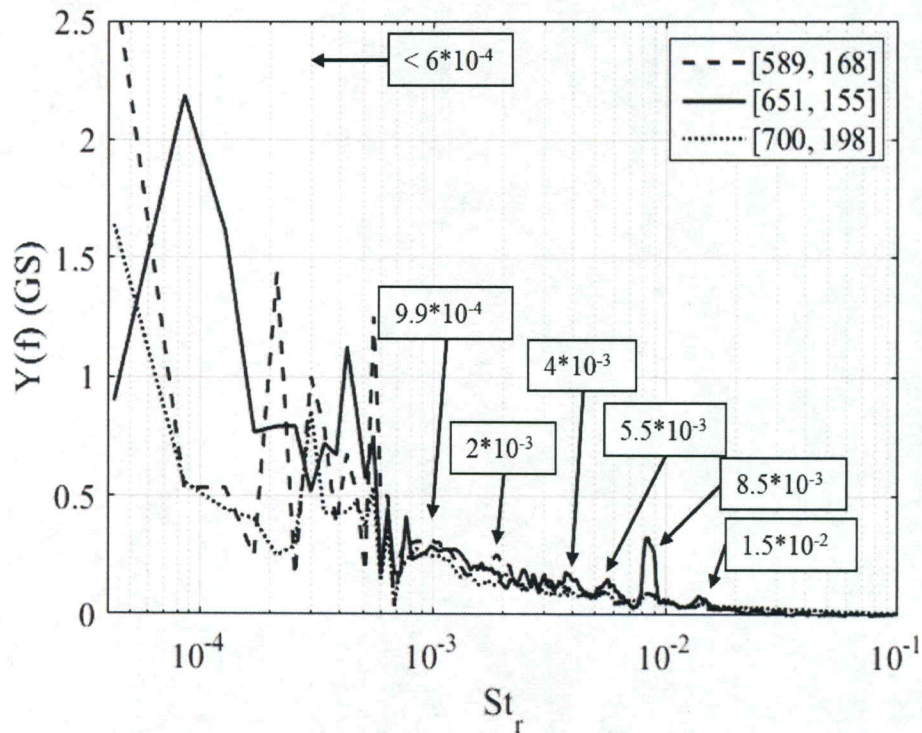


Figure 7.13: Grayscale spectral energy distributions associated with three pixel locations in the downstream boundary layer with respect to Strouhal number. The associated pixels' locations are shown in Figure 7.11.

### 7.2.5 Grayscale Spectral Energy Distribution Comparison

Characteristic grayscale spectral energy distributions are compared for each flow region. The selected pixel locations are [736, 329] for the shock wave, [739, 226] for the lambda foot, [893, 200] for the upstream boundary layer, and [589, 168] for the downstream boundary layer. These pixel locations are marked in Figure 7.14 relative to an instantaneous shadowgraph image.

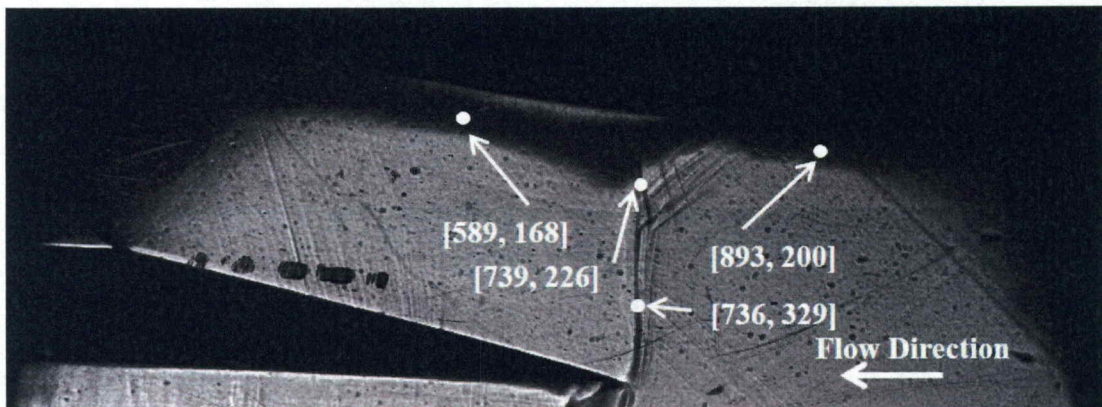


Figure 7.14: The locations of the pixels representative of the shock wave, lambda foot, upstream boundary layer, and downstream boundary layer regions.

The overall integrated spectral energy of grayscale values are compared in Table 7.2. Table 7.2 shows the spectral energy calculated from the time domain and frequency domain data. It also shows representative energy values for each of the flow regions considered. Here, the flow associated with the with the shock wave pixel location has the greatest overall integrated energy. This is expected since the shock wave is associated with the largest local density gradients of all the flow features considered. The flow associated with the lambda foot pixel location has the second greatest overall integrated energy. The flow at the pixel location associated with the upstream boundary layer has more energy than the flow at the pixel location associated with the downstream boundary layer. The energy is calculated from the time sequence array and the frequency array prior to smoothing. Note that both methods produce the same result for all four considered pixel locations shown in Figure 7.14. Associated values of white noise are presented in Table 7.3.

Table 7.2: Energy of selected pixels in each of the four flow regions considered. The energy is calculated from the time sequence data and the frequency transformed data.

Location	Pixel	$\overline{y(t)^2}$	$\frac{1}{2} * \overline{Y(f)^2}$
Shock Wave	[736, 329]	1110.6	1110.6
Lambda Foot	[739, 226]	972.5	972.5
Upstream Boundary Layer	[893, 200]	23.6	23.6
Downstream Boundary Layer	[589, 168]	13.2	13.2

Table 7.3: The value of the white noise subtracted from each of the selected pixels in the four flow regions considered.

Location	Pixel	White Noise
Shock Wave	[736, 329]	0.175
Lambda Foot	[739, 226]	0.2332
Upstream Boundary Layer	[893, 200]	0.025
Downstream Boundary Layer	[589, 168]	0.0194

The grayscale spectral energy distributions at these pixel locations are shown with respect to frequency in Figures 7.15, 7.16, 7.17, and 7.18 for the shock wave, lambda foot, upstream boundary layer, and downstream boundary layer, respectively. In each figure, important frequencies are identified. Note that the data within these figures are given in log-log coordinates whereas previous data presented in Figures 7.3, 7.4, 7.6, 7.7, 7.9, 7.10, 7.12, and 7.13 are presented using semi-log coordinates.

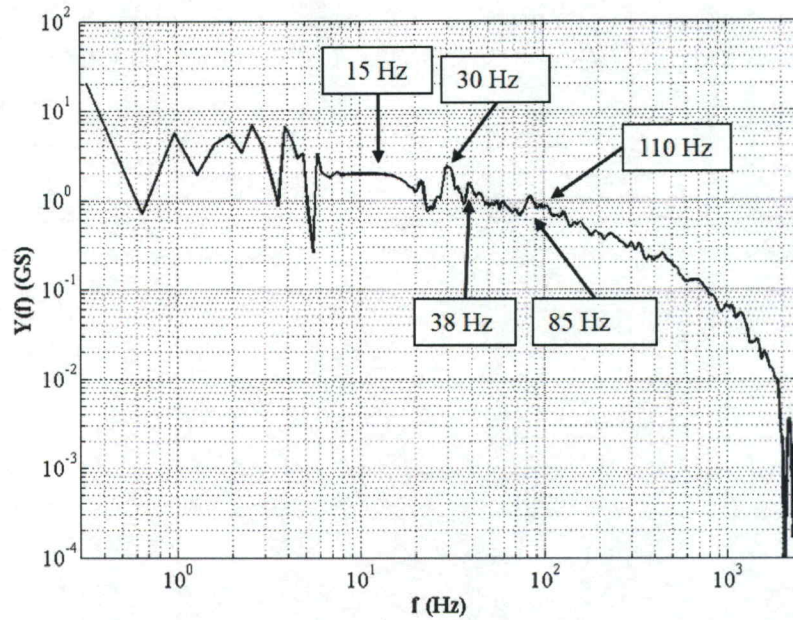


Figure 7.15: Grayscale spectral energy distribution for a location on the shock wave. The pixel is [736, 329] from the test on 13 November 2017.

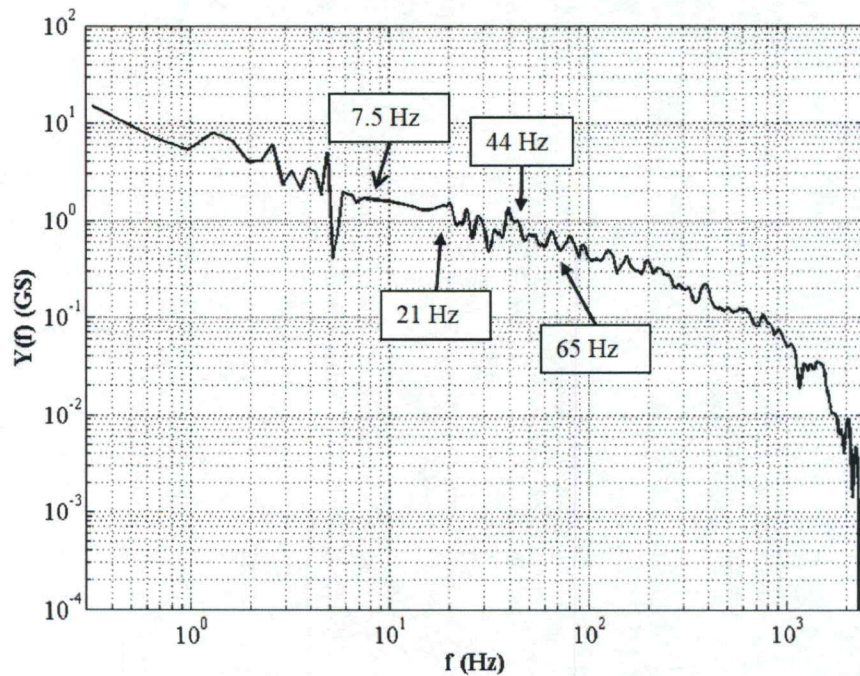


Figure 7.16: Grayscale spectral energy distribution for a location on the lambda foot. The pixel is [739, 226] from the test on 13 November 2017.



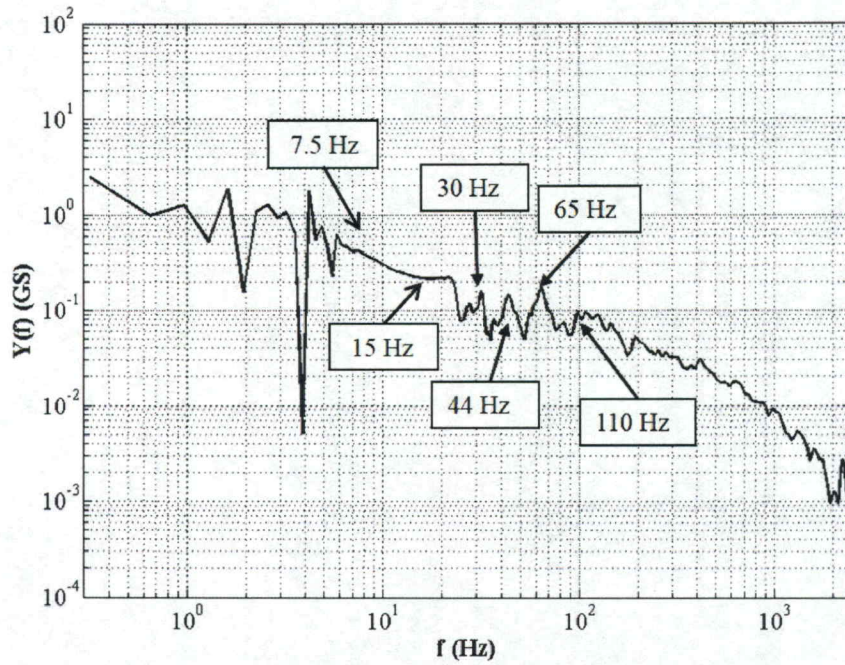


Figure 7.17: Grayscale spectral energy distribution for a location in the upstream boundary layer. The pixel is [893, 200] from the test on 13 November 2017.

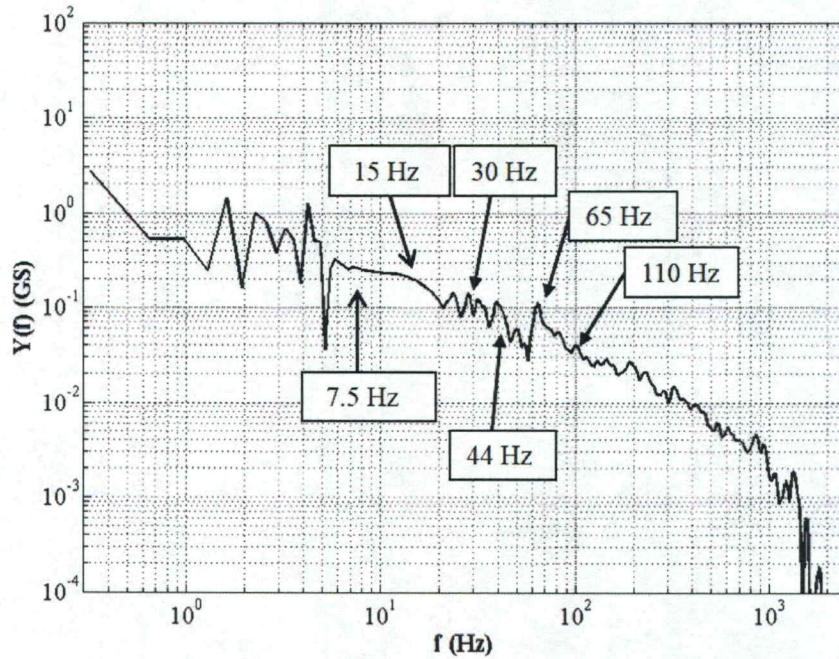


Figure 7.18: Grayscale spectral energy distribution for a location in the downstream boundary layer. The pixel is [589, 168] from the test on 13 November 2017.

Grayscale spectral energy distributions for the four flow regions are compared in Figure 7.19 for Strouhal numbers less than 0.4 and in Figure 7.20 for Strouhal numbers greater than 0.002. Note that a Strouhal number of 0.002 corresponds to a frequency of 15 Hz. Spectral content associated with the upstream boundary layer is similar to that of the downstream boundary layer. Table 7.4 shows frequencies and Strouhal numbers of spectral peaks for each region. Also note that there is a possibility that the results from this test may be affected by small amplitude vibrations in the optical system employed to obtain the shadowgraph data.

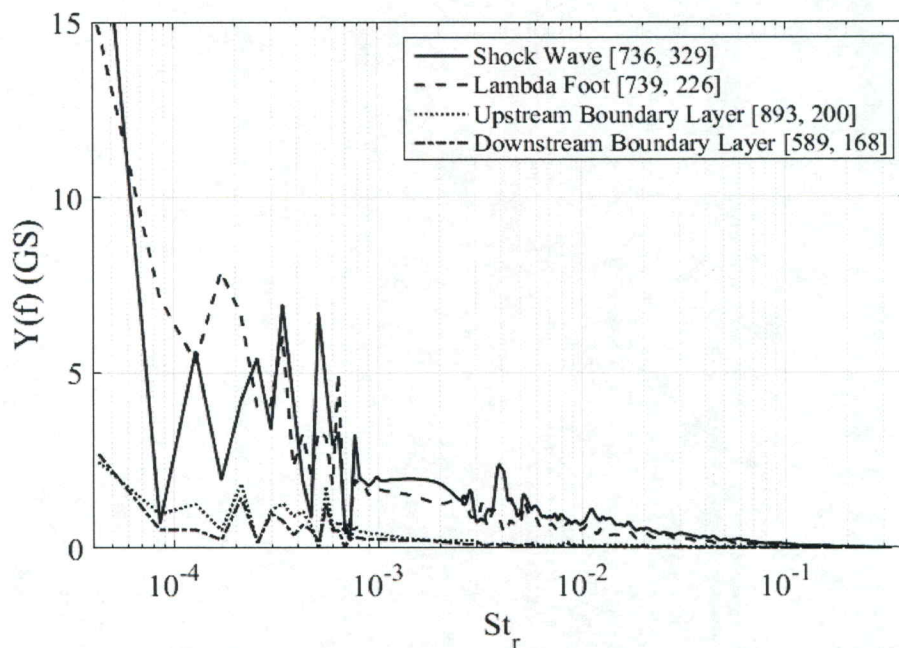


Figure 7.19: Representative grayscale spectral energy distribution from the shock wave, lambda foot, upstream boundary layer, and downstream boundary layer with respect to the Strouhal Number.

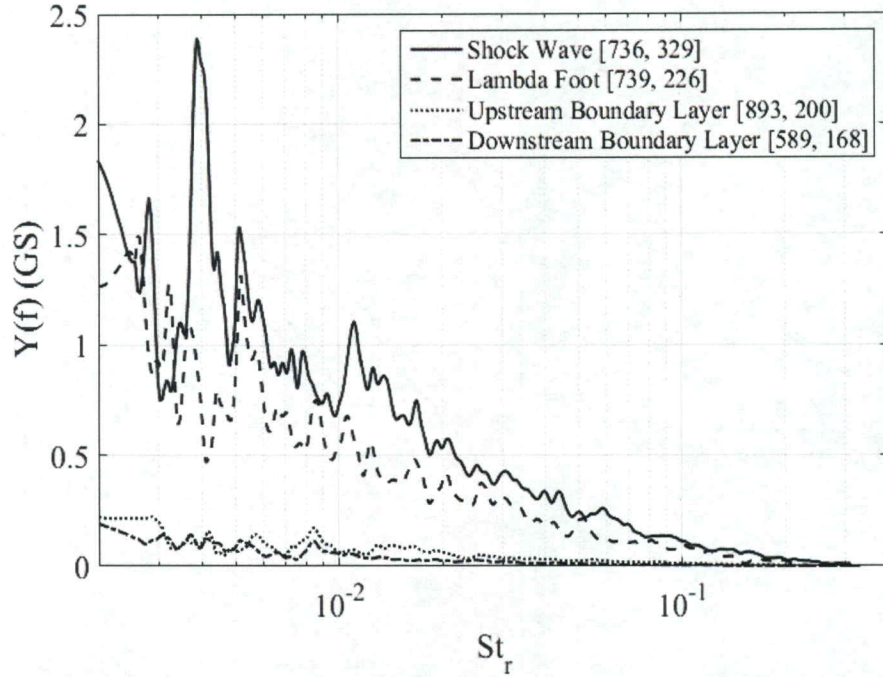


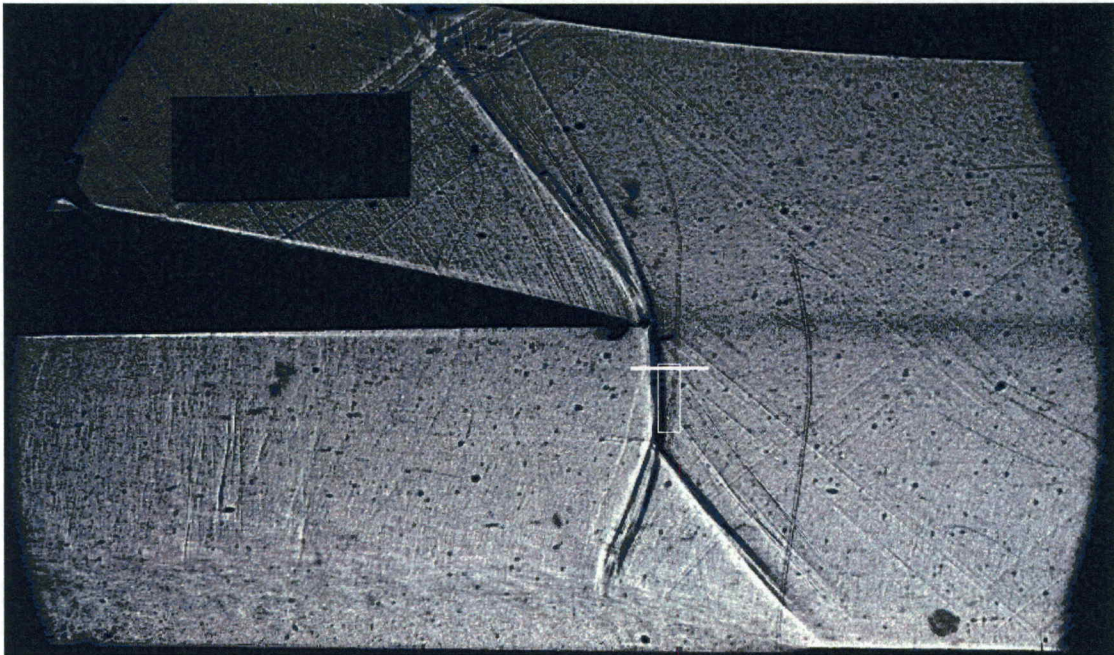
Figure 7.20: The higher frequency results of the representative grayscale spectral energy distribution in the four considered regions with respect to the Strouhal Number.

Table 7.4: The peak frequencies and Strouhal numbers for the shock wave, lambda foot, upstream boundary layer, and downstream boundary layer for the test on 13 November 2017. An "x" indicates the frequency is prominent in the corresponding region.

Frequency Hz	Strouhal Number	Shock Wave	Lambda Foot	Upstream Boundary Layer	Downstream Boundary Layer
7.5	0.00099		x	x	x
15	0.00197	x		x	x
21	0.00276		x		
30	0.00395	x		x	x
38	0.00500	x			
44	0.00552		x	x	x
65	0.00855		x	x	x
85	0.01118	x			
110	0.01447	x		x	x

## CHAPTER 8. RESULTS FROM 05 APRIL 2018

Flow visualization data are captured at an acquisition rate of 10.0 kHz during the test on 05 April 2018. A total of 21619 images are collected as established flow conditions are maintained during this test. The frequency resolution is 0.4625 Hz. The image size is 1024 x 512 pixels Figure 8.1 shows an instantaneous shadowgraph flow visualization image from the test sequence.

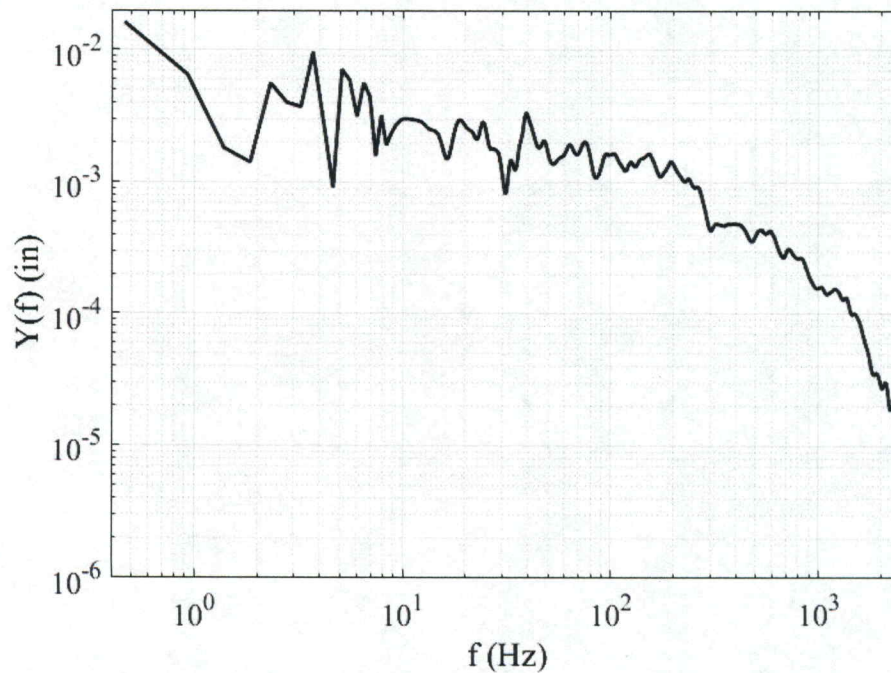


*Figure 8.1: Instantaneous shadowgraph image from the test on 05 April 2018.*

### 8.1 Shock Wave Streamwise Position Spectral Energy Result

A Lagrangian approach is used to determine the spectral energy distribution associated with the streamwise location of the normal shock wave, as is described in

Section 5.3. At a vertical location marked by the white line in Figure 8.1, the shock wave position changes approximately 0.18 inches in either direction, relative to its average position. This motion is due to unsteadiness. Note that the shock wave is positioned slightly downstream of its average position in this shadowgraph image. The resulting energy spectrum is shown in Figure 8.2. This is compared with the ensemble-averaged grayscale spectral energy distribution (for a single, stationary pixel location) near the shock wave, shown in Figure 8.3. The grayscale spectral energy distributions at five pixel locations are ensemble averaged to generate the results in Figure 8.3. The region in which these pixels are located is denoted by a white rectangle in Figure 8.1. The two plots show peaks at similar frequencies. For example, both data sets show spectral peaks at approximately 40 Hz and between 2 Hz and 9 Hz. Figures 8.2 and 8.3 also show that the spectral energy decreases significantly at frequencies greater than 200 Hz.



*Figure 8.2: Spectral energy distribution of the shock wave position relative to the average shock wave position as a function of frequency.*

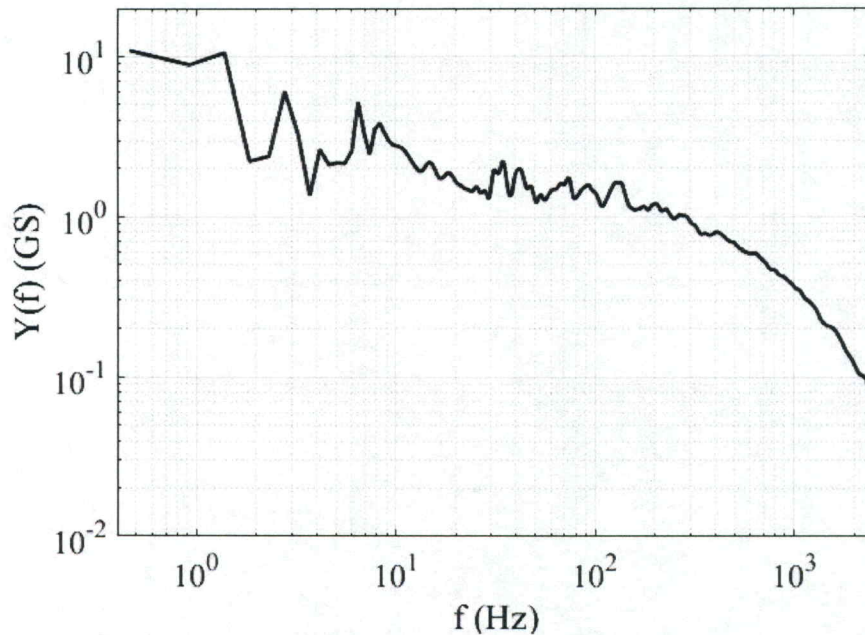


Figure 8.3: Grayscale spectral energy distribution for locations near the shock wave.

## 8.2 Grayscale Spectral Energy Results

Representative grayscale spectral energy distributions are shown with respect to frequency and Strouhal number in Figure 8.4. These data illustrate spectral variations near the shock wave, near the lambda foot, within the upstream boundary layer, and within the downstream boundary layer. Of particular interest are pronounced local peaks in frequency spectra for all four flow regions at Strouhal numbers  $St_r$  of 0.0047 to 0.0053 (or frequencies of 36 to 40 Hz), and also at  $St_r$  of 0.0144 to 0.0157 (or frequencies of 110 to 120 Hz). These Strouhal numbers are on the same order of the results of Grilli et al. [14]. Grilli et al. describe a Strouhal number which is equivalent to 0.0245 (using the present  $St_r$  definition) for a location near the foot of a normal shock wave. Evidence of correlated flow interactions is provided by spectrum local maxima, which are present at Strouhal numbers at approximately 0.00095 ( $f=7$  Hz) for the shock wave and the

upstream and downstream boundary layers, and which are present at Strouhal numbers from approximately 0.00017 to 0.00018 ( $f=1.3\text{-}1.4$  Hz) for the shock wave and the downstream boundary layer. According to Pirozzoli et al. [16], unsteadiness with Strouhal numbers less than 0.05 is associated with the flow separation region underneath the shock wave. Gamba [25] indicates that shock wave events with frequencies less than 250 Hz originate downstream of the shock wave.

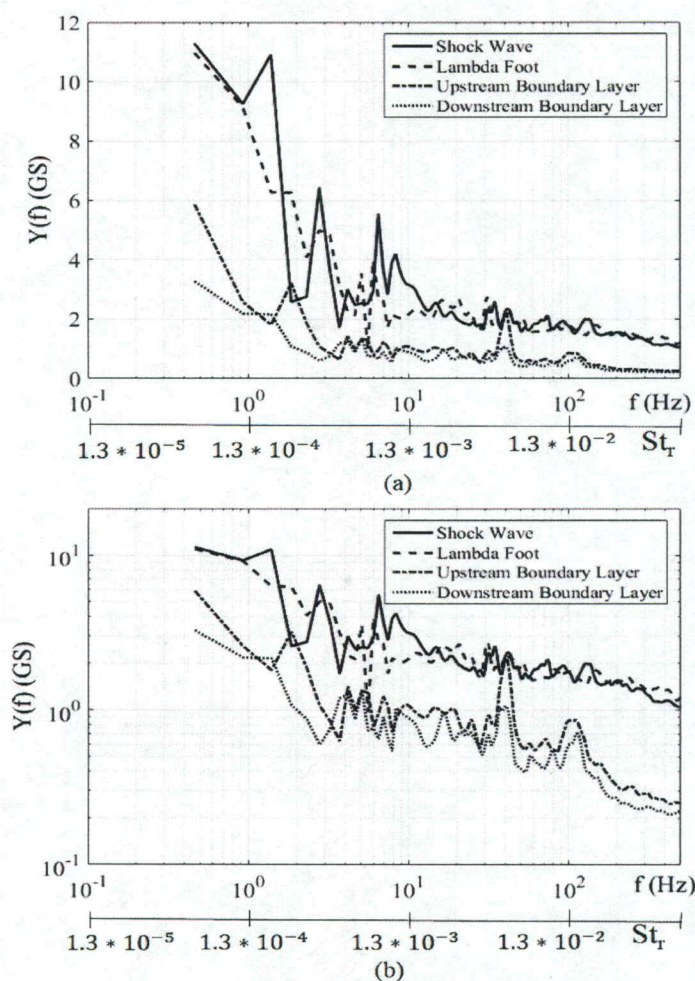


Figure 8.4: Grayscale spectral energy distribution with respect to frequency and Strouhal number shown in (a) semi-log coordinates, and (b) log-log coordinates

### 8.3 Auto-Correlation

The auto-correlation is calculated for data associated with a specific pixel location. For the present result, a pixel location on the shock wave is considered. The auto-correlation of this time sequence data is shown in Figure 8.5. Significant positive values are evident at 0.0 seconds, 1.4 seconds, and 0.75 seconds. Values for approximately 0.75 seconds indicate that the associated correlation is relatively weaker, since the auto-correlation magnitude barely exceeds the 95 percent confidence interval. Negative values of the auto-correlation indicate that the data are strongly dissimilar at time lags of 0.4 seconds and 0.9 seconds. Overall, the data in Figure 8.5 show that the grayscale time sequence data are roughly cyclical, with the most pronounced period equal to approximately 1.4 seconds.

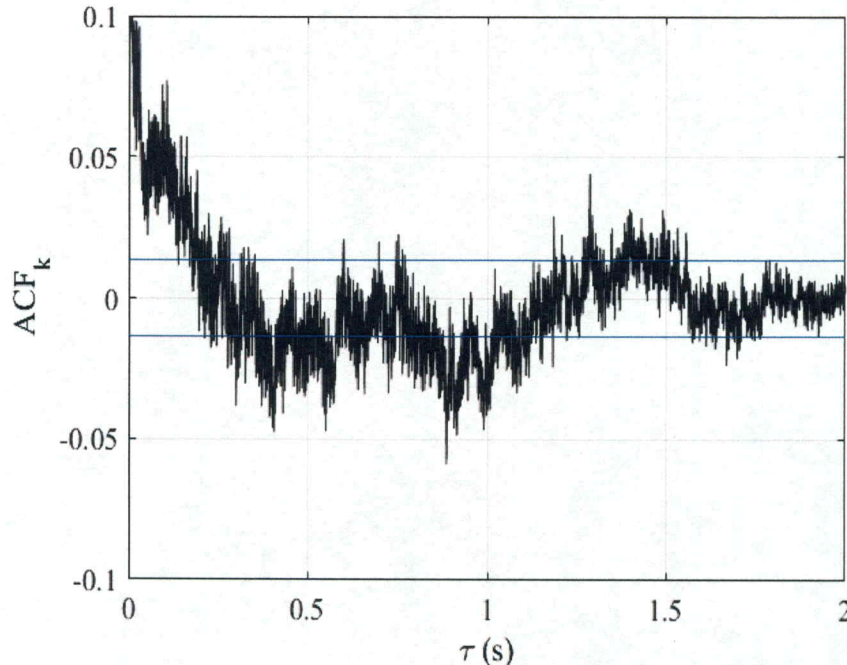


Figure 8.5: A single point auto-correlation as time varies. This utilizes data from a single pixel near the shock wave. The blue lines indicate a 95 percent confidence interval, relative to the zero value.

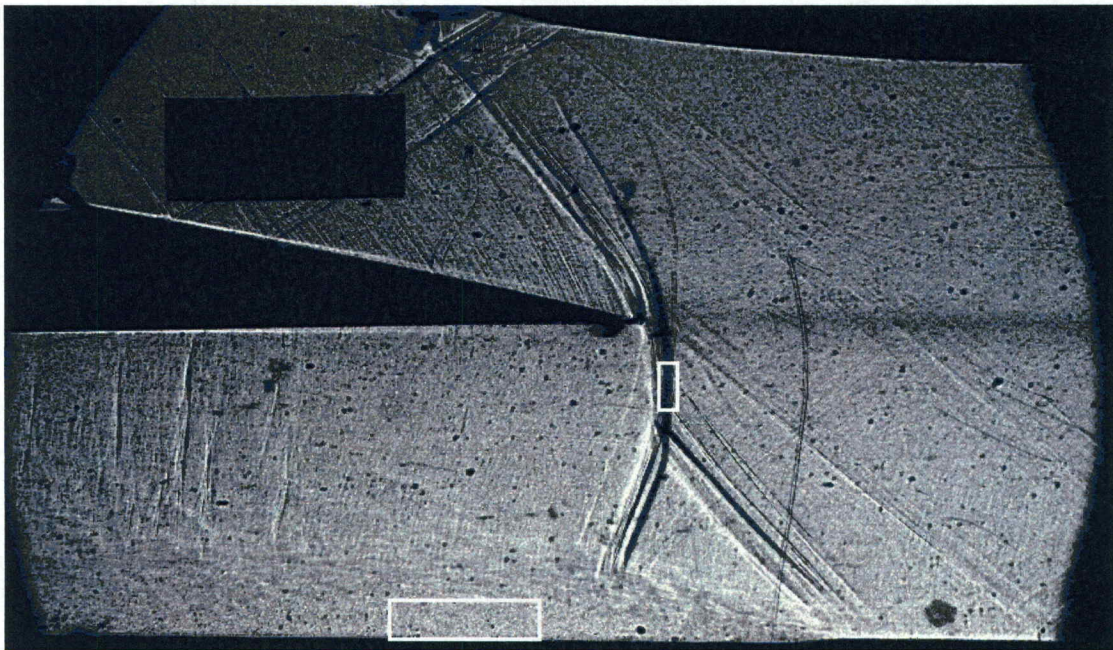


## 8.4 Correlations Function Variations Between Regions

The unsteadiness detected in various regions are correlated using the procedures described in Sections 5.4.2 and 5.4.3. Respective coherence and time lag variations are determined between data associated with the shock wave and the downstream boundary layer, and between the shock wave and the upstream boundary layer. Coherence variations between grayscale data associated with the shock wave and the lambda foot are also determined.

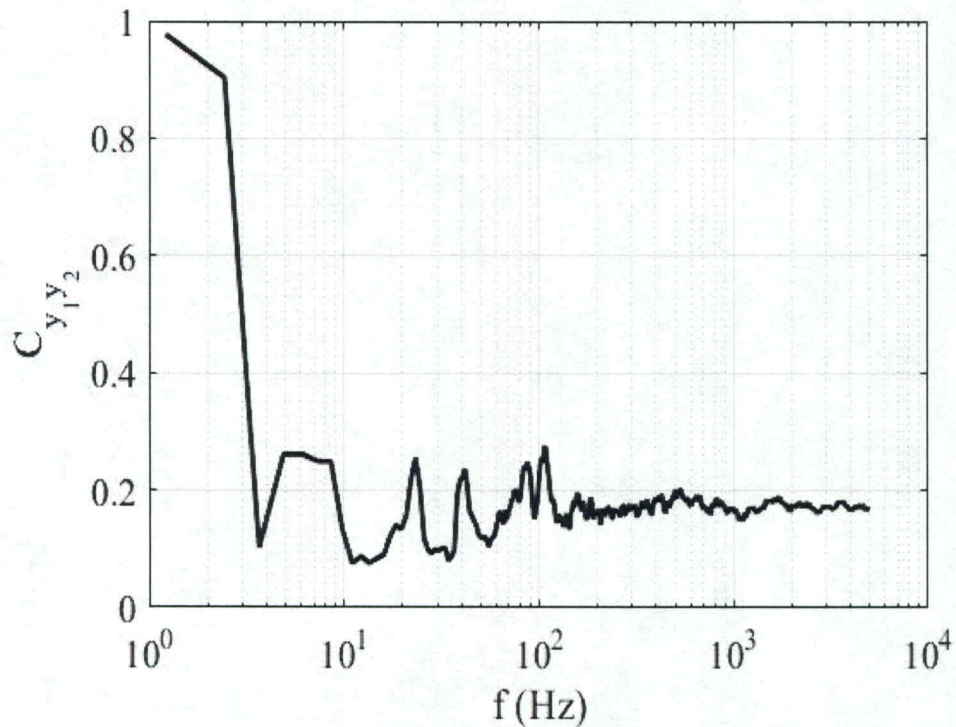
### 8.4.1 Shock Wave and Downstream Boundary Layer

Correlations exist between grayscale data associated with the shock wave and downstream boundary layer regions. The regions containing the pixel locations that are analyzed are shown by white rectangles in Figure 8.6. Figure 8.7 shows the magnitude



*Figure 8.6: Rectangles mark the locations of the pixels in the downstream boundary layer and on the shock wave associated with the data shown in Figures 8.7 and 8.8.*

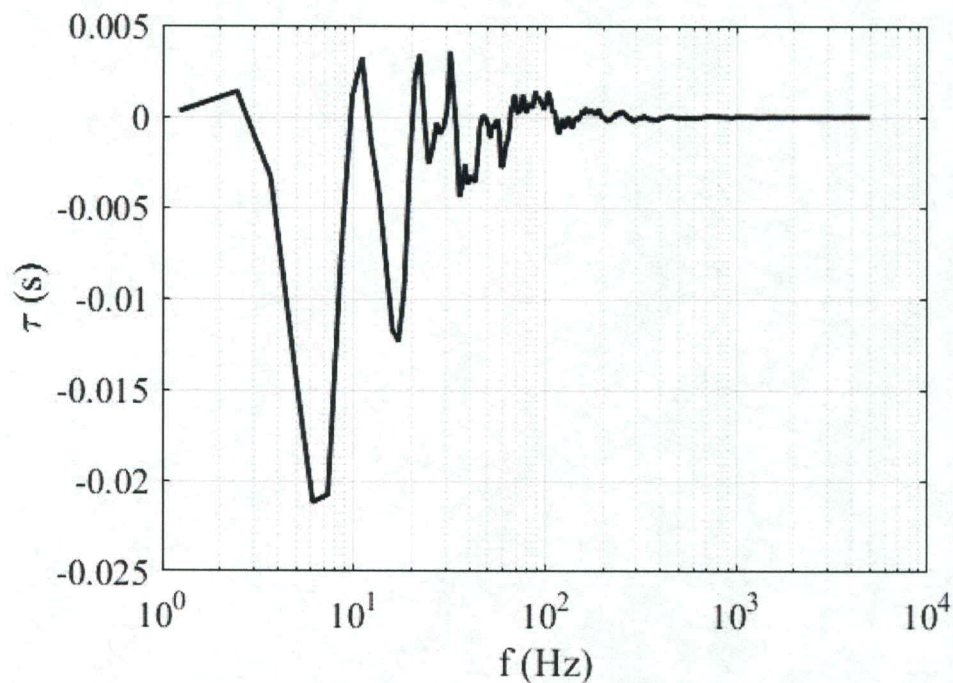
squared coherence of the time sequence grayscale signals in these two regions with respect to frequency. Associated data values evidence significant coherence between the shock wave and downstream boundary layer regions at frequencies of approximately 6 Hz, 20 Hz, 40 Hz, and 100 Hz, which correspond to Strouhal numbers of 0.00079, 0.00263, 0.00526, and 0.0132. Note that the Hanning windowing creates some fluctuations in the results at high frequencies, which are not representative of true coherence.



*Figure 8.7: Magnitude squared coherence of data associated with pixel locations near the shock wave and in the downstream boundary layer.*

The time lag values from grayscale flow visualization results are shown in Figure 8.8. Perturbations of approximately 20 Hz and 100 Hz in the downstream boundary layer occur prior to the same frequency events in the shock wave. This is determined because the values of the time lag are positive for both 20 Hz and 100 Hz. At

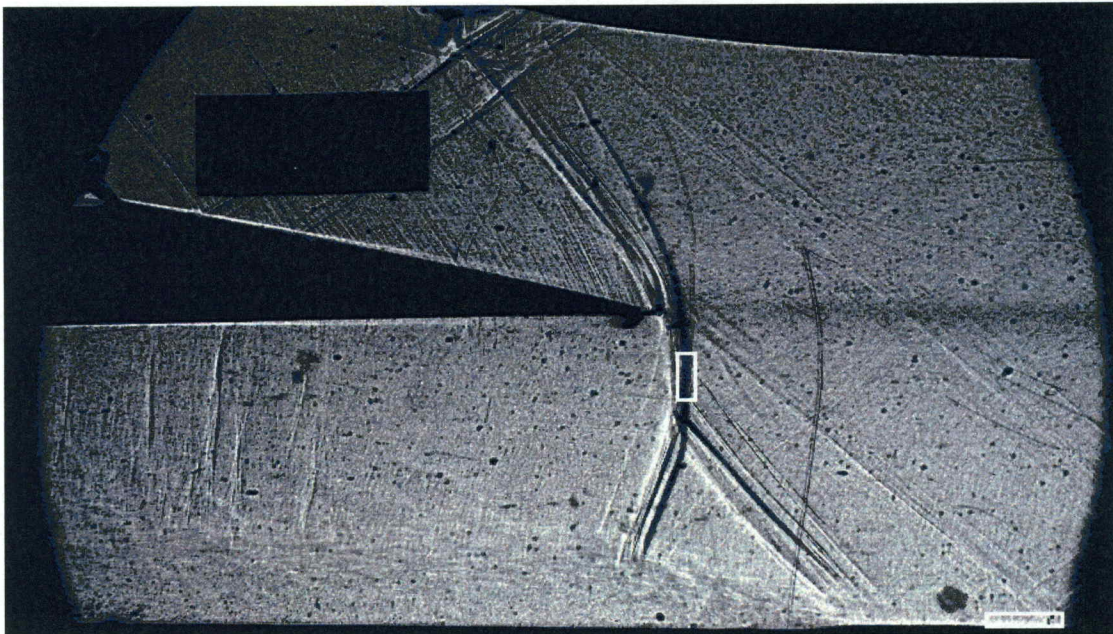
100 Hz, perturbations in the downstream boundary layer occur 1 ms before they do in the shock wave. However, for events at frequencies between 3 Hz and 20 Hz, and at approximately 40 Hz, the time lag is negative, indicating that the perturbations in the shock wave occur prior to the ones in the downstream boundary layer. Note that all of these time lags are approximately an order of magnitude longer than the time lags associated with the estimated advection speed of the fluid.



*Figure 8.8: Time lag between unsteadiness in the downstream boundary layer and the shock wave. Positive lags indicate the signal in the boundary layer comes first.*

#### **8.4.2 Shock Wave and Upstream Boundary Layer**

The magnitude squared coherence is also determined for data associated with pixel locations in the upstream boundary layer and on the shock wave. The regions containing the associated pixel locations are denoted by white rectangles in Figure 8.9.



*Figure 8.9: Rectangles mark the locations of the pixels in the upstream boundary layer and on the shock wave associated with data shown in Figures 8.10 and 8.11.*

Figure 8.10 shows that magnitude squared coherence between data in the shock wave and the upstream boundary layer exhibit peaks near 6 Hz, 40 Hz and 100 Hz, or Strouhal numbers of 0.00079, 0.00526 and 0.0132. Time lag values, shown in Figure 8.11 with respect to frequency, indicate that perturbations at both 100 Hz and 40 Hz occur in the shock wave prior to occurring within the upstream boundary layer. At frequencies less than 20 Hz, perturbations in the upstream boundary layer occur prior to those associated with the shock wave.

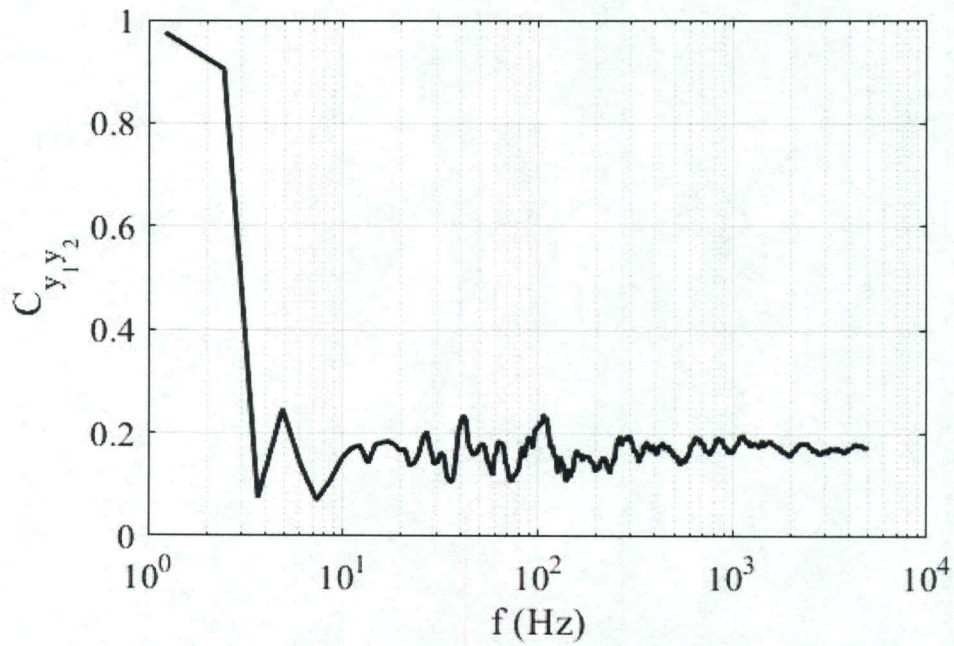


Figure 8.10: Magnitude squared coherence between grayscale signals in the upstream boundary layer and on the shock wave.

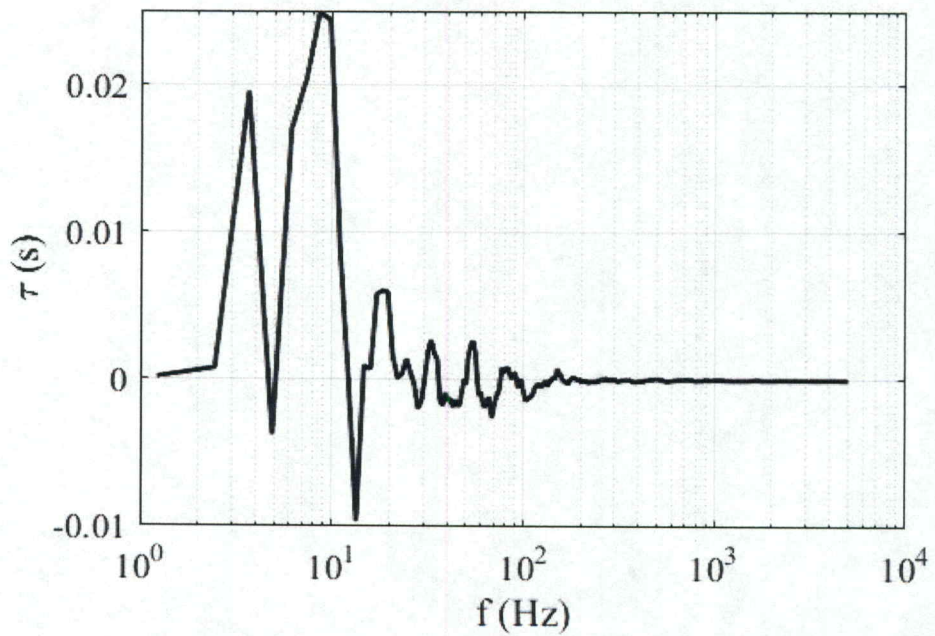
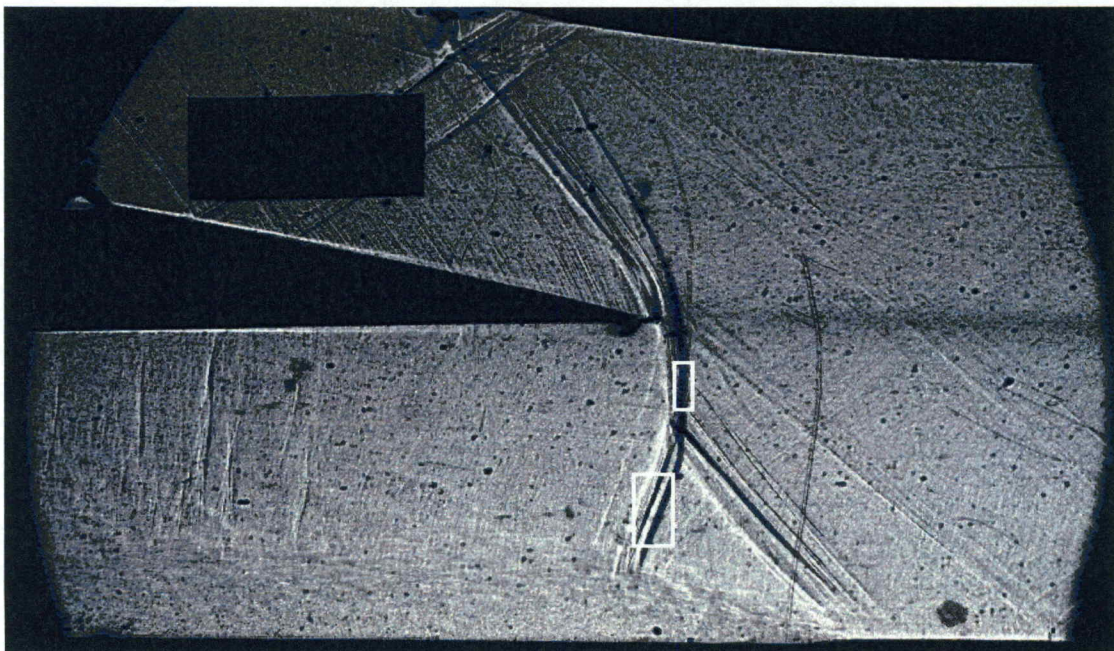


Figure 8.11: Time lag between perturbations in the upstream boundary layer and near the shock wave. Positive lags indicate that the signal in the boundary layer comes first.

Overall, the results presented show that perturbations at 100 Hz are detected first in the downstream boundary layer, then the shock wave, then the upstream boundary layer. At 40 Hz, perturbations originate near the shock wave and propagate both upstream and downstream. At frequencies less than 20 Hz, the unsteadiness originates upstream, as it is detected first in the upstream boundary layer, then the shock wave, then the downstream boundary layer. Perturbations at 20 Hz are only detected between the shock wave and the downstream boundary layer, and they seem to occur in the downstream boundary layer first.

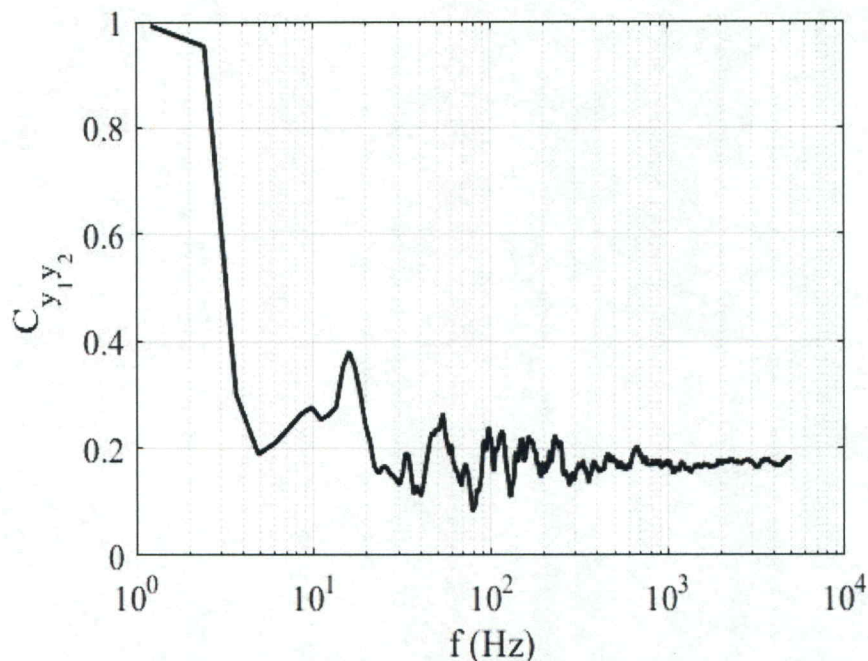
#### 8.4.3 Shock Wave and Lambda Foot

The data associated with pixel locations on the shock wave are correlated with data associated with the lambda foot. The regions containing the pixel locations on the shock wave and lambda foot are shown as white rectangles in Figure 8.12. Local maxima



*Figure 8.12: Rectangles mark the locations of the pixels on the lambda foot and on the shock wave associated with data shown in Figures 8.10 and 8.11.*

of associated magnitude squared coherence are evident in Figure 8.13 at approximately 6 Hz, 50 Hz, 100 Hz, 150 Hz, 225 Hz, and 650 Hz. The associated Strouhal numbers are 0.00079, 0.00658, 0.0132, 0.0197, 0.0296, and 0.0855, respectively.



*Figure 8.13: Magnitude squared coherence as a function of frequency of grayscale time sequence data associated with the shock wave and the lambda foot*

Time lag values between the signals in the shock wave and the lambda foot are presented in Figure 8.14 as they vary with frequency. In general, the signal from the shock wave comes prior to the signal associated with the lambda foot. However, unsteadiness in the lambda foot comes before unsteadiness in the shock wave at frequencies of 20 Hz, 30 Hz, and 150 Hz. In this case, positive time lags indicate the signals in the lambda foot are first and negative time lags indicate the signals in the shock wave are first. Note that this result is related to the order in which associated data are input into the “cpsd” function in MATLAB.

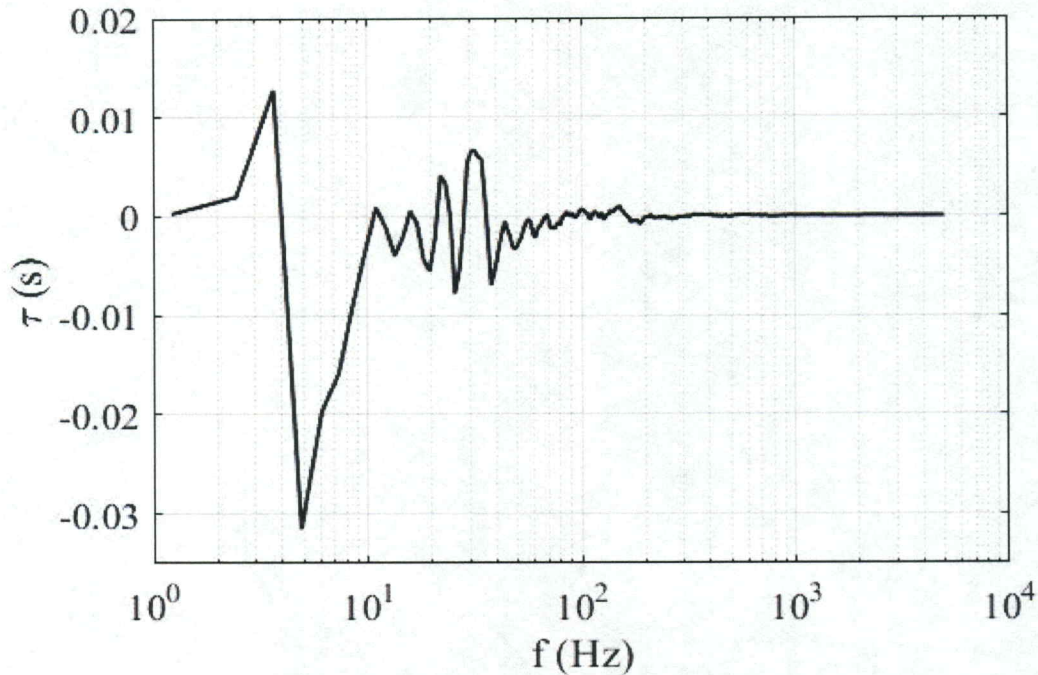
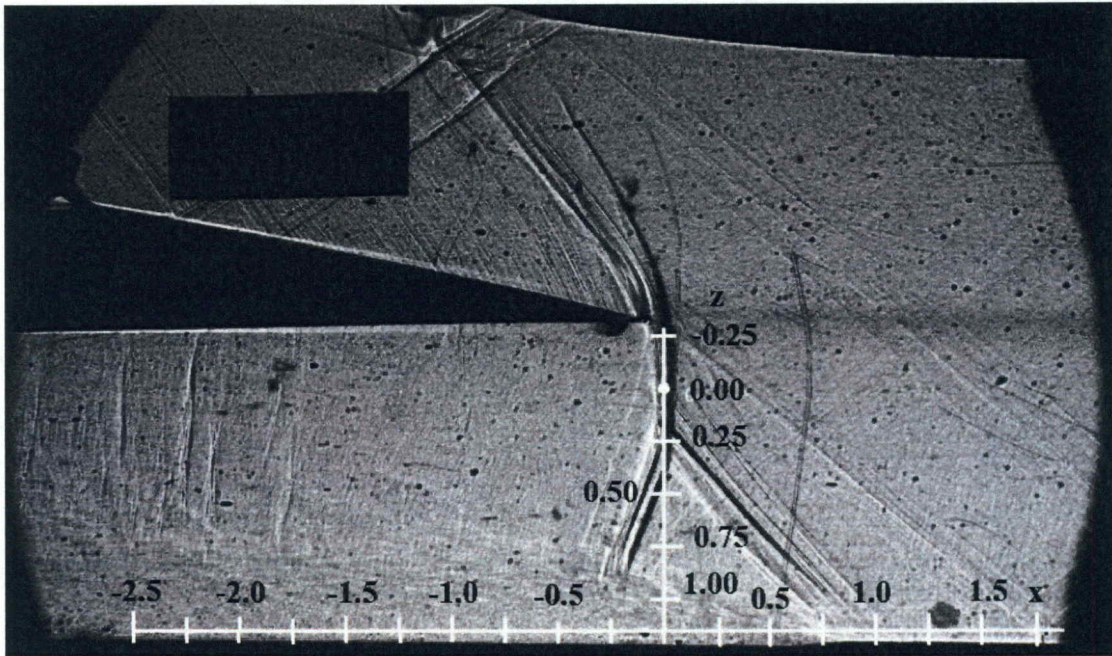


Figure 8.14: Time lag between perturbations near the lambda foot and near the shock wave. Positive lags indicate that the signal associated with the lambda foot comes first.

### 8.5 Correlation Function and Time Lag Results to Illustrate Spatial Variations

The magnitude squared coherence and time lag at certain frequencies are determined for one location, relative to a range of other spatial locations. The locations are represented by the long horizontal and vertical white lines within the flow visualization image of Figure 8.15. Note that coordinate scale locations along these lines are included. The magnitude squared coherence and time lag are calculated between these locations and a location on the shock wave, which is indicated by a white dot within Figure 8.15. The origin is chosen to be the pixel location on the shock wave. The other pixel locations are measured relative to that location.





*Figure 8.15: The spatial locations where the magnitude squared coherence and time lag are determined and analyzed at specific frequencies. Coordinate axes are in inches.*

The magnitude squared coherence and the time lag at 20 Hz, 40 Hz, and 100 Hz for the data associated with the pixel locations along the horizontal line and the shock wave pixel location are presented in Figure 8.16. Figures 8.16 (a) (b) and (c) show results for frequencies of 20 Hz, 40 Hz, and 100 Hz, respectively. For perturbations at a frequency of 20 Hz, the strongest coherence exists between the data associated with the shock wave pixel location and a pixel location in the boundary layer 0.25 inches upstream of the shock wave. This is in a location within the lambda foot region, as is shown in Figure 8.15. At this location, the signal occurs in the boundary layer prior to the shock wave. Perturbations occurring at 40 Hz have the most coherence with the shock wave at a location 0.75 inches upstream of the main shock wave. This location is at the base of the

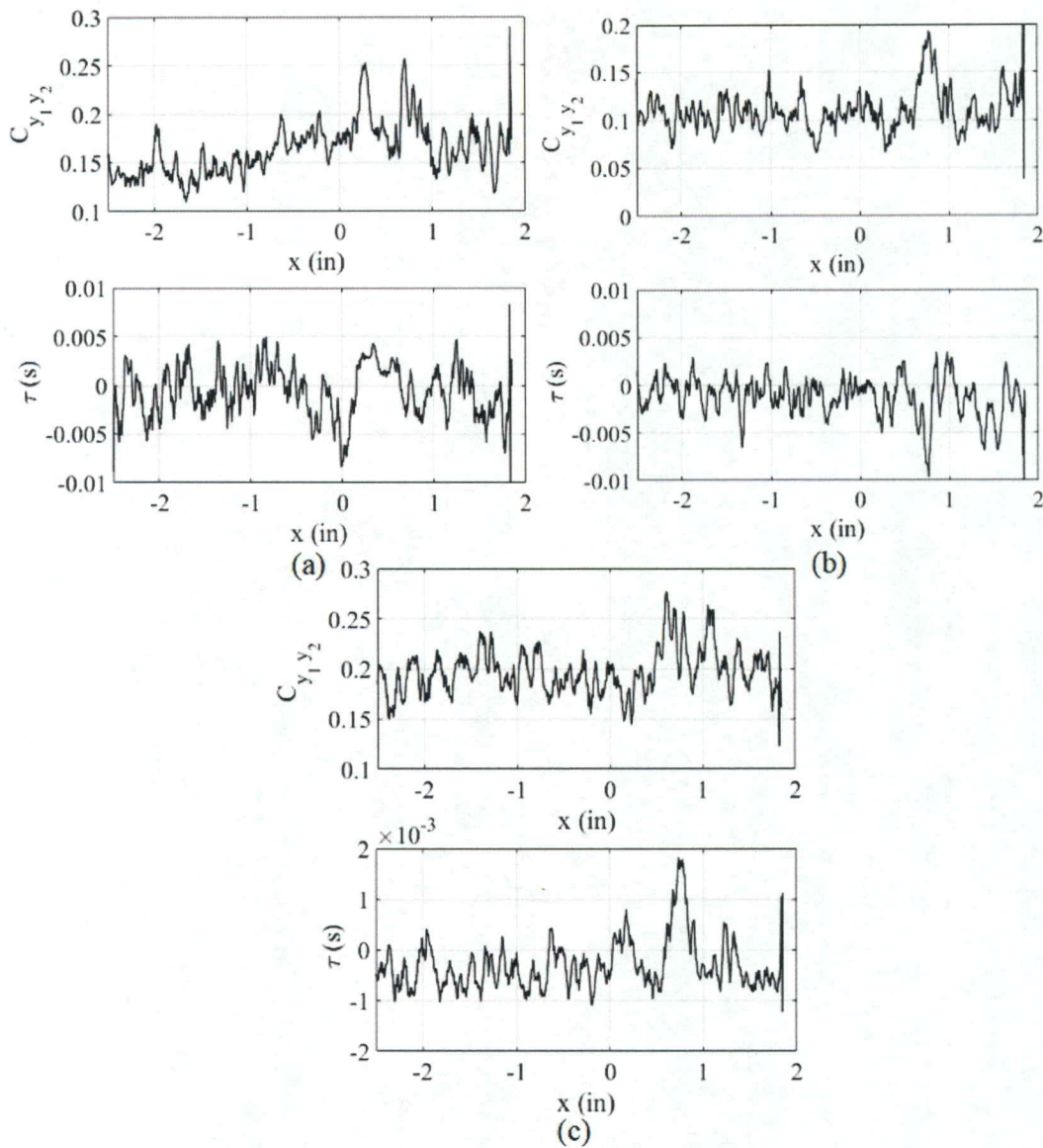


Figure 8.16: The magnitude squared coherence and time lag at frequencies of (a) 20 Hz, (b) 40 Hz, and (c) 100 Hz for  $y_1$  along a line in the boundary layer and  $y_2$  a pixel on the shock wave. Positive values of time lag indicate the boundary layer perturbation comes first.

upstream oblique shock wave associated with the shock wave boundary layer interaction.

The unsteadiness in the normal shock wave at this frequency occurs before the unsteadiness at the base of the upstream shock wave. At this frequency, such behavior indicates that perturbations in the upstream shock wave foot lag behind the shock wave.

At 100 Hz, the coherence is again greatest 0.75 inches in front of the shock wave. However, at this frequency, the signal in the upstream shock wave foot leads the shock wave.

Magnitude squared coherence and magnitudes of time lag between the same shock wave pixel location and the pixel locations along the vertical line on the shock wave are given in Figure 8.17. Figures 8.17 (a), (b), and (c) show these results for frequencies of 20 Hz, 40 Hz, and 100 Hz, respectively. All three plots show a magnitude squared coherence of 1.0 and a time lag of 0 seconds at the location where  $y_1$  is the same as  $y_2$ . This is because any signal is completely coherent with itself. More interestingly, for a frequency of 20 Hz, there is a peak in the coherence at a location 0.4 inches beneath the reference location on the shock wave ( $y_2$ ). This is just beneath the location where the oblique shock wave, normal shock wave, and lambda foot join (also referred to as the triple point), as shown in Figure 8.15. For a frequency of 40 Hz, a peak in the coherence is evident approximately 0.5 in beneath the location of  $y_2$ . A frequency of 100 Hz has increased coherence 0.2 inches beneath the location of  $y_2$ . This location is within the shock wave.

Associated time lag results are inconclusive since values are either near zero or show large amounts of data scatter. Overall, the results indicate that very little time lag is generally present within the shock wave. At 100 Hz, the signal from locations beneath the shock wave come after the signal associated with the original shock wave pixel location. Time lag values at frequencies of 20 Hz and 40 Hz vary significantly with spatial location beneath the shock wave. For the locations where notable time lags are present, there is little coherence.

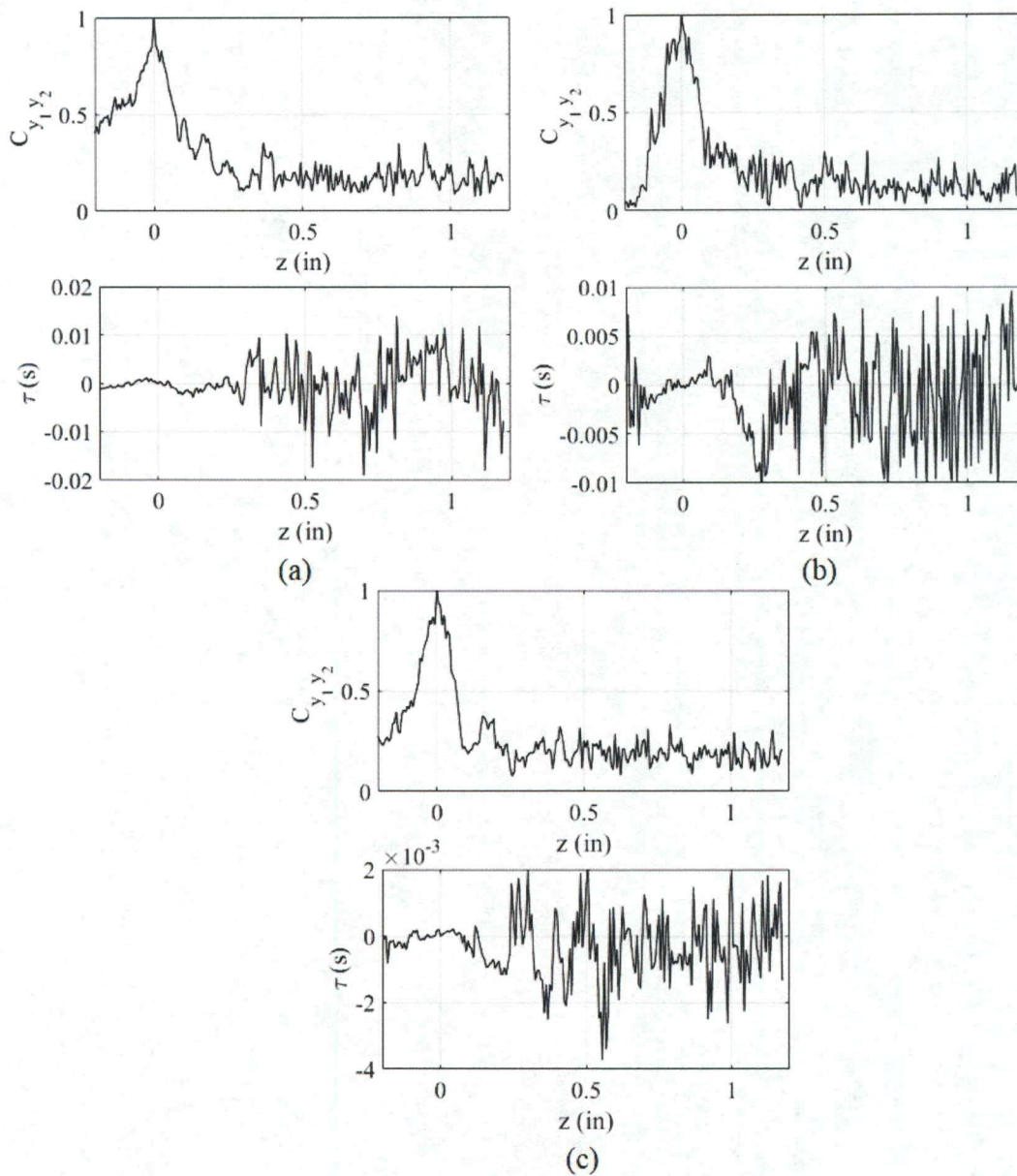


Figure 8.17: The magnitude squared coherence and time lag at frequencies of (a) 20 Hz, (b) 40 Hz, and (c) 100 Hz where  $y_1$  is located on a line along the shock wave and  $y_2$  is a pixel on the shock wave. Positive values of time lag indicate perturbations at the location along the line comes first.

## CHAPTER 9. SUMMARY AND CONCLUSIONS

Shock wave boundary layer interactions occur in many aerospace applications. Some examples include ramjet isolator ducts, turbine blade tip gaps, and transonic wings. However, low frequency unsteadiness associated with shock wave boundary layer interactions is not well understood. Different studies conclude different and contradicting results. Some results indicate that shock wave unsteadiness originates from the turbulence in the upstream boundary layer. Other results indicate that a separation region formed as part of the shock wave boundary layer interaction generates the unsteadiness. Other studies indicate that both the upstream and downstream sources are responsible for shock wave unsteadiness. The current investigation is aimed at development of a supersonic wind tunnel test section for normal shock wave boundary layer interaction studies, as well as consideration of unsteady flow characteristics and structure.

The supersonic wind tunnel facility includes high and low-pressure systems to store and regulate dried air. The dried air accelerates through a converging diverging nozzle to reach a Mach number of approximately 1.54 at the entrance to the test section. The test section is made from a flat bottom wall and a diverging top wall, and includes a shock wave holding plate that separates the flow into top and bottom flow passages. A choking flap is located in the downstream portion of the bottom passage. The present test section arrangement is similar to that proposed by Ogawa and Babinsky [1]. Once the flow exits the test section, it passes through an exhaust plenum and then exhausts to the

atmosphere. Pressures are measured throughout the supersonic wind tunnel, and a shadowgraph optical system is employed to visualize shock wave structure within the test section. Shadowgraph flow visualization data are analyzed to determine shock wave structure and unsteadiness characteristics, including grayscale spectral energy variations with frequency, as well as coherence and time lag properties associated with perturbations between different flow regions.

Effects of test section configuration on shock wave structure and unsteadiness are considered. Increasing the ratio of downstream static pressure to upstream stagnation pressure gives larger stand-off distances between the shock wave and the upstream tip of the shock wave holding plate. This change also decreases overall unsteadiness in the flow field, as quantified by lower overall grayscale spectral energy values, especially for Strouhal numbers less than about 0.0014. Increased downstream static pressure in the lower channel is accomplished by decreasing the venting area in the exhaust plenum, by lowering the shock wave holding plate (relative to the bottom surface of the test section), and by increasing the angle of the choking flap. The test section configuration associated with the test on 05 April 2018 has the cleanest shock wave pattern and the lowest grayscale spectral energy; thus, it is considered the best wind tunnel configuration of the ones tested.

Grayscale spectral energy variations with frequency show that unsteadiness is present at frequencies of 7 Hz, 40 Hz, and 110 Hz, which correspond to respective Strouhal number values of 0.00095, 0.0057, and 0.0144, for locations associated with the shock wave, lambda foot, upstream boundary layer, and downstream boundary layer. These values are roughly consistent with those detected by other researchers [14, 16, 25].

Auto-correlation function results show that the time sequence of grayscale values, for particular shock wave locations, is cyclical, with a period of approximately 1.4 seconds. Two-point correlation functions, as they vary with frequency, indicate that perturbations at a frequency of 100 Hz ( $St_r = 0.0131$ ) originate downstream of the shock wave and propagate upstream. At 40 Hz ( $St_r = 0.0057$ ), perturbations originate near the shock wave and propagate both upstream and downstream. Coherence functions, determined between different flow locations within the present investigation, show strong correlation between the shock wave and the downstream boundary layer exists at 20 Hz or  $St_r = 0.0029$ . Such results are consistent with spatial variations of coherence functions, and associated time lag magnitudes, which are determined at frequencies of 20 Hz, 40 Hz, and 100 Hz, with respective Strouhal number values of 0.0029, 0.0057 and 0.0144.

## REFERENCES

- [1] Ogawa, H., and Babinsky, H.: Wind-tunnel setup for investigations of normal shock wave/boundary-layer interaction control. *AIAA J.* 44, 2803-2805 (2006).
- [2] Edwards, J.A. and Squire, L.C.: An experimental study of the interaction of an unsteady shock with a turbulent boundary layer at Mach numbers of 1.3 and 1.5. *Aero J.* 97, 337-348 (1993)
- [3] Ott, P., Bolcs, A., and Fransson, T.H.: Experimental and numerical study of the time-dependent pressure response of a shock wave oscillating in a nozzle. *J. Turbomach.* 117, 106-114 (1995)
- [4] Bur, R., Benay, R., Galli, A., and Berthouze, P.: Experimental and numerical study of forced shock wave oscillations in a transonic channel. *Aerospace Sci Techn* 10: 265-278 (2006)
- [5] Bruce, P.J.K., and Babinsky, H.: Unsteady shock wave dynamics. *J. Fluid Mech.* 603, 463-473 (2008)
- [6] Threadgill, J., and Bruce, P. J. K.: Study of transonic shock wave/boundary layer interactions subject to unsteady forcing. *AIAA SciTech.* (13-17 January 2014), National Harbor, MD, USA
- [7] Doerffer, P., Szulc, O., and Magagnato, F.: Unsteady shock wave-turbulent boundary layer interaction in the laval nozzle”, *Task Quart.* 9, 115-132 (2005)
- [8] Clemens, N. T. and Narayanaswamy, V.: Low-frequency unsteadiness of shock wave turbulent boundary layer interactions. *Annu. Rev. Fluid Mech.* 46, 469-492 (2014)
- [9] Humble, R. A., Elsinga, G. E., Scarano, F., and vanOudheusden, B./ W.: Three-dimensional instantaneous structure of a shock wave/turbulent boundary layer interaction. *J. Fluid Mech.* 622, 33-62 (2009)
- [10] Ganapathisubramani, B/. Clemens, N. T.: Effects of upstream boundary layer on the unsteadiness of shock induced separation. *J. Fluid Mech.* 585, 369-394 (2007)



- [11] Ganapathisubramani, B., Clemens, N. T.: Low frequency dynamics of shock induced separation in a compression ramp interaction. *J. Fluid Mech.* 636, 397-436 (2009)
- [12] Touber, E., and Sandham, N. D.: Low-order stochastic modelling of low frequency motions in reflected shock-wave/boundary-layer interactions. *J. Fluid Mech.* 671, 417-465 (2011)
- [13] Piponnier, S., Dussauge, J. P., Debieve, J. F., and Dupont, P.: A simple model for low-frequency unsteadiness in shock-induced separation. *J. Fluid Mech.* 629, 87-108 (2009)
- [14] Grilli, M., Schmid, P.J., Hickel, S., Adams, N.A.: Analysis of unsteady behavior in shockwave turbulent boundary layer interaction. *J. Fluid Mech.* 700, 16-28 (2012)
- [15] Wu, M., Martín, M. P.: Analysis of shock motion in shockwave and turbulent boundary layer interaction using direct numerical simulation data. *J. Fluid Mech.* 594, 71-83 (2008)
- [16] Pirozzoli, S., Larsson, J., Nichols, J.W., Bernardini, M., Mogan, B.E., Lele, S.K.: Analysis of unsteady effects in shock/boundary layer interactions, *Annu. Res. Briefs.* 153-164 (2010)
- [17] Babinsky, H., and Harvey, J. K. (eds): *Shock wave - boundary-layer interactions.* Cambridge, UK (2011)
- [18] Sajben, M. and Kroutil, J.C.: Effects of initial boundary layer thickness on transonic diffuser flows. *AIAA J.* 19, 1386-1393 (1981)
- [19] Bogar, T.J., Sajben, M., and Kroutil, J.C.: Characteristic Frequencies of Transonic Diffuser Flow Oscillations. *AIAA J.* 21, 1232-1240 (1983)
- [20] Robinet, J.C. and Casalis, G.: Shock oscillations in diffuser modeled by a selective noise amplification. *AIAA J.* 37, 453-459 (1999)
- [21] Handa, T., Masudo, M., and Matsuo, K.: Mechanism of shock wave oscillation in transonic diffusers. *AIAA J.* 41, 64-70 (2003)
- [22] Dussauge J. P., Piponnier, S.: Shock/boundary-layer interactions: possible sources of unsteadiness. *J. Fluids Struct.* 24, 1166-1175 (2008)

- [23] Zheltovodov, A.A., Trofimov, V.M., Schülein, E., and Yakovlev, V.N.: A experimental documentation of supersonic turbulent flows in the vicinity of forward- and backward-facing ramps. Tech. Rep. 2030. Inst. Theor. Appl. Mech., USSR Acad. Sci., Novosibirsk. (1990)
- [24] Plotkin, K.J.: Shock wave oscillation driven by turbulent boundary layer fluctuations. AIAA J. 13, 1036-1040 (1975)
- [25] Gamba, M.: Roles of flows in a corner on the orderly response of a Mach 2 shock train. 10th Annual SWBLI TIM, (10-11 May 2016), Dayton, Ohio, USA
- [26] Settles, G. S.: Schlieren and shadowgraph techniques: visualizing phenomena in transparent media. Germany (2001)
- [27] Phantom v711. Vision Research. <http://www.phantomhighspeed.com/Products/v-Series-Cameras/v711> (2018). Accessed March 2018
- [28] Butterworth, S.: Theory of filter amplifiers. Experimental Wireless & the Wireless Engineer 7, 536-541 (1930)
- [29] John, J.E.A.: Gas Dynamics 2nd Ed. Newton, MA, USA (1984)

## **APPENDICES**

## APPENDIX A: PRESSURE REGULATOR CONTROLLER

### SETTINGS

Configuration	
Control Type	Standard
Line Frequency	60 Hz
Process Variable Source	Process Variable1
Output 2	Retransmission
Output 3	Off
Output 4	Off
Analog Range 1	4-20 mA
Analog Range 2	4-20 mA
Analog Range 3	4-20 mA
Analog Range 4	4-20 mA
Contact 1	Manual
Contact 2	Rem Set Point
Contact 3	Second Set Point
Contact 4	2nd PID
Contact 5	Alarm Acknowledge
Loop Name	Loop 1

Special	
AutoTrip	Off
Designated Output	-5%
Power Up	Manual
Power Up Out	-5%
Power Up Set Point	Last Set Point
Number of Set Points	1

Alarms	
Alarm Type 1	Off
Alarm Type 2	Off

Control	
Algorithm	PID
Derivative Source	Process Variable
Action 1	Reverse
Process Variable Break	0%
Low Out	45%
High Out	100%

Tuning	
Power Back	Disabled
Proportional Band	85%
Reset 1	5
Rate 1	1
Loadline 1	0%
Number of PID	1

Self Tune	
Type	Disabled
Noise Band	0%
Response Time	7200 sec
Dead Time	0.1 sec

Display	
Set Point	60
Deviation	-45.5
Out	-5%

Retransmission	
Type 2	Control Out

PV 1 Input	
Process Variable 1 Type	4-20 mA
Decimal	XXX.XX
Linearize	None
Low Range	0
High Range	150
Set Point Low Limit	0
Set Point High Limit	120
Set Point Ramp	Off
Filter	0 sec
Offset	0
Gain	1
Restore	Last Mode

Security	
Set Point Adjust	Locked
Auto/Manual	Unlocked
Set Point Select	Locked
Alarm Acknowledge	Locked
Tuning	Locked
Configure	Locked

Serial Communication	
Station	1
Baud Rate	9600 bps
CRC	yes
Shed Time	off

## APPENDIX B: DATA FILE DIRECTORY

### Preliminary Work (not included directly in thesis)

#### 01 Sept 2017

#### File Folder

PressureSpectra_09_01.docx	Pressure Spectra, linear axes
Pressure Data 01Sept17LogLog.docx	Pressure Spectra in Log axes
SchlierenSpectra_09_01_17.docx	Schlieren Spectra, some averaging
SchlierenSpectra_09_01_17_try2.pdf	Schlieren Spectra, more averaging
SchlierenSpectra_09_01_17_try3.pdf	Schlieren spectra, average 6x
Schlieren_FFT_MinusConst.pdf	Schlieren Spectra and code, averaging 1x, subtract arbitrary constant
Schlieren_FFT_1run.pdf subtract white noise	Schlieren Spectra and code, averaging 1x,
Schlieren_FFT_2run.pdf and subtracting white noise	Schlieren Spectra and code, averaging 2x,
2Ave_15Sept17.docx noise	Schlieren Spectra, average, subtract white
SchlierenSpectra_09_01_17_try4	Schlieren Spectra and code, averaged 5x,

#### 11 Sept 2017

#### File Folder

Pressure Spectra.docx	Pressure Spectra, Log axes
Pressure_Spectrum_11Sept17.m	Code to develop the Pressure Spectra Plots

15 Sept 2017

File Folder

imag4271\_withPoints.bmp

Pixel Locations Identified

Pressure Spectra.docx

Pressure Spectra, Log axes

Schlieren Spectra.docx

Schlieren Spectra Images only

Schlieren\_FFT\_18Sept2017.pdf

Schlieren Spectra and Code

**25 Sept 2017**

**File Folder**

imag4018\_marked.bmp

Pixel Locations Identified

Pressure\_Spectrum\_25Sept17.m

Code to get Pressure Spectra

Pressure\_Spectra.docx

Pressure Spectra for tests on 25 and 27 Sept

Venting Comparison\_1.pdf

Spectra, tests 25 and 27 Sept 2017 (25 had vent open, 27 had it closed)

**29 Sept 2017**

**File Folder**

fft.docx

Shadowgraph Spectra

imag1900\_points.bmp

Pixel Locations Identified

**05 Dec 2017**

**File Folder**

Schlieren\_FFT\_05Dec2017.m

MATLAB spectra Code

Spectra Summary.docx

Spectra, 2 point correlations, etc

Points Labeled.docx

The pixels used in Spectra Summary.docx

**05 Apr 2018**

**File Folder**

2018\_04\_05\_DSBL\_1.xlsx

Time data in recirculation region under SW

2018\_04\_05\_DSBL\_1\_filtered.xlsx

Filtered time data in recirculation region

SpectralData\_2018\_04\_05\_DSBL\_1.xlsx

Frequency data, recirc. region under SW

SpectralDataAve\_2018\_04\_05\_DSBL\_1.xlsx

Frequency data ensemble average  
recirculation region under the shock wave

2018\_04\_05\_DSBL\_2.xlsx

Time data, DSBL behind LF, near wall

2018\_04\_05\_DSBL\_2\_filtered.xlsx

Filtered time data behind LF near wall

SpectralData\_2018\_04\_05\_DSBL\_2.xlsx

Frequency data behind LF near Wall

SpectralDataAve\_2018\_04\_05\_DSBL\_2.xlsx

Frequency data ensemble average 5  
pixels behind LF near wall

2018\_04\_05\_DSBL\_3.xlsx

Time data under SW outside of recirculation  
region

2018\_04\_05\_DSBL\_3\_filtered.xlsx

Filtered time data under SW outside of  
recirculation region

SpectralData\_2018\_04\_05\_DSBL\_3.xlsx

Frequency data under SW outer BL

SpectralDataAve\_2018\_04\_05\_DSBL\_3.xlsx

Frequency data ensemble average of  
5 pixels under SW in outer BL

2018\_04\_05\_DSBL\_4.xlsx

Time data behind LF farther from wall

2018\_04\_05\_DSBL\_4\_filtered.xlsx

Filtered time data behind LF far from wall

SpectralData\_2018\_04\_05\_DSBL\_4.xlsx

Frequency data behind LF far from wall



SpectralDataAve_2018_04_05_DSBL_4.xlsx	Averaged frequency data, 5 pixels behind LF far from wall
2018_04_05_DSBL_5.xlsx	Time data far downstream
2018_04_05_DSBL_5_filtered.xlsx	Filtered time data far downstream
SpectralData_2018_04_05_DSBL_5.xlsx	Frequency data, far downstream
SpectralDataAve_2018_04_05_DSBL_5.xlsx	Average frequency data, 5 pixels far downstream
2018_04_05_USBL_1.xlsx	Time data far upstream near wall
2018_04_05_USBL_1_filtered.xlsx	Filtered time data far upstream near wall
SpectralData_2018_04_05_USBL_1.xlsx	Frequency data, upstream near wall
SpectralDataAve_2018_04_05_USBL_1.xlsx	Average frequency data, upstream near wall
2018_04_05_USBL_2.xlsx	Time data far upstream farther from wall
2018_04_05_USBL_2_filtered.xlsx	Filtered time data upstream, far from wall
SpectralData_2018_04_05_USBL_2.xlsx	Frequency data, upstream far from wall
SpectralDataAve_2018_04_05_USBL_2.xlsx	Average Frequency data, upstream far from wall
2018_04_05_USBL_3.xlsx	Time data closer to shock wave upstream
2018_04_05_USBL_3_filtered.xlsx	Filtered time data closer to SW upstream
SpectralData_2018_04_05_USBL_3.xlsx	Frequency data upstream close to SW
SpectralDataAve_2018_04_05_USBL_3.xlsx	Average frequency data, upstream close to shock wave
2018_04_05_USBL_4.xlsx	Time data USBL on the side walls

2018_04_05_USBL_4_filtered.xlsx	Filtered time data, USBL on the side walls
SpectralData_2018_04_05_USBL_4.xlsx	Frequency data, USBL on the side walls
SpectralDataAve_2018_04_05_USBL_4.xlsx	Average frequency data, side walls

### Chapter 3

High Perssure Piping SSWT.vsd	Editable schematic of the piping system
N1Research.pptx	Contour of the converging diverging Nozzle
Old vs New Slopes.xlsx	Curvature of the top wall, before and after spring 2017
InsertConnectsDiverterPlenum.pptx	Diagram, connection to the diverter plenum
INSERTS LIGRANI – 0918-2015.pdf	Hand drawing of inserts and wind tunnel connection to diverter plenum
See C:\Users\Research\Documents\Wind Tunnel Master\Wind Tunnel CAD on the pressure acquisition computer in the instrumentation room for the Wind Tunnel CAD Files such as models and drawings.	

### Chapter 4

SolarTurbinesLIGRANI 05-31-2017.pptx	Shadowgraph configuration, slides 15 and 16
--------------------------------------	---

### Chapter 5

2017_11_13_filtered_1.xlsx	Filtered time domain data of single pixel, column 2
SW_BeforeSmoothing.fig	Spectral plot from the shock wave before smoothing

SW_AfterSmoothing.fig	Spectral plot from the shock wave after smoothing
SW_NoiseCompare.fig	Spectral plot from the shock wave shows effect of white noise subtraction
SpectralData_2017_11_13_SW.xlsx	Spectral data of the 5 pixels on the shock wave
2017_11_13_SW5_Comparison_NoNoise.fig	Spectral plot from 5 pixels on the shock wave
SpectralDataAve_2017_11_13_SW.xlsx	Averaged spectral data of the 5 pixels
2017_11_13_Ave_SW5_NoNoise.fig	Spectral plot of average of 5 pixels on the shock wave
2018_04_05_trackshock_y277.xlsx	Pixel and displacement of the shock wave wrt time
TrackShockVTime_y277.fig	Plot of pixel location wrt time
TrackShockInchVTime_y277.fig	Plot of shock displacement in inches wrt time
LastFrame_trackShock_y277.fig	Plot of pixel intensity wrt x pixel coordinate
Running Average Table.xlsx	Chart depicting the smoothing process

## Chapter 6

Table_EnergyAndNoise.xlsx	Pixels, energy (plots), noise, data files, sampling rates
ShadowgraphComparisonImages.pptx	Editable conglomerate figures
TestSectionChangesChart.xlsx	Table of test section changes and area/pressure ratios

2017-11-15 at 17-29.xlsx	Pressure data from test on 15 Nov 2017, vent open
2017-11-08 at 15-48 (Recovered).xlsx	Pressure data from test on 08 Nov 2017, vent closed
2017-11-13 at 16-47.xlsx	Pressure data from test on 13 Nov 2017, vent half open
Shadowgraph Set-up 11 Dec 2017.pptx	Schematic diagram of angled shadowgraph set-up

**Data Files**

**File Folder, 5 pixel grayscale values**

2017_09_29_SW.xlsx	Time domain data
2017_09_29_SW_filtered.xlsx	Filtered time domain data
SpectralData_2017_09_29_SW5.xlsx	Frequency domain data
SpectralDataAve_2017_09_29_SW5.xlsx	Ensemble averaged frequency domain data
2017_09_29_LF5.xlsx	Time domain data
2017_09_29_LF5_filtered.xlsx	Filtered time domain data
SpectralData_2017_09_29_LF.xlsx	Frequency domain data
SpectralDataAve_2017_09_29_LF.xlsx	Ensemble averaged frequency domain data
2017_11_08_SW5.xlsx	Time domain data
2017_11_08_SW5_filtered.xlsx	Filtered time domain data
SpectralData_2017_11_08_SW.xlsx	Frequency domain data
SpectralDataAve_2017_11_08_SW.xlsx	Ensemble averaged frequency domain data
2017_11_08_LF5.xlsx	Time domain data
2017_11_08_LF5_filtered.xlsx	Filtered time domain data

SpectralData_2017_11_08_LF.xlsx	Frequency domain data
SpectralDataAve_2017_11_08_LF.xlsx	Ensemble averaged frequency domain data
2017_11_13_SW5.xlsx	Time domain data
2017_11_13_SW5_filtered.xlsx	Filtered time domain data
SpectralData_2017_11_13_SW_lowaq.xlsx	Frequency domain data, lower acquisition rate
SpectralDataAve_2017_11_13_SW_lowaq.xlsx	Ensemble averaged frequency domain data
2017_11_13_LF5.xlsx	Time domain data
2017_11_13_LF5_filtered.xlsx	Filtered time domain data
SpectralData_2017_11_13_LF_lowaq.xlsx	Frequency domain data, lower acquisition rate
SpectralDataAve_2017_11_13_LF_lowaq.xlsx	Ensemble averaged frequency domain data
2017_11_13_SW5.xlsx	Time domain data
2017_11_13_SW5_filtered.xlsx	Filtered time domain data
SpectralData_2017_11_13_SW.xlsx	Frequency domain data
SpectralDataAve_2017_11_13_SW.xlsx	Ensemble averaged frequency domain data
2017_11_13_LF5.xlsx	Time domain data
2017_11_13_LF5_filtered.xlsx	Filtered time domain data
SpectralData_2017_11_13_LF.xlsx	Frequency domain data
SpectralDataAve_2017_11_13_LF.xlsx	Ensemble averaged frequency domain data
2017_11_15_SW.xlsx	Time domain data

2017_11_15_SW_filtered.xlsx	Filtered time domain data
SpectralData_2017_11_15_SW.xlsx	Frequency domain data
SpectralDataAve_2017_11_15_SW.xlsx	Ensemble averaged frequency domain data
2017_11_15_LF.xlsx	Time domain data
2017_11_15_LF_filtered.xlsx	Filtered time domain data
SpectralData_2017_11_15_LF.xlsx	Frequency domain data
SpectralDataAve_2017_11_15_LF.xlsx	Ensemble averaged frequency domain data
2017_12_05_SW5.xlsx	Time domain data
2017_12_05_SW5_filtered.xlsx	Filtered time domain data
SpectralData_2017_12_05_SW_lowaq.xlsx	Frequency domain data, lower acquisition rate
SpectralDataAve_2017_12_05_SW_lowaq.xlsx	Ensemble averaged frequency domain data
2017_12_05_LF5.xlsx	Time domain data
2017_12_05_LF5_filtered.xlsx	Filtered time domain data
SpectralData_2017_12_05_LF_loqaq.xlsx	Frequency domain data, lower acquisition rate
SpectralDataAve_2017_12_05_LF_lowaq.xlsx	Ensemble averaged frequency domain data
2017_12_05_SW5.xlsx	Time domain data
2017_12_05_SW5_filtered.xlsx	Filtered time domain data
SpectralData_2017_12_05_SW.xlsx	Frequency domain data
SpectralDataAve_2017_12_05_SW.xlsx	Ensemble averaged frequency domain data

2017_12_05_LF5.xlsx	Time domain data
2017_12_05_LF5_filtered.xlsx	Filtered time domain data
SpectralData_2017_12_05_LF.xlsx	Frequency domain data
SpectralDataAve_2017_12_05_LF.xlsx	Ensemble averaged frequency domain data
2017_12_08_SW.xlsx	Time domain data
2017_12_08_SW_filtered.xlsx	Filtered time domain data
SpectralData_2017_12_08_SW_lowaq.xlsx	Frequency domain data
SpectralDataAve_2017_12_08_SW_lowaq.xlsx	Ensemble averaged frequency domain data
2017_12_08_LF.xlsx	Time domain data
2017_12_08_LF_filtered.xlsx	Filtered time domain data
SpectralData_2017_12_08_LF_lowaq.xlsx	Frequency domain data, lower acquisition rate
SpectralDataAve_2017_12_08_LF_lowaq.xlsx	Ensemble averaged frequency domain data
2017_12_08_SW.xlsx	Time domain data
2017_12_08_SW_filtered.xlsx	Filtered time domain data
SpectralData_2017_12_08_SW.xlsx	Frequency domain data
SpectralDataAve_2017_12_08_SW.xlsx	Ensemble averaged frequency domain data
2017_12_08_LF.xlsx	Time domain data
2017_12_08_LF_filtered.xlsx	Filtered time domain data
SpectralData_2017_12_08_LF.xlsx	Frequency domain data

SpectralDataAve_2017_12_08_LF.xlsx	Ensemble averaged frequency domain data
2017_12_13_SW.xlsx	Time domain data
2017_12_13_SW_filtered.xlsx	Filtered time domain data
SpectralData_2017_12_13_SW.xlsx	Frequency domain data
SpectralDataAve_2017_12_13_SW.xlsx	Ensemble averaged frequency domain data
2017_12_13_LF.xlsx	Time domain data
2017_12_13_LF_filtered.xlsx	Filtered time domain data
SpectralData_2017_12_13_LF.xlsx	Frequency domain data
SpectralDataAve_2017_12_13_LF.xlsx	Ensemble averaged frequency domain data
2018_03_22_SW.xlsx	Time domain data
2018_03_22_SW_filtered.xlsx	Filtered time domain data
SpectralData_2018_03_22_SW.xlsx	Frequency domain data
SpectralDataAve_2018_03_22_SW.xlsx	Ensemble averaged frequency domain data
2018_03_22_LF.xlsx	Time domain data
2018_03_22_LF_filtered.xlsx	Filtered time domain data
SpectralData_2018_03_22_LF.xlsx	Frequency domain data
SpectralDataAve_2018_03_22_LF.xlsx	Ensemble averaged frequency domain data
2018_04_04_SW.xlsx	Time domain data
2018_04_04_SW_filtered.xlsx	Filtered time domain data
SpectralData_2018_04_04_SW.xlsx	Frequency domain data



SpectralDataAve_2018_04_04_SW.xlsx	Ensemble averaged frequency domain data
2018_04_04_LF.xlsx	Time domain data
2018_04_04_LF_filtered.xlsx	Filtered time domain data
SpectralData_2018_04_04_LF.xlsx	Frequency domain data
SpectralDataAve_2018_04_04_LF.xlsx	Ensemble averaged frequency domain data
2018_04_05_SW.xlsx	Time domain data
2018_04_05_SW_filtered.xlsx	Filtered time domain data
SpectralData_2018_04_05_SW.xlsx	Frequency domain data
SpectralDataAve_2018_04_05_SW.xlsx	Ensemble averaged frequency domain data
2018_04_05_LF.xlsx	Time domain data
2018_04_05_LF_filtered.xlsx	Filtered time domain data
SpectralData_2018_04_05_LF.xlsx	Frequency domain data
SpectralDataAve_2018_04_05_LF.xlsx	Ensemble averaged frequency domain data
2018_04_05_USBL.xlsx	Time domain data
2018_04_05_USBL_filtered.xlsx	Filtered time domain data
SpectralData_2018_04_05_USBL.xlsx	Frequency domain data
SpectralDataAve_2018_04_05_USBL.xlsx	Ensemble averaged frequency domain data
2018_04_05_DSBL.xlsx	Time domain data
2018_04_05_DSBL_filtered.xlsx	Filtered time domain data
SpectralData_2018_04_05_DSBL.xlsx	Frequency domain data

SpectralDataAve_2018_04_05_DSBL.xlsx	Ensemble averaged frequency domain data
2018_04_05_SW.xlsx	Time domain data
2018_04_05_SW_filtered.xlsx	Filtered time domain data
SpectralData_2018_04_05_SW_short.xlsx	Frequency domain data
SpectralDataAve_2018_04_05_SW_short.xlsx	Ensemble averaged frequency domain data
<b>MATLAB Figures</b>	<b>File Folder, figures compare spectral data</b>
CF_LF.fig	Spectra on lambda Foot changing choking flap angle
CF_SW.fig	Spectra on shock wave changing choking flap angle
Overall_all.fig	Spectra on shock wave changing everything
Overall_all_LF_str.fig	Spectra of lambda foot changing everything
SHPHeight_SW.fig	Spectra on shock wave changing SHP Height
SHPHeight_LF.fig	Spectra on lambda foot changing SHP Height
SWHP_LF.fig	Spectra on lambda foot refinishing SWHP
SWHP_SW.fig	Spectra on shock wave refinishing SWHP
Venting_SW.fig	Spectra on shock wave changing venting amount
Venting_LF.fig	Spectra on lambda foot changing venting amount
<b>Journal Paper 1</b>	<b>File Folder</b>

V.83 ShockWaves Journal Paper.docx	Journal Paper, changes to Test Section
ChokingFlap_Energy.tif	Plot of total spectral energy wrt area ratio from cf angle
ChokingFlap_Shadowgraph.tif	Shadowgraph images changing cf angle
ChokingFlap_Spectra.tif	Grayscale Spectra comparing cf angle
OverallComparison_Shadowgraph.tif	Shadowgraph images from 13Dec17, Mar and Apr 2018
OverallComparion_Spectra.tif	Grayscale Spectra from 13 Dec 17, Mar and Apr 2018
PipingDiagram.tif	High and Low-Pressure Piping System Schematic, metric
PlenumVentingSchematic.tif	Drawing of Plenum and Vents
Pressure_2018_03_20_Metric.tif	Pressure Plot from 20 March 2018 in metric
ShadowgraphImage_2018_04_05.tif	Characteristic Shadowgraph image from 05 April 2018
ShadowgraphSchematic.tif	Drawing of Shadowgraph System Configuration, metric
SHP_HeightAreaTable.tif	Table relating area ratios to SWHP heights
SHPHeight_Energy.tif	Plot of spectral energy wrt area ratio from SHP height
SHPHeight_Shadowgraph.tif	Shadowgraph images changing SWHP Height
SHPHeight_Spectra.tif	Grayscale Spectra comparing SWHP Height
SmoothingTable.tif	Table showing general spectral smoothing scheme

Spectra_2018_04_05_FourRegions.tif	Spectra from 05 April 2018 in SW, LF, USBL, and DSBL
SWHP_Diagram_Refinished.tif	Dimensioned drawing of new SHWP (Nov 2017), metric
TestSection_PlenumToPlenum_Diagram.tif	Drawing of WT inside the laboratory building
TestSectionConfigurationTable.tif	Table showing testing configurations used
TestSectionPicture_BlackandWhite.png	Picture of the test section in black and white
TestSectionSchematic_metric.tif	Schematic Diagram of test section, metric, variable dims
VentingComparison_Energy.tif	Plot of spectral energy wrt pressure from venting
VentingComparison_Shadowgraph.tif	Shadowgraph images changing venting
VentingComparison_Spectra.tif	Grayscale Spectra comparing venting amount
VentingPressureTable.tif	Table relating 4 inch vent config with pressure ratio

\*The original collected data in the form of .cine files for each test are located on the shadowgraph capturing computer or associated back up hard drive in the instrumentation room; see [Users\Research\Documents\Windtunnel\Phantom V711 Videos](#) in either location for these raw data files.

### **Chapter 7 (13 Nov 2017)**

Frequency Comparison.xlsx	Peak frequencies in shadowgraph spectra
Frequency Spectra.docx	Shadowgraph Spectra associated with Points.docx

Points.docx	Pixel Locations Identified for Frequency Spectra.docx
FrequencySpectra_filtered.docx	Shadowgraph Spectra (with Points.docx), low pass filter applied
Spectra_top2.docx	Shadowgraph Spectra for second set of points
Spectra_top3.docx	Shadowgraph Spectra for third set of points
Compare3sets.docx	Multi-plot spectral charts comparing the 3 sets of pixels
AveragedTopSpectra(1to3).docx	Shadowgraph spectra for 1 through 3 averaged together in the frequency domain
Black Locations.docx	Shadowgraph spectra for four points outside flow area
AverageSpectraAnalysis.m	MATLAB code for averaging spectra together
SectralAnalysisOnly.m	Pixel Intensity Spectral Analysis MATLAB Code
PixelDataSaver.m	MATLAB code converts images to grayscale pixel intensity arrays
SpectralAnalysisOnly_SameRegion.m	Pixel Intensity Spectral Analysis MATLAB code for when the grayscale pixel intensity arrays are not in the same excel file
Filter1.vi	LabVIEW filtering Program
<b>Data</b>	<b>File Folder</b>
2017_11_13_top3_filtered.xlsx	time domain filtered pixel intensity data for set 3
2017_11_13.xlsx	time domain pixel intensity data for set 1

2017_11_13_filtered_1	time domain filtered pixel intensity data for set 1
2017_11_13_top2.xlsx	time domain pixel intensity data for set 2
2017_11_13_top2_filtered.xlsx	time domain filtered pixel intensity data for set 2
2017_11_13_top3.xlsx	time domain pixel intensity data for set 3
SpectralData_2017_11_13_SW_top_original.xlsx	Spectral Data for 3 pixels on the SW
SpectralData_2017_11_13_LF_top_original.xlsx	Spectral data for 3 pixels on the LF
SpectralData_2017_11_13_USBL_top_original.xlsx	Spectral data for 3 pixels in the USBL
SpectralData_2017_11_13_DSBL_top_original.xlsx	Spectral data for 3 pixels in the DSBL

### **Chapter 8 (-5 April 2018)**

2018_04_05_y480.xlsx	Time domain data for pixels along the line $y = 480$
2018_04_05_x674.xlsx	Time domain data for pixels along the line $x = 674$
Cohere_DSBL1.xlsx	Coherence, phase and time lag between DSBL region 1 and the lambda foot
Cohere_DSBL2.xlsx	Coherence, phase and time lag between DSBL region 2 and the lambda foot
Cohere_DSBL3.xlsx	Coherence, phase and time lag between DSBL region 3 and the lambda foot
Cohere_DSBL4.xlsx	Coherence, phase and time lag between DSBL region 4 and the lambda foot

Cohere_DSBL5.xlsx	Coherence, phase and time lag between DSBL region 5 and the lambda foot
Cohere_USBL1.xlsx	Coherence, phase and time lag between USBL region 1 and the lambda foot
Cohere_USBL2.xlsx	Coherence, phase and time lag between USBL region 2 and the lambda foot
Cohere_USBL3.xlsx	Coherence, phase and time lag between USBL region 3 and the lambda foot
Cohere_USBL4.xlsx	Coherence, phase and time lag between USBL region 4 and the lambda foot
Cohere_DSBL1_SW.xlsx	Coherence, phase and time lag between DSBL region 1 and the shock wave
Cohere_DSBL2_SW.xlsx	Coherence, phase and time lag between DSBL region 2 and the shock wave
Cohere_DSBL3_SW.xlsx	Coherence, phase and time lag between DSBL region 3 and the shock wave
Cohere_DSBL4_SW.xlsx	Coherence, phase and time lag between DSBL region 4 and the shock wave
Cohere_DSBL5_SW.xlsx	Coherence, phase and time lag between DSBL region 4 and the shock wave
Cohere_USBL1_SW.xlsx	Coherence, phase and time lag between USBL region 1 and the shock wave
Cohere_USBL2_SW.xlsx	Coherence, phase and time lag between USBL region 2 and the shock wave
Cohere_USBL3_SW.xlsx	Coherence, phase and time lag between USBL region 3 and the shock wave
Cohere_USBL4_SW.xlsx	Coherence, phase and time lag between USBL region 4 and the shock wave

2018_04_05_DSBL_1.xlsx	Time domain data for DSBL region 1 pixels
2018_04_05_DSBL_2.xlsx	Time domain data for DSBL region 2 pixels
2018_04_05_DSBL_3.xlsx	Time domain data for DSBL region 3 pixels
2018_04_05_DSBL_4.xlsx	Time domain data for DSBL region 4 pixels
2018_04_05_DSBL_5.xlsx	Time domain data for DSBL region 5 pixels
2018_04_05_USBL_1.xlsx	Time domain data for USBL region 1 pixels
2018_04_05_USBL_2.xlsx	Time domain data for USBL region 2 pixels
2018_04_05_USBL_3.xlsx	Time domain data for USBL region 3 pixels
2018_04_05_USBL_4.xlsx	Time domain data for USBL region 4 pixels
2018_04_05_DSBL_1_filtered.xlsx	Filtered time data for DSBL region 1 pixels
2018_04_05_DSBL_2_filtered.xlsx	Filtered time data for DSBL region 2 pixels
2018_04_05_DSBL_3filtered.xlsx	Filtered time data for DSBL region 3 pixels
2018_04_05_DSBL_4_filtered.xlsx	Filtered time data for DSBL region 4 pixels
2018_04_05_DSBL_5_filtered.xlsx	Filtered time data for DSBL region 5 pixels
2018_04_05_USBL_1_filtered.xlsx	Filtered time data for USBL region 1 pixels
2018_04_05_USBL_2_filtered.xlsx	Filtered time data for USBL region 2 pixels
2018_04_05_USBL_3_filtered.xlsx	Filtered time data for USBL region 3 pixels
2018_04_05_USBL_4_filtered.xlsx	Filtered time data for USBL region 4 pixels
imag00017_manypoints.bpm	Image showing all the regions
imag0017_lines.bpm	Image showing the lines of coherence



## APPENDIX C: LIST OF PROGRAMS

MATLAB 2013a - 2018a

AverageSpectraAnalysis.m	Averages spectra together
SectralAnalysisOnly.m	Pixel Intensity Spectral Analysis PixelDataSaver.m converts images to grayscale value arrays (R2014, R2018)
SpectralAnalysisOnly_SameRegion.m	Pixel Intensity Spectral Analysis MATLAB code for when the grayscale value arrays are not in the same Excel file
SpectralAnalysisOnly_2.m	Grayscale spectral analysis with ensemble averaging
SpectraComparison.m	Plots spectra from various spectral data excel files
TrackShock.m	Determines streamwise shock wave location (R2013a only)
SpectralAnalysisShockMotion.m	Spectral analysis for shock position data
ScaleShockPath.m	Converts from pixels and image number to inches and time for shock position
Correlations_manypoints_spatial.m	Coherence and time lag of a line of data compared to a single pixel
Correlations.m	Coherence and time lag between 5 points each from 2 regions
Autocorrelation.m	Single point auto-correlation of 5 pixels separately
PixelDataSaver_manypoints.m	Saves time domain data from points along a specified line in an image

get_newest_mach_numbers.m	In pressure acquisition code
graphdava_v6.m	In pressure acquisition code
upfromdownmach.m	In pressure acquisition code
isentropicmach.m	In pressure acquisition code
rayleigh.m	In pressure acquisition code

#### LabVIEW

Filter1.vi	Low pass filter grayscale pixel data (LV 2011)
Probe Pressure (with data export) (150 psi pitot-static system)	Acquire pressure data at 50 Hz, early tests (LV 2015)
Probe Pressure (with data export) (150 psi pitot-static system)03-Apr-18	Acquire pressure data at a faster rate, only some channels measured (2015)

Phantom Camera Control Applications	Acquire and save shadowgraph data
-------------------------------------	-----------------------------------

Microsoft Excel	Processed data saved in this format
-----------------	-------------------------------------

Microsoft Powerpoint	Create, modify, and annotate figures
----------------------	--------------------------------------

Microsoft Paint	Take measurements from pixels
-----------------	-------------------------------

Solid Edge	Facility models and drawings
------------	------------------------------

Microsoft Visio	Schematic diagram of piping system
-----------------	------------------------------------

#### Batch Scripts

Test1 Video Maker.bat	Converts bitmap image files to mp4 video
-----------------------	--

generate_excel.bat	Generates the excel file from pressure acquisition code
--------------------	---

Snipping Tool

Microsoft Word

LibreOffice

Google Chrome